THESIS

CALIBRATION AND UNCERTAINTY OF A HEAD-DISCHARGE RELATIONSHIP FOR OVERSHOT GATES UNDER FIELD CONDITIONS

Submitted by

Caner Kutlu

Department of Civil and Environmental Engineering

In partial fulfillment of the requirements

For the Degree of Master of Science

Colorado State University

Fort Collins, Colorado

Spring 2019

Master's Committee:

Advisor: Timothy K. Gates

Subhas Karan Venayagamoorthy
Gregory Butters

Copyright by Caner Kutlu 2019

All Rights Reserved

ABSTRACT

CALIBRATION AND UNCERTAINTY OF A HEAD-DISCHARGE RELATIONSHIP FOR OVERSHOT GATES UNDER FIELD CONDITIONS

Adjustable overshot gates (pivot weirs) are commonly used to control discharge and water levels in irrigation water delivery networks. The degree to which this control can be achieved depends upon reliable relationships between flow rate and the hydraulic head upstream and downstream of the gate. Moreover, such relationships also can be used for flow measurements. This study aims to develop a head-discharge equation for free flow over a overshot gate, to describe its uncertainty, and to examine the impact of gate submergence on the equation.

Previous research on the flow characteristics of overshot gates has been performed primarily in laboratories, with very little investigation of performance in the field. This thesis provides a report of a field study conducted on four Obermeyer-type pneumatically automated overshot gates, which were operated for irrigation water delivery in northern Colorado. Utilizing both classical and amended forms of the sharp-crested weir equation, Buckingham-Pi dimensional analysis, and incomplete self-similarity theory, head-discharge equations for free flow have been developed which are alternately dependent on and independent of the gate inclination angle. To estimate the flow rate, three fully-suppressed Obermeyer-type overshot gates with crest widths of 22 ft, 20 ft, and 15 ft, and respective lengths of 5 ft., 6.3 ft., 6.08 ft , were inspected for eight different inclination angles (α = 22.8°, 23.6°, 29.7°, 32.6°, 34.6°, 35.3°, 38.9°, 40.4°), under free flow conditions. The best-performing equation is of classical form and

contains a discharge coefficient dependent on gate inclination angle. It can be used to relate the discharge to upstream hydraulic head with about ± 10 % (standard deviation range of residual error) for free flow conditions. This equation is applicable for inclination angles between 20° and 40° and for flow rates ranging from 20 to 330 ft^3/s. To reduce uncertainty of the discharge coefficient and to prevent the misleading consequences of neglecting the velocity head in the approaching flow, the total upstream energy head was employed in the equation. The effect of velocity head was significant for flow estimation. Dependency of the equation on the gate and field characteristics was examined by testing the equation with field data for a different type of overshot gate. Alternate equations were developed which altered the classical form for a sharp-crested weir to include both a coefficient and an exponent that are dependent upon gate inclination angle, and which preserved the classical form and treated the discharge coefficient as a constant independent of gate inclination. Although, satisfactory results were obtained for these alternative forms, inclusion of the angle in the discharge coefficient alone was recommended for higher accuracy of flow rate estimation, particularly for larger overshot gates with inclination angles ranging from about 20° to about 40°. Furthermore, the modular limit of the overshot gates was investigated for a fourth Obermeyer gate with a crest width of 17 ft and a length of 5.8 ft. Up to a submergence ratio of 0.51, the submergence effect was not observed to decrease the flow rate over for the gate. More data for a higher submergence conditions are required to develop a modular limit and a head-discharge equation for submerged flow.

ACKNOWLEDGEMENTS

Firstly, I would like to thank my study advisor Professor Timothy K. Gates of the Civil and Environmental Engineering at Colorado State University. I am grateful to him for always being patient and encouraging. Throughout my studies, he steered me in the right direction whenever I encountered difficulties that were hard to overcome. I also wish to express my sincere gratitude to my thesis committee members Dr. Subhas Karan Venayagamoorthy and Dr. Gregory Butters for their cooperation.

Beside my advisor, my sincere thanks goes to my parents Nalan and Yavuz Kutlu, my brother Cagri Kutlu, my girlfriend Emily Dean, and our family friends Zehra - Osman Aydin and Ayse - Harun Ocak for their continuous encouragement throughout my research process. This accomplishment would not have been possible without their spiritual support.

Last but not the least, I am indebted to the Republic of Turkey - General Directorate of State Hydraulic Works for supporting my studies financially.

TABLE OF CONTENTS

LIST OF TABLES

LIST OF FIGURES

CHAPTER 1

INTRODUCTION

Irrigation practices are the most water-consumptive activities around the world. Considering decreasing useable water resources and population growth, effective use of water in agricultural applications becomes essential in order to meet increasing water demands. Wiser water resources management in irrigation systems leads to higher crop yields, enhanced water quality, and water conservation.

Ali (2010) stated that measuring flow rate is a vital part of irrigation water management. Moreover, Molden and Gates (1990) noted that regulation and measurement of water are significant elements of an irrigation delivery network's performance. Accurate measurement of the flow rate in irrigation delivery systems contributes to increased efficiency, reducing excessive diversion and application of water, contributing to short and long term water management plans, and contributing to legal, equitable, and dependable distribution of water. Flow measurement structures in open channels create a distinctive relationship between head and discharge (Boiten 2002). Akan (2011) broadly classified these structures as weirs and flumes. Flumes are specific measurement structures that take advantage of critical flow conditions in order to calculate discharge. Bos (1976) classified flumes as long-throated flumes, throatless flumes, Parshall flumes, or H flumes. Weirs are another type of common channel flow control structure, also used for flow measurement, and often classified in accordance with the thickness of the weir crest – sharp-crested weirs, short-crested weirs, and broad-crested weirs. Another classification of the weirs was suggested by French (1985) with respect to the shape of the crest – V-notch, rectangular, trapezoidal, and parabolic weirs. Besides weirs and flumes, sluice gates also are

used for hydraulic control. Typically, sluice gates function as underflow structures. However, they behave as weirs when the gates are lowered enough that the flow spills over the top of the gates.

Sharp-crested weirs are widely used control structures in open channels. They are one of the oldest control structures in engineering history and have inspired numerous additional types of hydraulic structures. Martínez et al. (2005) indicated that sharp-crested weirs are simple structures with low maintenance requirements, and provide remarkably accurate results for flow measurement applications. Overshot gates (pivot weirs) are an example of such structures. The adjustable crest elevation of these structures provides flexibility for water level control. Like other weir-type structures, they not only provide water level control, but also allow for flow measurement if properly calibrated.

An Obermeyer-type pneumatically automated gate is an overshot gate whose crest elevation is pneumatically automated (Figure 1 and Figure 2). Hinged across the bottom, and resting on a concrete foundation, it consists of a steel gate leaf and inflatable air bladder. The leaf has a curved structure that is considerably thin (1/4 inch). The adjustment of the gate leaf is provided by the air bladder, which is inflated and deflated by small air compressors to conduct hydraulic control activities. Power for the air compressors is supplied by small 12V batteries. Operation mechanisms of the gates typically are housed in a control building located nearby. Moreover, each structure has rubber blockers in order to prevent over-inflation of the gate leaves.

(a) (b)

(c) (d)

Figure 1. Obermeyer-type overshot gates showing a) gate leaf equipped with nappe-breakers, b) a free flow over the gate viewed from downstream, c) inflate air bladders of the gate leaf, and d) a view of free flow viewed from upstream.

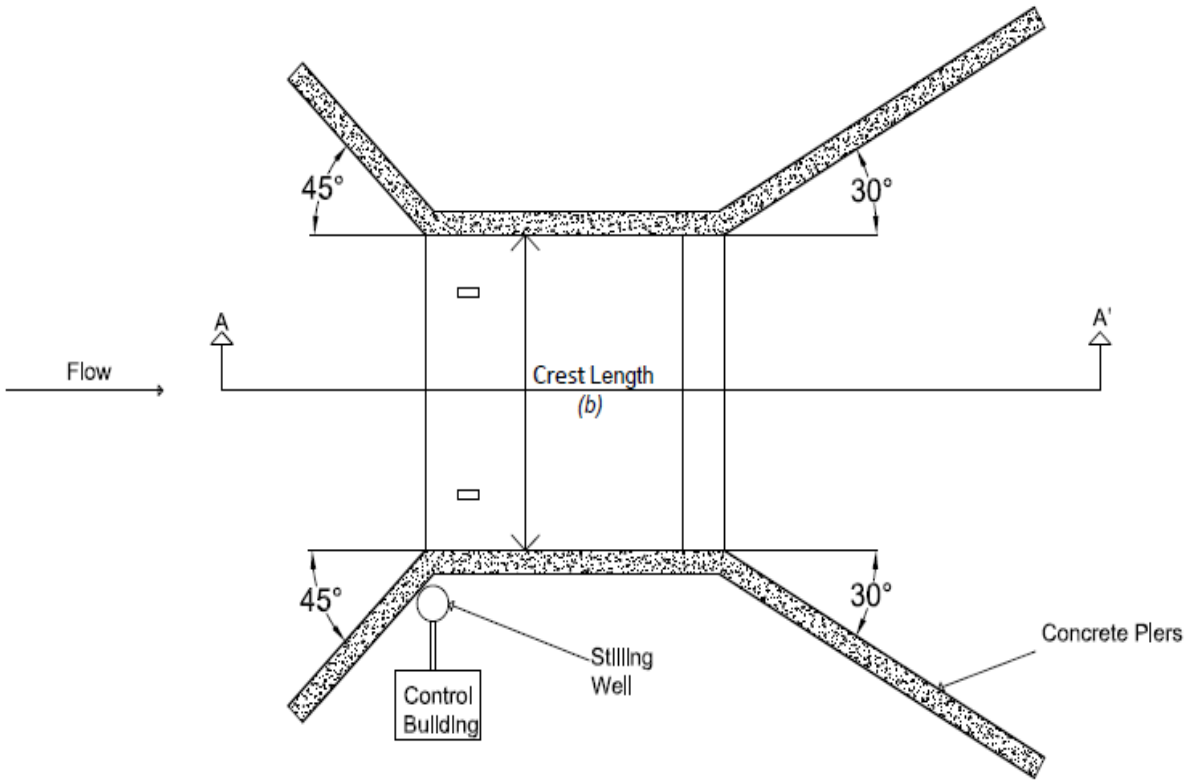

Plan View

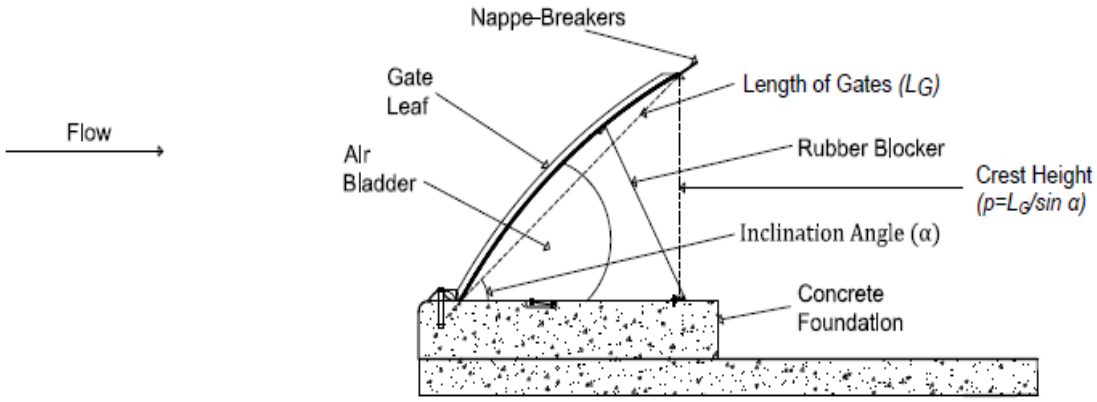

AA' Section

Figure 2. A general sketch of an Obermeyer overshot gate, showing a plan view and a longitudinal cross sectional view.

Wahlin and Replogle (1994) indicated that overshot gates behave similarly to sharp-crested weirs at high inclination angles, but coincide with free over flow at low inclination angles. Thus, Obermeyer-type adjustable overshot gates can be classified as inclined rectangular sharp-crested weirs.

The literature review (Chapter 2), summarizes previous research conducted on flow behavior of sharp-crested weirs and overshot gates. Outflow studies on these structures, described the hydraulic behavior. Numerous experimental studies have been conducted under laboratory conditions. However, there has been very little research reported in the literature on head-discharge relationships under actual field conditions. Field and laboratory conditions differ in many aspects with respect to open channel flow over a weir. Field conditions involve more variability in properties, such as roughness, geometry, velocity distribution of the flow, turbulence, etc. Accordingly, field tests reflect flow behavior under characteristics and constraints encountered in practice. In this study, an applicable relationship was expressed between hydraulic head and discharge for the flow process over suppressed (no horizontal contraction at the crest) Obermeyer-type adjustable overshot gates under operating conditions in a canal in Northern Colorado. The total energy head effect on the discharge was scrutinized, the gate inclination effect on the discharge was inspected, and the modular limit of the overshot gates was examined to comprehend the hydraulic behavior of the overshot gates for actual field conditions.

CHAPTER 2

LITERATURE REVIEW

Many studies have been conducted on sharp-crested weirs. Tracy (1957) presented the discharge equation of sharp-crested weirs accounting for hydraulic energy head over the crest for free flow, as below (Figure 3):

$$Q = \frac{2}{3} C_d \sqrt{2g}\, b\, H^{1.5} \tag{1}$$

where Q is the discharge [L^3/T], C_d is the discharge coefficient, g is the acceleration of gravity [L/T^2], b is the crest length across the channel [L], and H is the total energy head relative to the weir crest [L] (measured at a distance of 4h to 5h upstream of the weir crest), with

$$H = h + \Lambda \frac{\bar{u}^2}{2g} \tag{2}$$

and

$$\bar{u} = \frac{Q}{A} = \frac{Q}{f(y)} \tag{3}$$

Now, $\bar{u}$ is the cross-section averaged channel approaching flow velocity [L/T], y is the total channel flow depth upstream [L], and h is the upstream flow depth above the crest of the weir [L]. Λ is the kinetic energy correction factor (Subramanya, 1982) and A is the upstream cross-sectional area [L^2]. A is a function of y that depends upon the channel cross section geometry.

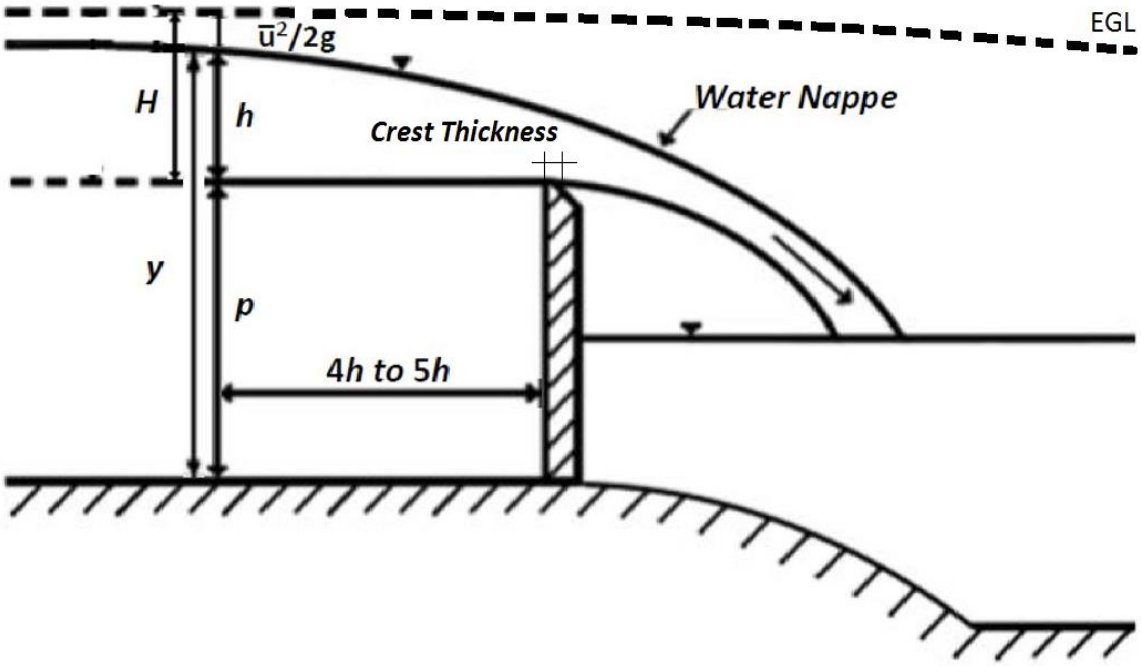

Figure 3. Sharp crested weirs parameters. Adapted from Bilhan et al. (2016).

In Rehbock's (1929) experimental study, the discharge coefficient was calculated as a function of the ratio of approaching flow depth between the crest of the weir and the water surface level to the crest height. Villemonte (1947) experimentally studied submerged weirs and discovered a drowned flow reduction factor to define the submerged flow on sharp-crested weirs. Kindsvater and Carter (1959) derived a version of the flow rate equation accounting for fluid viscosity and surface tension forces for both free and submerged flow over sharp-crested weirs. In the study an effective discharge coefficient was defined. The effective discharge coefficient accounted viscous and surface tension forces as a function of *h*. Hulsing (1968) depicted the discharge coefficient variation with *h*/*p* for both submerged and free flow conditions. Bos (1976), derived the discharge equations for different types of sharp crested weirs, with rectangular, parabolic, triangular and circular control sections by assuming horizontal and

parallel distribution of velocity profiles over the weir crests. Ramamurthy et al. (1987) pursued experimental laboratory studies and obtained a relationship between the discharge coefficient and the ratio h/p, where p is the height of the crest, using the conservation of momentum principle. Swamee (1988) determined a generalized weir equation for not only sharp-crested weirs, but also for broad ($0.1 \leq h$ divided by crest thickness ≤ 0.4), narrow ($0.4 < h$ divided by crest thickness ≤ 1.5), and long-crested weirs (h divided by crest thickness < 0.1). Wu and Rajaratnam (1996) developed a diagram to estimate the regime types that were possible under submerged flow conditions. Borghei at al. (1999) conducted experimental studies under laboratory conditions on sharp crested weirs under subcritical conditions and presented a new discharge coefficient using conservation of energy principle. Although, the majority of researchers (i.e. Bos, 1976; Swamee, 1988; Ramamurthy, 1987) neglected the velocity head of the approaching flow or only considered the velocity head effect within the discharge coefficient, Johnson (2000) utilized the specific energy concept in the classical discharge equation of sharp crested weirs for free flow. Borghei et al. (2003) conducted experimental laboratory studies on the oblique rectangular sharp-crested weirs and extracted the discharge coefficient formulas for both free and submerged flow conditions. Azimi and Rajaratnam (2009) performed critical flow analyses on different crest-type weirs and proposed new discharge coefficient equations. Afzalimehr and Bagheri (2009) showed that potential flow theory, which uses an idealized fluid model for incompressible, irrotational and non-viscous fluids, was a practical approach for estimating discharge coefficients for sharp-crested weirs. Vatankhah (2010) conducted studies on circular shaped-sharp crested weirs and proposed a new discharge coefficient. Aydin et al. (2011) executed experimental laboratory studies on sharp-crested weirs and recommended employing

the average flow velocity at the weir section rather than using an empirically-derived discharge coefficient in the flow equation. Rady (2011) used 2D and 3D computer models to analyze the flow over sharp-crested weirs and determined that the upstream velocity head should be considered in the the flow equation. Arvanaghi and Oskuei (2013) performed laboratory experiments and numerical studies on sharp-crested weirs and proposed a fixed discharge coefficient for a Reynolds number greater than 20,000 and a Froude number greater than 0.2.

Azimfar et al. (2018) applied conservation of energy and momentum principles to flow over overshot gates and proposed a discharge coefficient equation by assuming negligible energy head loss from upstream of the weir to its crest. Wahlin and Replogle (1994) experimentally studied overshot gates under laboratory and field conditions for both free and submerged flow conditions. The researchers limited the considered inclination angles between 16.2° and 63.4° for overshot gates manufactured by the Armtec Company. Two Armtec gates located in Imperial Irrigation District (IID)'s trapezoidal concrete lined canals were used in the field tests. The lengths of the gates were 5.08 ft and 5.58 ft, while the crest widths for both gates were 2 ft. The gate leaves were flat and made of stainless steel. The crest of the gate was rounded to some extent and severe side seal effects (supplement material mounted at side of the gates which effected flow area) for the flow over the gates were observed during the field tests. Wahlin and Replogle (1994) obtained the following equation using the approach of Kindsvater and Carter (1959) to analyze the flow over overshot gates:

$$Q=(\frac{2}{3})C_aC_e\sqrt{2g}b_eh_e^{1.5} \quad (4)$$

where C_a is a correction factor that depends upon α, C_e is the effective discharge coefficient, b_e is the effective crest length [L] which is a function of lateral contraction over the crest, and h_e is

the effective flow depth above the crest of the weir [L]which is a function of empirical coefficients under the effect of viscous forces. C_a was presented as a polynomial function of α.

Prakash et al. (2011) conducted research on an inclined rectangular weir with a crest length of 0.5 ft and width of 0.5 ft via laboratory experiments in a plexiglass channel by neglecting the approaching flow velocity head. The authors derived a polynomial angle correction coefficient equation as a function of α. The angle correction coefficient ranged over 1 - 2.25 for the various inclination values of α considered (α = 0°, 15°, 30°, 45°, 60°) and the discharge ratio from 0.07 ft^3/s to 0.74 ft^3/s. The value of α highly affected the flow rate and the angle correction coefficient increased when α increased.

Nikou et al. (2016) studied overshot weirs (three weirs with 2.62x2.13 ft, 1.97x1.8 ft, 1.31x1.31 ft) experimentally under free and submerged flow. The researchers completed laboratory experiments for α values of 0°, 20°, 40°, 60°, 80°, and 90°. The researchers utilized two different approaches to obtain head-discharge equations. The first approach used the form of the Wahlin and Replogle (1994) equation and in the second form new discharge coefficient equations were derived utilizing the conservation of energy principle and assuming critical depth conditions at the crest of the weir. The researchers concluded that the derived equations were more applicable than that of Wahlin and Replogle (1994). The researchers also indicated that decreasing α increased the discharge capacity substantially, a finding contrary to Prakash (2011). Shayan et al. (2018) published a discussion on Nikou et al.'s (2016) research and indicated that hydrostatic pressure distribution and uniform velocity distribution assumptions were not valid for the scenario. Instead, another coefficient was recommended for the correction of non-hydrostatic pressure. Later, Nikou et al. (2018) published a closure and explained that the error

associated with these phenomena had been embedded in the empirical derivation of the discharge coefficient itself.

Fenton (2015) believed that utilizing dimensional analysis was wiser than maintaining traditional physical approaches in understanding the theory of flow over sharp-crested weirs. Ferro (2011) examined broad- and sharp-crested weir flow processes by utilizing dimensional analysis and incomplete self-similarity theory. The classical sharp-crested weir discharge equation (Eq. 1) was rearranged and a similar power equation was obtained:

$$\frac{h}{p} = m \left(\frac{k_s}{p}\right)^n \tag{5}$$

where k_s is an assigned coefficient (a function of discharge, crest width, and acceleration of gravity), and m and n are a coefficient and exponent that could be found experimentally. The researcher noted that *n* could be equated to 1 for fully-suppressed sharp-crested and broad-crested weirs, whereas the m relied on the geometry of the weirs.

Di Stefano and Ferro (2013) utilized dimensional analysis and self-similarity theory to determine the stage discharge relationship on triangular in-plane sharp crested weirs. A power equation (Eq. 5) was a conventional form to depict the discharge head relationships for this type of weirs.Bijankhan et al. (2013) conducted an experimental laboratory study on sharp-, short-broad- and long-crested weirs [as defined in Rao and Muralidhar (1963), long-crested weir ($0 < h/L_c \leq 0.1$), broad-crested weir ($0.1 < h/L_c \leq 0.4$), short-crested weir ($0.4 < h/L_c \leq 2$), and sharp-crested weir ($h/L_c > 2$), where L_c is crest thickness]. The researchers obtained Eq. 5 using dimensional analysis and incomplete self-similarity theory, concluding that different parameters of the weir, such as the ratio of the crest length to the crest thickness, followed a single trend

under different values. Thus, the power equation exponent *n* was always taken to be 1 for sharp-, short-, broad-, and long-crested weirs.

Di Stefano et al. (2016) also pursued studies on weirs with irregular shapes utilizing dimensional analysis and incomplete self-similarity theory. Triangular weirs with upstream and downstream ramps (resembling overshot gates in terms of geometry) and broad-crested weirs with positive and negative crest slopes were investigated using available data from the literature. The researchers obtained Eq. 5 with *n* = 1, referencing Bijankhan et al. (2013) and noting that the power equation the coefficient *m* depended on the geometry of the weirs. The researchers proposed a discharge coefficient and concluded that utilizing dimensional analysis and incomplete self-similarity theory provided satisfactory results, even for irregularly-shaped weirs.

Bijankhan and Ferro (2017) also utilized dimensional analysis and incomplete self-similarity to examine flow over overshot gates. The researchers indicated that the α and the contraction ratio of the gate (the ratio of crest length to the canal width) were essential parameters for describing the flow process. The researchers obtained a power equation (Eq. 5) to express the head-discharge relationship by utilizing the experimental data of Nikou et al. (2016). Both the *m* and the *n* were found to be functions of α. The researchers proposed second-order polynomial equations to represent these functions.

Di Stefano et al. (2018) examined the contraction ratio and the effect of α on flow rate using dimensional analysis and incomplete self-similarity theory. The researchers used the data presented in Wahlin and Replogle (1994). The power equation (Eq. 5) was employed considering *n*=1 and *m*, which could be utilized to acquire C_d was obtained. The authors showed that the effect of α was negligible when there was no side contraction on the gate crest. Thus, a

representation of the head-discharge equation was proposed independent of α with n=1 for overshot gates. The researchers, also, recommended more studies on inclined weirs to better express the effect of α because of the contradiction of the results to those of Prakash (2011).

Bijankhan et al. (2018) pursued experimental and numerical studies on inclined rectangular weirs using dimensional analysis and incomplete self-similarity theory (for α = 30°, 40°, 54°, and 90°). The experimental study was pursued on an inclined rectangular weir with a crest length of 1.64 ft in a laboratory. The experimental study was supplemented with a numerical analysis using a computational fluid dynamics model. The researchers obtained Eq. 5 and indicated that *n* could be equated to 1, whereas *m* was a function of α. They showed that decreasing α increased *Q* over the inclined rectangular weir for $\alpha =$ 30° and α = 40° but for $\alpha =$ 54° and α = 90°, the effect of α on *Q* was trivial.

This present study utilizes Eq. 5 in the development of three different equations to express the relationship between head and discharge for overshot gates. The first head-discharge equation was obtained considering both m and n as functions of α, as described in Bijankhan and Ferro (2017). A second head-discharge equation was obtained as prescribed in (Bijankhan et al. (2018) by using the classical form of the sharp-crested weir equation (Eq. 1) wherein *n=1* and *m* was applied to obtain C_d, which is a function of α as prescribed by Nikou et al. (2016) and Prakash (2011). Lastly, following Di Stefano et al. (2018), the classical form of the equation was used with C_d that obtained by *m* derived as a constant independent of α and with *n* = 1. The development and performance of these three forms of the head-discharge equation are described and compared.

CHAPTER 3

METHODOLOGY

3.1 Site Description and Field Measurements

Four Obermeyer-type pneumatically automated overshot gates were selected for examination during the irrigation season. The gates were located in an irrigation canal operated by a local irrigation company in Northern Colorado. The main considerations in gate selection were accessibility, condition and functionality, and convenience of conducting discharge measurements on the upstream side of the structures. Field tests of these gates were conducted for the irrigation seasons of 2017 and 2018. Table 1 displays a summary of the data collection.

Table 1. Data collection summary table.

Montgomery Check Structure	
2017 irrigation Season (July 18 – September 18)	
Number of Measurements	28
Q (ft^3/s)	
Average	209.5
Standard Deviation	107.8
Max	330
Min	20.4
H (ft)	
Average	2.11
Standard Deviation	0.79
Max	2.92
Min	0.64
α	23.6°, 29.7°, 34.6°
2018 Irrigation Season (August 2 – September 7)	
Number of Measurements	19
Q (ft^3/s)	
Average	213
Standard Deviation	56
Max	281.4
Min	85.4

Table 1 (continued)

H (ft)	
Average	2.19
Standard Deviation	0.36
Max	2.54
Min	1.43
α	29.7°, 32.6°, 34.6°
Magnuson Check Structure	
2017 irrigation Season (July 18 – September 18)	
Number of Measurements	19
Q (ft^3/s)	
Average	220
Standard Deviation	97.6
Max	307.13
Min	23.32
H (ft)	
Average	2.38
Standard Deviation	0.74
Max	2.97
Min	0.71
α	35.3°, 38.9°
2018 Irrigation Season (August 2 – September 7)	
Number of Measurements	18
Q (ft^3/s)	
Average	202.7
Standard Deviation	53.2
Max	258.9
Min	77.6
H (ft)	
Average	2.33
Standard Deviation	0.33
Max	2.66
Min	1.47
α	38.9°, 40.4°
W85 Check Structure	
2017 irrigation Season (July 18 – September 18)	
Number of Measurements	21
Q (ft^3/s)	
Average	229.2
Standard Deviation	29.7
Max	266.2
Min	173.5

Table 1 (continued)

H (ft)	
Average	2.6
Standard Deviation	0.26
Max	2.98
Min	2.12
Gate Angles (Degrees)	23.4°, 26.9°, 31.8°
HWY 14 Check Structure	
2017 irrigation Season (July 18 – September 18)	
Number of Measurements	12
Q (ft^3/s)	
Average	164.5
Standard Deviation	12.9
Max	182.6
Min	137.6
H (ft)	
Average	2.32
Standard Deviation	0.12
Max	2.46
Min	2.04
Gate Angles (Degrees)	22.8°

3.1.1 Physical Features of the Gates

The studied gates have been labeled A (Montgomery Check Structure), B (Magnuson Check Structure), C (W85 Check Structure), and D (HWY 14 Check Structure) for ease of notation. The general configuration of each of the gates can be seen in Figure 4. Design drawings of Gates A and B were provided by the canal company (Appendix 1). Since Gates C and D was mounted much earlier than A and B, their project could not be provided. Comparison of design drawings to conditions in the field revealed no difference that would significantly affect flow conditions. The surfaces of the gate leaves were completely covered by an extensive rust layer (Figure 5), but the cross-sectional area loss due to the rusty zones was trivial. The gate leaves had stiffness plates that were mounted parallel to the flow direction (Figure 5). These plates not only increased

the stiffness of the leaves, but also directed the streamlines to be perpendicular to the crest. Each gate was hinged across the bottom and sat on top of a concrete foundation. The movement of the gate leaves was controlled by air bladders made of rubber that were inflated and deflated by air compressors. Next to each of the gates, control buildings housed control stations and electrical power units. Solar power systems mounted on top of the control buildings were the main sources of energy in the field. 12V batteries were also required for the power units.

Each gate had a stilling well on the upstream side to facilitate flow depth measurements using a water level logger (pressure transducer). The lateral distance between the stilling wells and the crest of the gates for the four Obermeyer gates were measured as approximately 4 ft to 7 ft, depending on the setting of α. Stilling wells supply a clear measurement zone that reduces the turbulence on the water's surface and blocks any external substances delivered by the flow. Bos (1976) indicated that the upstream flow depth measurements should be taken at a distance from the crest of 4*h* to 5*h*. The researcher suggested this distance in order to avoid surface drawdown effects due convective acceleration between the structures and the measurement stations. Therefore, suitability of the stilling wells for upstream water level measurements were inspected in relation to of the zone of drawdown (Chapter 3, Part 1.2.2).

According to the U.S. Bureau of Reclamation (USBR Water Measurement Manual, 2001), the water nappe that passes over the crest of the weir, should be aerated properly to insure atmospheric pressure below the nappe. In the case of clinging or depressed flow conditions, negative pressure occurs under the nappe and can create a deviation in the discharge measurement applications by causing excessive drawdown. To prevent misleading measurement implications, proper aeration of the water nappe should be provided for the gates. Bos (1976)

stated that improper aeration of the weir causes an increase of the nappe curvature and leads to an increased discharge coefficient in the head-discharge relationship. In the field settings of this study, air ventilation was supplied using two different ways for the structures. For relatively low flow regimes ($Q \leq 50$ ft^3/s), nappe-breakers mounted on top of the gate leaves effectively provide air ventilation under the nappe (Figure 6). For relatively high flow regimes ($Q > 50$ft^3/s), streamline curvature at the crest allows for proper aeration of the gate. The inclined form of the gate leaves and the expanding retaining walls downstream of the gate also contributed to air flow under the water nappe (Figure 7).

(a) (b)

(c) (d)

Figure 4. General configuration of the studied overshot gates: a) Gate A from upstream, b) Gate B from upstream, c) Gate C from downstream, d) Gate D from downstream.

Figure 5. Rigid connection between the gate leaves, and stiffness plates (GateA).

Figure 6. Aeration of the water nappe by the nappe-breakers for relatively low flow regime (Gate A, Flow Rate < 50 ft^3/s).

Figure 7. Aeration of the water nappe by the expanding side walls for relatively high flow regime (Gate A, Flow Rate > 50 ft^3/s).

Gate A had two bolted and welded gate leaves with a total crest length, *b*, of 22 ft. Each of the gate leaves had a slightly curved structure, so that the linear chord length from the bottom of the gate leaf to the crest of the gate leaf was identified as the length of the gate, L_G = 5 ft (Figure 2). Flow toward the gate was guided by concrete retaining walls. The retaining walls were built diagonally at a 45° angles to the flow direction in the upstream approach to the gate, but walls were aligned parallel to the flow direction in the vicinity of the gate leaf (see Figure 2). This alignment served to straighten the streamlines as perpendicular to the crest in the approach. The length of the approaching diagonal retaining walls was measured as 22 ft on both sides of the channel. The flow downstream of the gate was regulated by diagonal concrete retaining walls

that expanded at a 30° angle to the flow direction and extended a distance of 25 ft on both sides of the channel.

Gate B also had two connected gate leaves with b = 20 ft and L_G =6.3 ft. It had 12 ft-long diagonal concrete sidewalls aligned at a 45° angle to the approach flow direction. This structure was slightly different in terms of the approaching canal geometry that it had a concrete retaining wall on the right bank, upstream of the diagonal approach walls, aligned parallel to the flow direction. For the other gates the canal cross section upstream of the approach retaining walls was earthen. The straight retaining wall upstream of the diagonal approach to Gate B was 45 ft long (see Figure 4-b). Gate B also had expanding concrete sidewalls downstream that were similar to Gate A.

The bolted and welded connection for Gates A and B provided not only shear resistance but also moment resistance to the gate leaves. There are many ways to provide rigid connections for steel profiles but considering the dynamic effects of rapidly-varied flow profiles adjacent to the gates, using bolted and welded connections together was necessary to increase the stiffness of the gate leaves.

Gates C and D consisted of a single gate leaf each with L_G =5.8 ft and 6.08 ft, respectively. For Gate C, b = 17 ft and for Gate D, b = 15 ft. Gate C had approaching diagonal concrete retaining walls with a length of 10 ft and an angle of 45° to the flow direction. The length of the diagonal approaching sidewalls was measured as 12 ft for Gate D. Gate C and D had concrete sidewalls that expanded at 30° downstream with the length of 20.5 ft and 15 ft, respectively.

Expanding downstream sidewalls not only provided aeration of the nappe for relatively high flow regimes but also provided considerable space for streamlines to circulate freely. This

free circulation was particularly important for the flow measurement applications under submerged flow conditions.

Since Gate A and B were composed of two gate leaves, two air bladders were employed under the leaves to adjust the height of the weir, while Gate C and D were built as one piece including the bladder and the gate leaf. Moreover, each of the gates had restraining rubber straps underneath to prevent excessive rise of the gate leaves. These rubber straps immobilized the gate leaves at a limited level against the over-inflating of the air bladders resulting in back-flipping of the gate leaves. The max α that the gate can raised up was 65°.

The irrigation canal in which each of the gates were constructed was earthen. The canal composed of clay. Fine sand was deposited on the canal bed and the canal banks were covered by dense vegetation. Offtake structures for irrigation water diversion were placed at intervals upstream of each of the gate check structures. Downstream of the structures, concrete slabs were emplaced on the canal bed and rip-rap after the concrete slabs to dissipate turbulent energy.

3.1.2 Data Collection to Analyze Flow over the Overshot Gates

3.1.2.1 Discharge Measurements

Considering the physical conditions in the field, and acoustic Doppler current profiler (ADCP) was utilized to measure the discharge over each of the gates in this study. Average flow depths in the canal at the measurement locations upstream of the gates ranged from y = 3 ft. to y = 6.2 ft, as measured by the ADCP, and the measured top width of the canal at the gauging locations ranged from 15 ft to 30 ft, depending on the flow regimes. ADCPs employ the Doppler effect to measure velocity profiles within a channel cross section. In using the Doppler effect,

ADCPs conduct sound waves at a constant frequency and examine the responding echoes via scatterers in the water (RD Instruments, 1996). The channel bottom-tracking feature of the ADCP allows measurement of Doppler shifts to determine the flow velocity. Velocity profiles are sectioned into uniform pieces referred to as depth cells. The cross-sectional area of each depth cell is calculated by multiplying the width by the depth of the cell (Mueller et al., 2013). ADCPs measure the flow rate using the same principle as traditional point-velocity meters by summing the products of the cell cross sectional area by the respective velocity measured within each cell as described by Rantz (1981).

A 2,000 kHz StreamPro^{TM} ADCP produced by Teledyne RD Instruments was used in this study. The StreamPro^{TM} ADCP consists of a transducer, a tow arm, a float boat, and an electronics housing (Figure 8). The transducer is connected to the electronics housing via the transducer assembly.

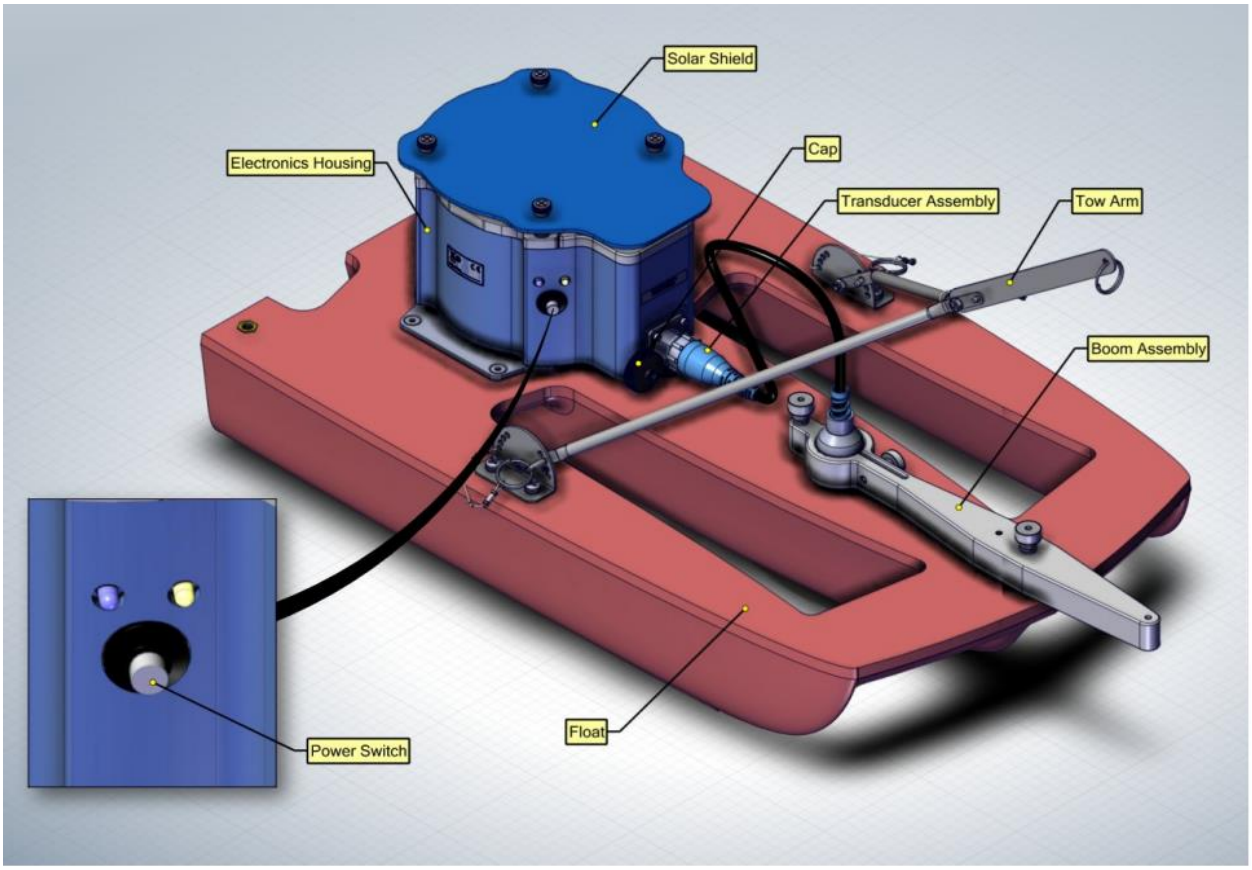

Figure 8. StreamPro ADCP (Adapted from the Teledyne StreamPro^{TM} ADCP Guide, 2015).

The ADCP can be deployed in two different transducer positions: in-hull or extended. The in-hull position of the transducer requires mounting the transducer in the boat itself, whereas the extended position can be set up in front of the boat utilizing a boom assembly. The in-hull position provides protection for the transducer against environmental effects. Since the canal flows carry debris, the in-hull position of the transducer was preferred for the flow measurement applications. A solar shield was attached to the top of the electronics housing to protect the device from the direct effects of sunlight.

Before starting the flow measurements, the ADCP was calibrated and equipped with firmware updates by the United States Geological Survey (USGS) Hydrologic Instrumentation Facility in Mississippi (Appendix 2). The accuracy of the ADCP was also tested with Rubicon Gates

installed in the canals via 1 flow measurement (due to restrictions of the canal operation just 1 flow rate measurement was completed). Percent error [(Q_{ADCP} – Q_{rubicon}) 100/ Q_{rubicon}] was calculated as -5.7%. The ADCP was also tested with other two ADCPs (with same frequency values) and a laser Doppler flowmeter in an unpublished study completed at Colorado State University in fall 2018. High agreement noted with the ADCP transducers and the laser Doppler flowmeter (about 2.5% deviation) for physical limitations of Water Mode 13 (explained later in this chapter). This agreement can support that the ADCP utilized in this study works accurately. The ADCP was operated by the WinRiver II real-time discharge data collection software (Teledyne Marine, 2016). The software sends commands to the ADCP and receives back collected data through a Bluetooth connection.

Flow measurements were performed at a position upstream of the gates located downstream of the nearest diversion. For Gate A, measurement was performed at a distance of 25 ft from the gate crest, for Gates B and C at 20 ft from the crest, and for Gate D at 18 ft from the crest. The StreamPro™ ADCP is designed as a tethered-type flow measurement device. Hence, a tethering platform was set up to drag the float boat back and forth along the cross-section. The platform consisted of two solid steel rods driven firmly into the ground on the opposite sides of the canal, a cable to tether the boat, and a roller-joint to facilitate the motion of the tethered boat along the cross section (Figure 9).

Figure 9. ADCP Operation Mechanism, along the Cross-Section Upstream of Gate C.

The ADCP was equipped with a four-beam transducer. Three-beam ADCPs measure three dimensional flow. In the four-beam version, there is an extra beam that measures the velocity error profile by measuring the vertical velocity difference between opposed beams to obtain more accurate results (Mueller et al., 2013). To reduce distortion effects, beam number 3 has been mounted at a 45° angle to the flow direction, as indicated in the user's manual of the device (Teledyne Marine 2015). It was difficult to keep the transducer beams in the desired position for flow rate values lower than 50 ft^3/s, due to the canal geometry's effect on the dragging mechanism. The ADCP was attached to the tethering cable with plastic ties on both sides of the device rather than using the tow arm in order to provide more stability.

The water mode, which describes the flow speed and depth of the device was set to either Mode 12 or Mode 13 depending upon the flow conditions and the physical conditions of the canal. Water Mode 13 was selected for $\bar{u}$ < 0.82 ft/s and y < 3.28 ft, whereas Mode 12 was used for $\bar{u}$ > 0.82 ft/s *and y* > 3.28 ft (Teledyne Marine, 2015). The ADCP utilized the bottom tracking feature which measures the velocity difference between the bottom of the canal and the transducer, in order to determine the flow velocity. According to Ramooz and Rennie (2010), bottom tracking assumes the channel bed is stationary but moving bed situations could cause deviations when using this feature. Thus, moving bed effects were considered in the canal during flow measurements. Tolerability of the moving bed conditions was evaluated before each of the discharge measurements. When moving bed status was not in a tolerable range, the required discharge calibrations were performed by the WinRiver II software automatically utilizing the USGS loop correction and stationary moving bed analysis (Mueller et al., 2013). Mueller et al. (2013) indicated that in severe moving bed situations, using GPS could more accurately determine the boat velocity.

Moving bed tests were completed before starting every discharge measurement. Two moving bed tests options were presented in the user's manual for the device. One option was a loop test, where the ADCP was dragged from one bank to the other while regarding the flow direction. The boat dragging process did not cease until the same bank was reached again (WinRiver II Software User's Guide, 2016). If the moving bed velocity is more than 0.04 ft/s and more than 1% of $\bar{u}$, moving bed effects should be considered (Mueller et al., 2013). The loop tests should be performed when the $\bar{u}$ > 0.82 ft/s (Environment Canada, 2013). The second option was the stationary moving bed test, which is employed when $\bar{u}$ < 0.82 ft/s (Environment Canada,

2013). For stationary tests, the ADCP was immobilized in the middle of the transect to obtain movement characteristics of the bed (WinRiver II Software User's Guide, 2016).

Moving bed conditions were not observed during this study except- for two measurements on Gate C. For these two measurements, $\bar{u}$ was recorded as 0.21 ft/s and 0.23 ft/s, respectively. These two measurements have not been employed in the analysis.

Once the moving bed tests were executed, other required steps were followed as prescribed in Teledyne Marine (2015). Mueller et al. (2013) pointed out that *y* can become too shallow at the banks for the ADCP to get accurate flow measurement values. Since the StreamPro™ ADCP can only be operated for 0.5 ft $\leq y \leq$ 6.6 ft. For the unmeasured zones near the canal banks, the data was extrapolated from the closest measured water column by the WinRiver II Software. The transducer of the ADCP is an immersed unit, as such an unmeasured zone exists between the operational distance of the transducer and the water's surface. Muller et al. (2013) stated that another uncertainty at the canal bed is due to the side-lobe interference. The side lobe interference is a reflection problem of the main transducer beam from the bottom. WinRiver II software offers three different methods to estimate the flow rate within unmeasured areas that are close to the water's surface and to the bottom of the canal. These three methods provide an extrapolation of the measured data to the unmeasured zones. The power law method was employed in this study to estimate the discharge at the canal bed and the water surface, with the power exponent set at 1/6 (Muste and Spasojevic, 2004). Gonzalez et al. (1996) suggested that measured velocity profiles are represented well by a power-law velocity function with an exponent of 1/6. Chen (1991) also found 1/6 to be a conventional power law coefficient for open channel problems.

At least four transects of the boat-mounted ADCP were performed along the cross section at each measurement location to increase the accuracy of the discharge estimation. Dynamic residual analysis was performed by the software after all data were collected from each transect. For the analysis, the ratio of the difference between the mean discharge value and each transect discharge value to the mean discharge value was calculated to be the residual control. The software verified that the maximum residual control was less than the maximum permissible relative residual (MPRR). The MPRR depends on the number of transects and a detailed table was presented in WinRiver II Software User's Guide (2016). If the required statistical condition could not be met, additional transects were employed. The number of transects ranged between 4 and 10 with average 4.72 for total. Finally, the velocity magnitude contours (Figure 10 and Figure 11), the flow rates, and $\bar{u}$ values were obtained.

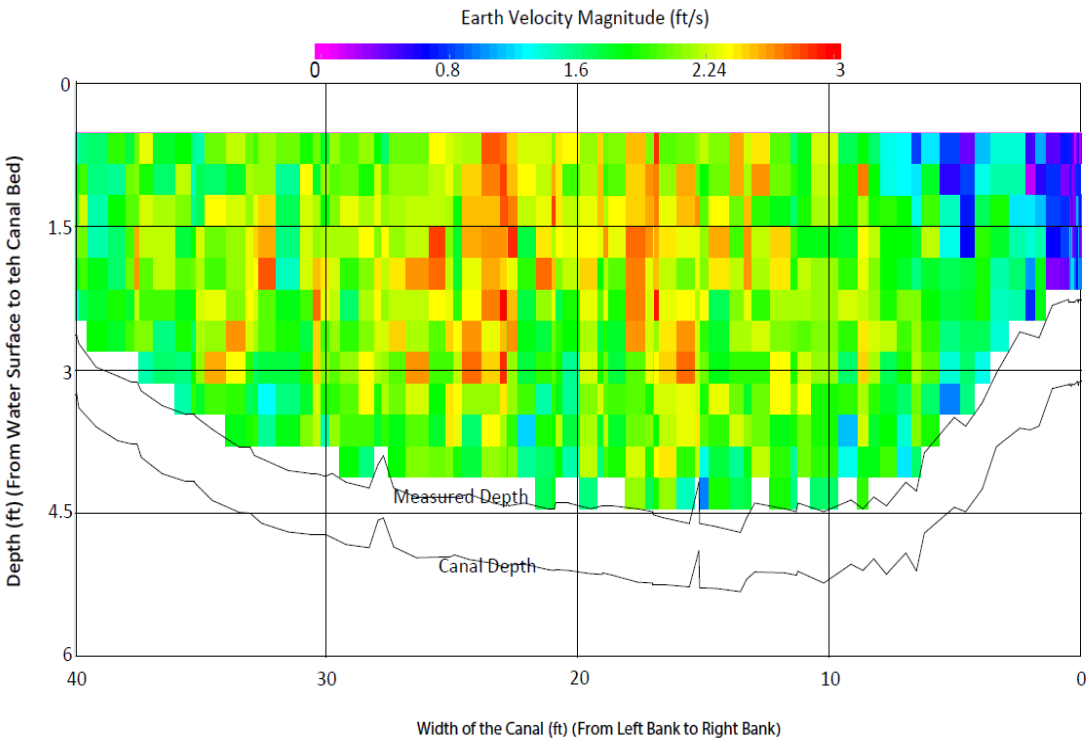

Figure 10. Velocity Magnitude Contour Sample along an Arbitrary Transect from Upstream of Gate A (Flow Rate = 286.4 ft^3/s, on 9 September 2017 at 2:35pm).

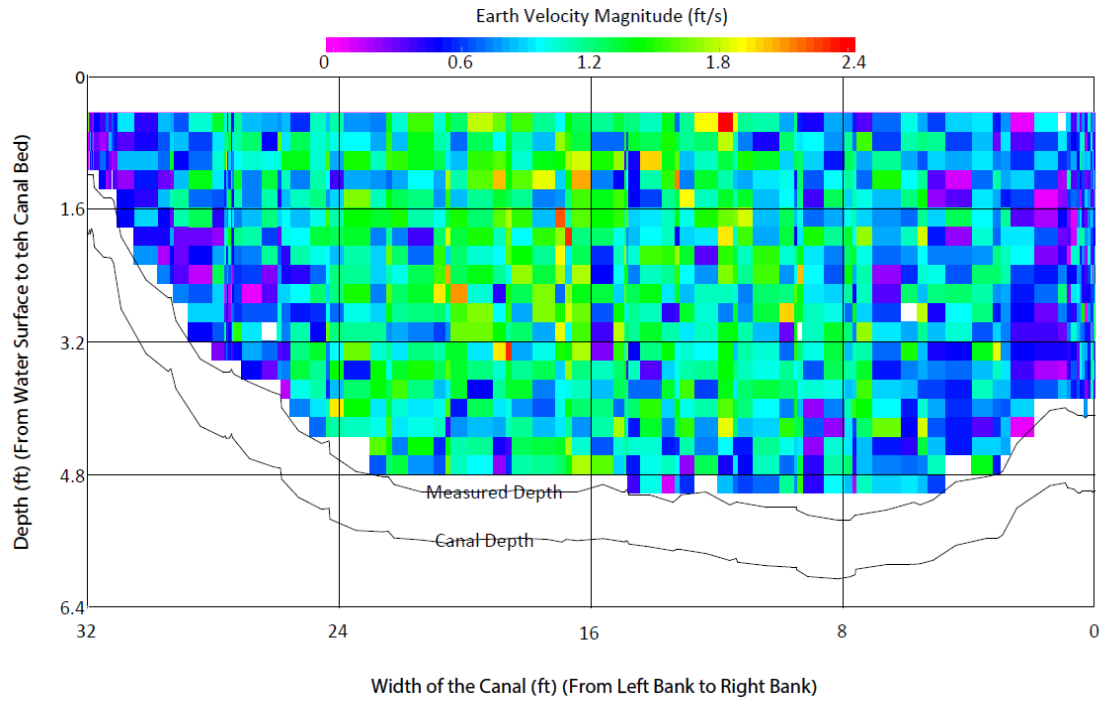

Figure 11. Velocity Magnitude Contour Sample along an Arbitrary Transect from Upstream of Gate B (Flow Rate =150.8 ft^3/s, on 18 August 2018 at 11:23 am).

3.1.2.2 Flow Depth Measurements

Measurements were made to determine the depth, *h*, over the crest of the gates. At Gates A, B, and D, free flow conditions were observed for all measurement periods during the irrigation seasons of 2017 and 2018. Free flow conditions occur when the tail-water level in the channel does not rise high enough to influence the discharge. Accordingly, only measurements of the upstream depth, *h,* needed to be made at the gates.

Although, each gate had a stilling well installed in the sidewall upstream to provide water level measurement, measurements for head-discharge calibration were not made at these locations. The distances of the stilling wells from crest of the gates were measured as only about 4 ft - 7 ft, which was not long enough to avoid the region of acceleration and drawdown toward the gate crest. However, the stilling well data were used to verify staff gauge measurement methods utilized in this study. To verify that staff gauge measurement is a reliable method, staff gauge measurements of depth below the top of the stilling well casing were pursued. These measurements were then compared with readings of CS451 series Campbell Scientific submersible pressure transducers that were mounted in the stilling wells at Gates A, B, and C (due to limited budget, Gate D could not be equipped with a data acquisition system). The transducers were made of stainless steel, temperature compensated, and submersible for water level measurement applications. The transducers were connected to Campbell Scientific CR300 series data-loggers, which converted electrical signals to suitable units for data acquisition. The data-loggers, were wired to small batteries in the control buildings for a power source. PC200W software was utilized to connect the transducers to the data-loggers. Wiring of the transducers to the data-loggers was completed following a wiring diagram prescribed by the software. Once

all the required connections were made, data collection programs were written to acquire the data. Signal intervals of the devices were specified as 10 seconds and output units were defined in the program as well. The same software was used to monitor and store the data (Figure 12). Pressure transducer readings from stilling wells versus staff gauge measurements in the stilling wells were examined by obtaining the coefficient of determination (R^2) for 84 data points. Values of R^2 were calculated as 0.99, 0.98, and 0.99 for Gates A, B, and C, respectively, indicating strong agreement between the two different methods of water level readings. This analysis showed that staff gauge measurement method is trustable and applicable for measuring *h*.

Figure 12. Water level measurements in the stilling well with a data acquisition system (left) and using a staff gauge at the stilling well at upstream of Gate B (right).

Once after verifying the accuracy of the staff gauge measurement method, staff gauge readings via a leveling bubble were used to measure *h* by utilizing the concrete retaining wall.

The vertical distance from the retaining wall to the water surface upstream was measured and subtracted from the vertical distance measured from the top of the retaining wall to the gate crest. Thus, *h* was obtained. Since the upstream flow depth measurement should be performed at a distance from the crest of at least 4*h* to 5*h,* staff gauge readings were taken 23 ft upstream from the crest of Gate A, 18 ft from the crest of the Gates B and C, and 16 ft from the crest of Gate D to avoid drawdown effects while remaining close enough to insure negligible energy head loss over the distance to the gate crest. The distance upstream between the staff gauge reading location and the location of flow rate measurements was about 2 ft for all gates. Staff gauge readings were conducted by a calibrated auto-level to prevent measurement errors due to construction flaws in the retaining walls (Figure13).

Figure 13. Upstream staff gauge readings and auto-level for flow depth measurements at Gate B.

The pressure transducer data were used not only to verify the method for measuring *h*, but also to indicate the flow conditions in the canal. During the 2017 irrigation season, water levels measured by the pressure transducers at 10-s intervals showed very small variability during the period of the ADCP measurements, verifying the assumption of steady flow conditions during the tests. Unfortunately, the data acquisition system was damage and could not be re-used for verification during the 2018 irrigation season. Nevertheless, observations of flow conditions during 2018 tests, compared to those in 2017, indicated steady flow.

For $Q \geq 173.5$ ft^3/s, the water level downstream of the gate reached the crest level for Gate C. For this reason, another pressure transducer was mounted downstream of Gate C to measure flow depth above the crest for potentially submerged flow conditions. The average water level elevation over the course of the ADCP measurements was computed for use in downstream flow depth analysis since significant turbulence and eddies developed in the tail-water at the outfall.

The drawdown effect between the location of *h* measurements and the stilling well locations was examined upstream of the gates. The drawdown was calculated as the difference between *h* and the water level over the crest that was measured at the stilling wells. Maximum drawdown values were observed as 0.09 ft, 0.08 ft, and 0.06 ft for Gates A, B, and C, respectively, and were analyzed as a function of $\bar{u}$ upstream of the gates (due to inconvenience of the stilling well at Gate D, drawdown could not obtain for this gate). Figure 14 shows the relationship between drawdown and $\bar{u}$ for Gate A.

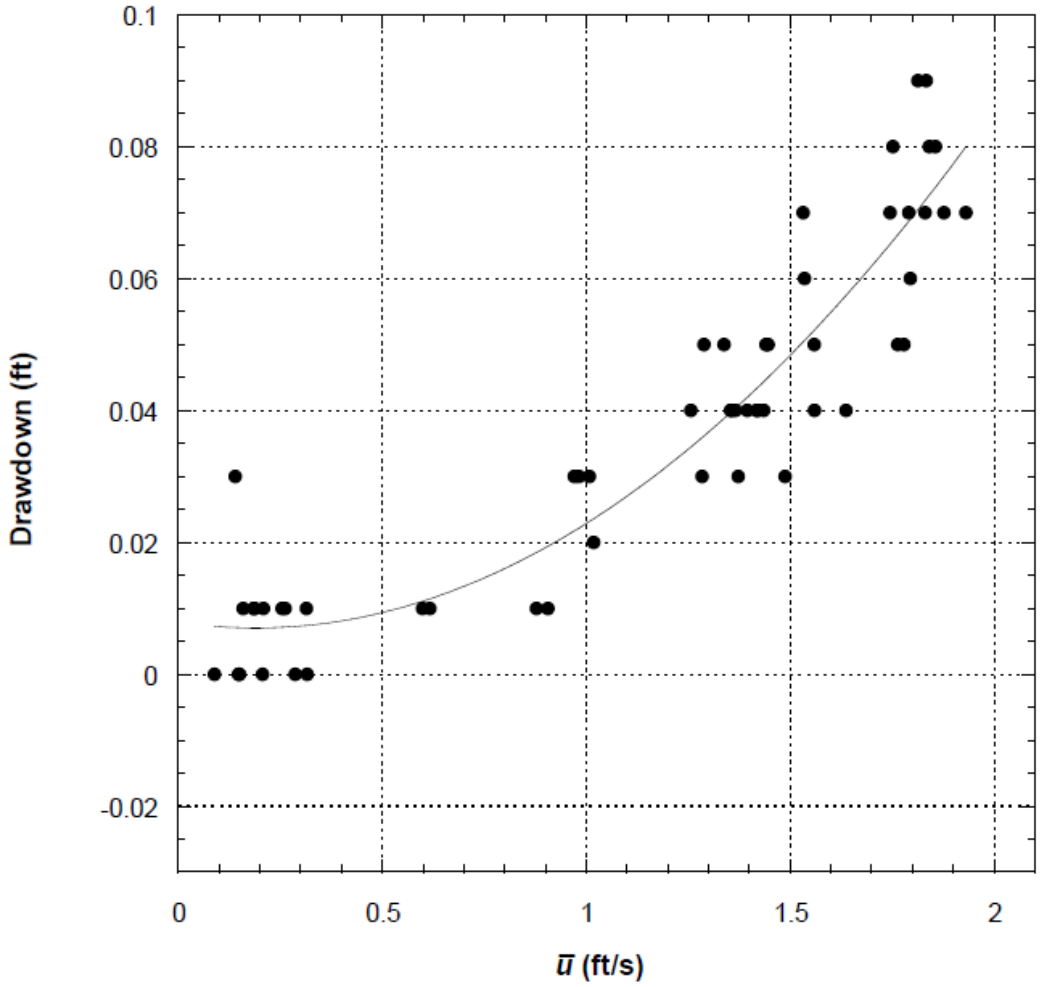

Figure 14. Drawdown values as a function of average velocity for Gate A.

3.1.2.3 Determination of the Total Hydraulic Head

Velocity head in the channel at the upstream measurement location was taken into account in this study, whereas it has been neglected or its effect simply embedded in the discharge coefficient in the majority of previous studies. To determine the velocity head $\bar{u}$ was computed as the average velocity values measured over the upstream cross section with the ADCP were used. Employing a kinetic energy (velocity head) correction factor, the upstream velocity head [L] was evaluated as:

$$\Lambda \frac{\bar{u}^2}{2g} \tag{6}$$

In practical open channel applications, velocity profiles often are assumed to be uniform over the cross section, but in reality, the velocity profiles are not uniform. However, the actual variability of velocity profiles within an open channel cross section depends upon the roughness of the stream perimeter, the physical features of the stream bed, the geometry of the cross section, etc (Hulsing et al., 1968). The kinetic energy correction factor is introduced to account for this variability when computing kinetic energy head in a channel cross section. It is defined as the ratio of the true kinetic energy flux to the kinetic energy flux computed using $\bar{u}$ (Subramanya 1982):

$$\Lambda = \frac{\int u^3 dA}{\bar{u}^3 \bar{A}} \tag{7}$$

In this study the integral in the numerator of Eq. 7 is approximated as the summation of the cube of the *u* values measured ADCP within each depth cell of the cross section, and $\bar{u}$ is calculated as the arithmetic average of the u measurements within all of the depth cells. Subramanya (1982) suggested that the value of Λ typically is 1.15 - 1.50 for natural channels torrents.

To calculate Λ, WinRiver II software was utilized. Initially, the velocity magnitude output files were created to obtain the velocity magnitude for each cell. Dragging distance output files, also were created to obtain the width of the cells. Knowing the depth and the width of the cells, the velocity magnitude of each cell, the average velocity of the flow, and the average cross-sectional area allowed for calculation Λ values. Using 10 different measurements with a total of 40 transects from four different gates for Q values ranging 30 – 300 ft^3/s, Λ was calculated as

1.075 - 1.12. The average Λ was calculated as 1.10 for the chosen transects. Hence, a Λ of 1.10 was used in the total energy head calculations for this study.

3.2.4 Measurements of the Inclination Angles of the Gates

Values of α for each of the measured gate flow conditions were determined based on the staff gauge readings. Measurements were made on both sides of the gates along the cross section in order to avoid the misleading effects of gate fluctuations. Fortunately, however, significant fluctuation was not observed for the gates. Staff gauge measurements were performed by measuring the vertical distance from the top of the adjacent retaining wall to the crest of the gate. The horizontal distance from the crest of the gate to a reference point, such as the steel bridge that was mounted across the gate, was measured as well. Thus, the specific locations of the gate crest have been determined. After determining the specific locations of the crests during the irrigation seasons, at the end of the irrigation seasons (during no-flow conditions), actual α values were obtained by measuring the distance of these specific locations from bottom of the gate leaves (Figure 15). Calibrated auto levels were used to increase the accuracy of the collected data.

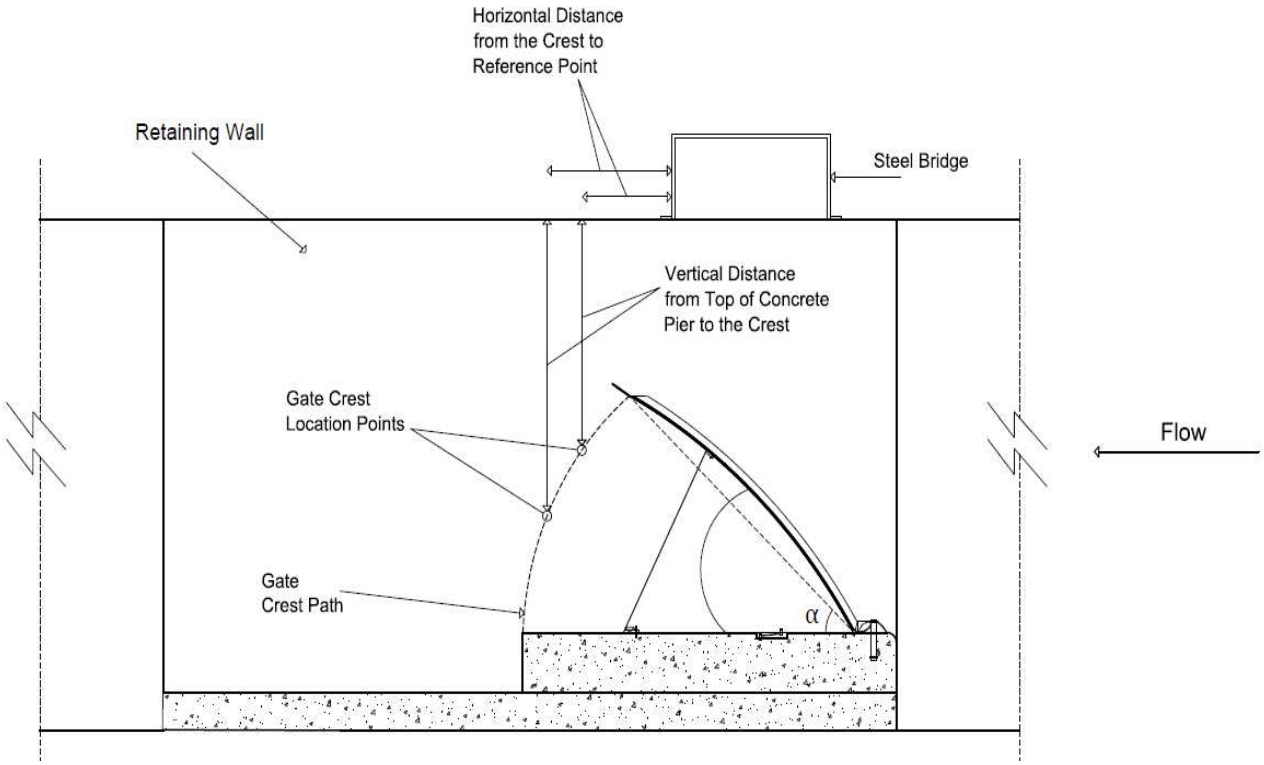

Figure 15. Staff gauge measurements of gate inclination angle.

Verification of the staff gauge inclination angle measurement method, was provided by Campbell Scientific SR50-A series sonic distance sensors that were mounted at Gate A and Gate C. Sonic distance sensors are capable of measuring desired distances by recording the time difference between sent and retrieved ultrasonic pulses (Campbell Scientific, SR50A Instruction Manual, 2006). Two plastic pipes were employed to setup a measuring mechanism for the sonic level sensors. One pipe was mounted to the crest of the gate as a hinge connection to provide flexibility for gate inclination (Figure 16). Another pipe, which is smaller in diameter was mounted on a concrete retaining wall as a fixed connection, and the smaller pipe slid within the larger pipe concordant with the gate motion. The sonic level sensors were mounted on the pipe at the fixed connection. Thereby, the distance from the level sensor to the crest of the gate was measured. The sonic level sensors were mounted to the same data-loggers as were the pressure transducers

in the stilling wells. Wiring and connection processes of the water level sensors were completed similarly to those for the pressure transducers, as prescribed in the PC200W software.

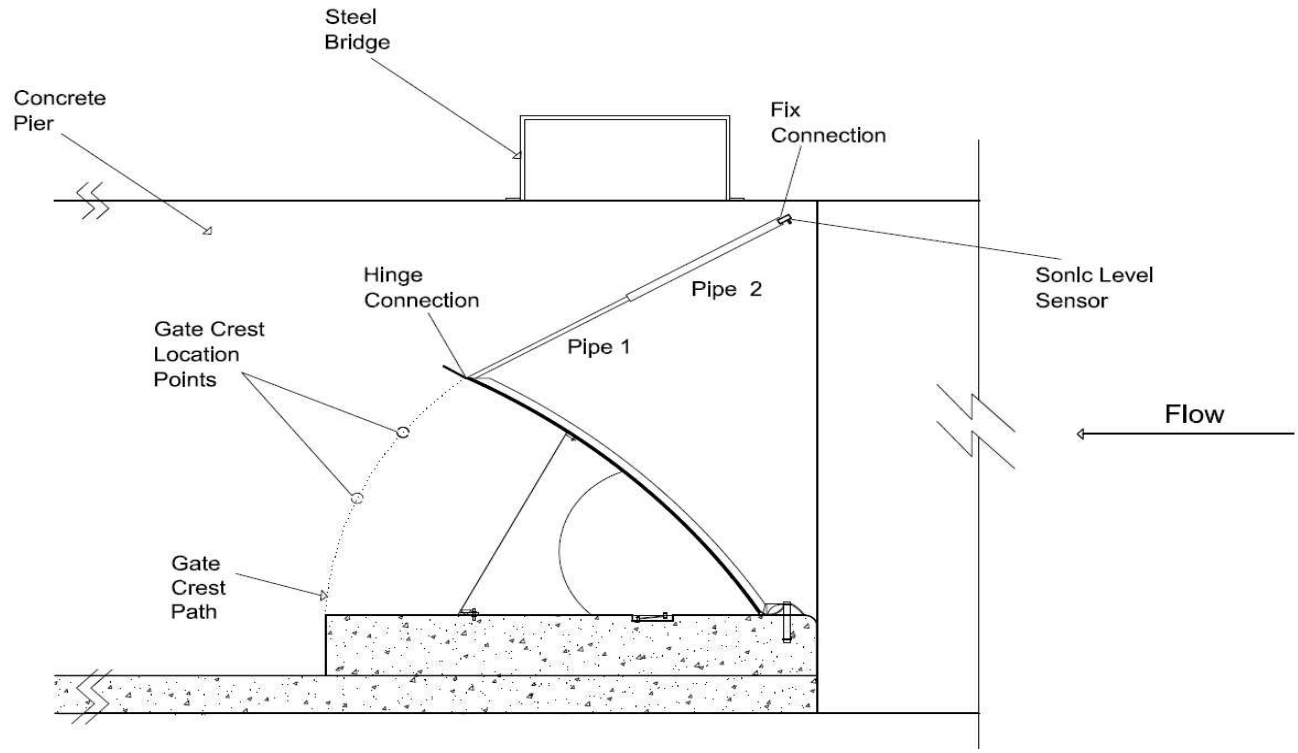

Figure 16. Gate inclination angle verification using sonic level sensor and sliding pipe configuration.

To verify the staff gauge measurement method for the gate's inclination, the distance from the gate crest to the level sensors was measured by staff gauge. These distances were then compared with sonic level sensors measurements. Root Mean Squared Errors (RMSE) and Normalized Root Mean Squared Error (NRMSE) of the distances from crest to level sensor locations were calculated as 0.08 and 0.01 for Gate A and 0.16 and 0.02 for Gate C, respectively (due to the limited budget, level sensors could not be employed for angle verification). Figure 17 displays photographs of the gate inclination measurements.

(a)

(b)

Figure 17. Measurement of the inclination angles: a) sonic level sensor at Gate C and A, b) staff gauge measurements at Gate A and B.

3.2 Obtaining the Discharge Coefficient as a Function of Inclination Angle under Free Flow Conditions

Eq. 1 represents the discharge of sharp-crested weirs as a function of *H*, *b*, and the discharge coefficient. It was rearranged as prescribed in Ferro (2011) in terms of *H*, as below:

$$H=\left(\frac{9}{8C_d^2}\right)^{1/3}\frac{Q^{2/3}}{b^{2/3}g^{1/3}} \tag{8}$$

by setting:

$$k_s=\frac{Q^{2/3}}{b^{2/3}g^{1/3}} \tag{9}$$

$$t=\left(\frac{9}{8\,C_d^2}\right)^{1/3} \tag{10}$$

Eq. 8 was rewritten relative to the weir height to obtain a dimensionless relationship:

$$\frac{H}{p}=t\left(\frac{k_s}{p}\right) \tag{11}$$

3.2.1 Dimensional Analysis

Dimensional analysis was used in this study to determine the form of the head-discharge relationship of overshot gates using field data. Sonin (2001) indicated that dimensional analysis is an effective tool that provides simpler forms for complex problems in order to obtain quantitative results. The main purpose of dimensional analysis is to reduce the number of variables required for experimental studies. Experiments are not only expensive, but also time consuming. To perform dimensional analysis, dimensional homogeneity is essential. Dimensional homogeneity is uniformity of the units on both sides of the equation. Singh (2012) presented that four independent dimensions, which are mass [M], length [L], time [T], and temperature, are

used to describe the state of the physical characteristics of fluid mechanics problems. The author also indicated that the units of temperature are not applied for conditions of incompressible flow. Thus, mass, length and time were selected as the reference dimensions needed to perform dimensional analysis in this study.

3.2.2 Buckingham – Π Theorem

Buckingham – Π theorem, can be described as a technique that derives dimensionless parameters from known variables. Chandler (1998) explained that for an equation with several variables, deduction to a relationship from the equation is possible with the help of dimensionless products. The number of dimensionless products should equal the number of variable minus the number of reference dimensions. These dimensionless groups were termed as π groups by Buckingham – Π theorem, and were independent of each other. White (1994) recommended the following steps to accomplish Buckingham – Π analysis. First, evaluate the problem and determine the independent variables. Second, note the dimensions of the variables and identify the number of π groups. Third, systemize the dimensionless groups, to be dimensionless and indicate the results in the following form: $\pi_1 = \Phi\ (\pi_2,\ldots\ldots\pi_{n-k})$. Barenblatt (1987) further stated that in order to obtain more appropriate results, acquiring new similarity parameters is achievable by incorporating the original dimensionless groups.

3.2.3 Self – Similarity (SS) and Incomplete Self – Similarity (ISS) Theory

Self – similarity can be explained as having the same features on any scale for objects. Barenblatt (1996) stated that ‘‘physical phenomena are called similar if they differ only in respect of numerical values of the dimensional governing parameters; the values of the corresponding dimensionless parameters $\pi_1,\ldots..\pi_m$ being identical.’’ Ferro (2000) also indicated that ‘‘a

phenomenon is defined as self-similar in a given π_n dimensionless group when the functional relationship $\pi_1 = \Phi(\pi_2,\ldots\ldots\pi_n)$ representing the physical phenomenon is independent of π_n." Ferro and Pecoraro (2000) explained that the boundary conditions are an identifier when solving for complete self-similarity and complete self-similarity occurs where Φ is not zero and is prone to reach a finite limit. When the phenomenon does not depend on π_n, the following functional relationship of the phenomenon can be termed $\pi_1 = \Phi(\pi_2, \pi_3, \ldots\ldots\ldots\ldots, \pi_{n-1})$. Barenblatt (1979, 1987) noted that incomplete self-similarity occurs where π_n goes to zero or infinity, and regarding limits of the Φ function equals to 0 or infinity, such that the following function can be obtained to express the incomplete self-similarity:

$$\pi_1 = \pi^a{}_n \Phi_2 (\pi_2,\pi_3,\ldots\ldots\ldots\pi_{n-1}) \quad (12)$$

The head-discharge relationship for an Obermeyer-type pneumatically automated gate is expressed as a function of nine variables:

$$\Psi (Q, H, p, b, g, \mu, \rho, \sigma, \sin\alpha) = 0 \quad (13)$$

where Ψ is the functional symbol, μ is the dynamic viscosity [M/TL], ρ is the water density [M/L^3], and σ is the surface tension of water [M/T^2].

Wahlin and Replogle (1994) assumed that the streamlines approaching an overshot gate are straightened before reaching the crest since the contraction was set up just along the hinge and the distance between the hinge and the crest of the gate was sufficiently long. Thus, the gates were assumed to behave as suppressed weirs for laboratory tests. In this study, with the same approach, the overshot gates were presumed to be fully suppressed. Thus, a contraction effect was not considered in Eq. (13).

To check the validity of the assumption of straight streamlines in the approach to the crest, and a fully-suppressed behavior of the overshot gates, a computational fluid dynamics (CFD) model was employed using a software (ANSYS Version R18.1, 2017). The CFD model was setup to simulate the streamlines that passed over the crest of the overshot gate. ANSYS R18.1 software was utilized, and employed the volume of fluid method to address free-surface multiphase modelling problems for open channel applications. The volume of fluid method is based on the fractional fluid volume in the cells, as described in Hirt and Nichols (1981). To obtain the streamline paths, a CFD model was created for Gate A using the known geometry. For the volume of fluid applications, the two fluid phases were defined as air and water for this multi-physics flow model. Density of water and air were determined as 998.2 kg/m^3 and 1.225 kg/m^3, respectively. The boundary conditions of the flow were then determined. Since the flow velocities were obtained from the ADCP measurements upstream, the inlet boundary was identified as a velocity-inlet (boundary condition with a known velocity profile) at the upstream. Resulting from free surface modelling, the boundary conditions above and at the downstream side of the flow, were described as pressure outlets to represent those that were open to the atmosphere (gauge pressure value is zero). The volume of fluid fraction was defined as 1, representing a full volume of fluid, for the inlet boundary. The volume of fluid fractions was set to 0 at the pressure outlet boundaries (atmosphere and outlet flow), since the fluid was not existent at the initial conditions. For solid boundaries, such as the canal bed, gate leaf and concrete piers, smooth stationary wall boundary option of the software was preferred. The standard k-ε turbulence model was selected, described by Chen and Kim (1987) as “the most widely used isotropic two-equation turbulence model”. The initialization of the flow was

processed with the software's hybrid initialization feature, which utilizes the Laplace equation. Time – step analysis characteristics were also identified for the flow simulations. Transient flow simulation results were analyzed in terms of the streamlines (Figure 18). According to the CFD-Post User's Guide (2015), the track of a zero-mass element is defined as a streamline in the software, and is determined by the Runge – Kutta Method (Cash and Karp 1990). As can be seen from Figure 18, the streamlines that pass over the crest of the weirs can be considered straight and adequately parallel for the analysis of flow over the overshot gates.

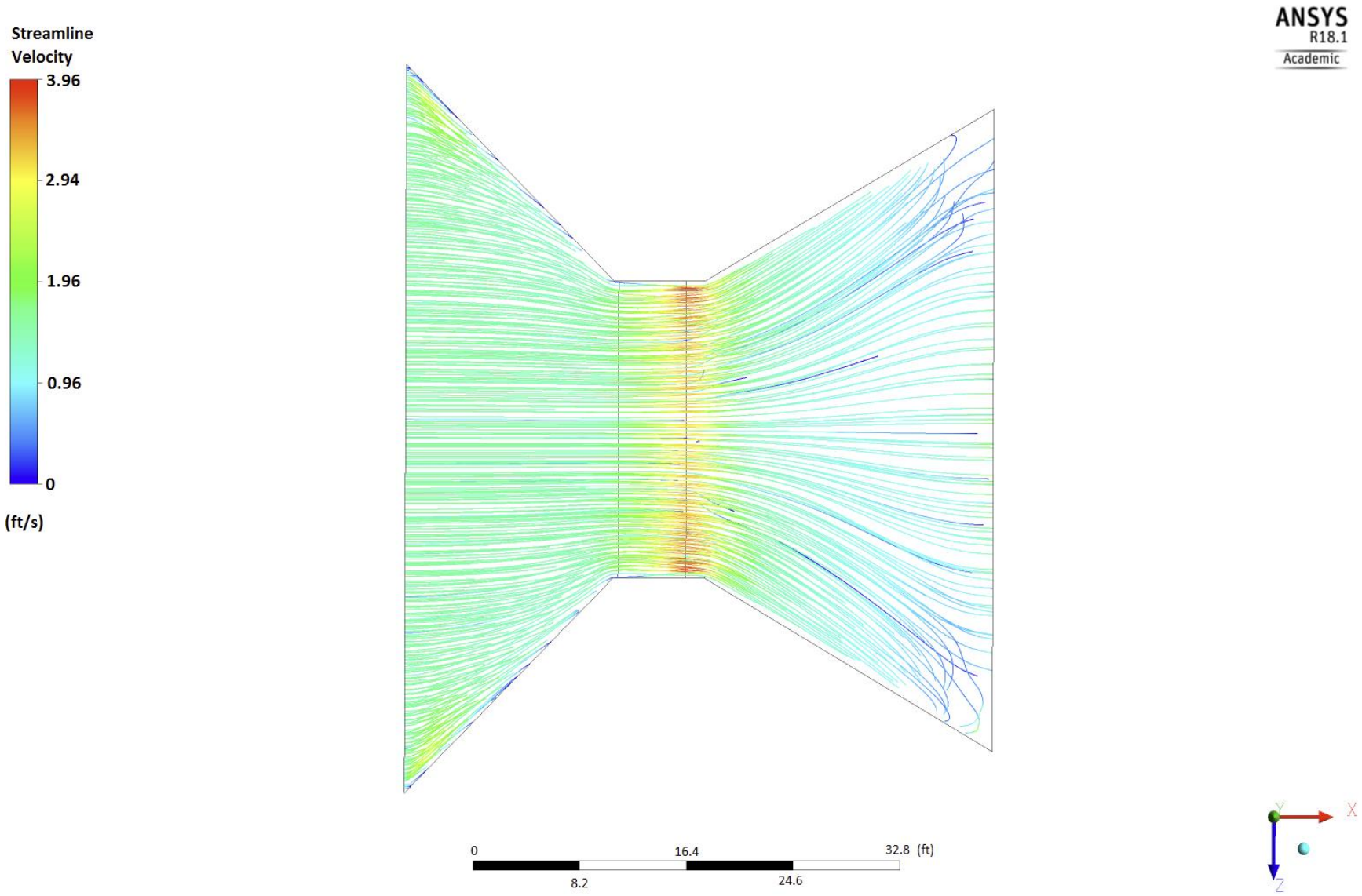

Figure 18. Streamlines flow paths for Obermeyer-type pneumatically automated gates simulated using ANSYS R18.1.

3.2.4 Applying the Buckingham – Π Theorem and ISS Theory to the Collected Data

Nine different variables were identified in Eq. 13 and the three selected reference dimensions were mass, length, and time. Therefore, six (i.e. 9 – 3) dimensionless groups were formed. Independence of the physical phenomenon represented in Eq. 13 from selected measurement units has been noted, and Eq. 13 was written with respect to π theorem (Barenblatt 1979, 1987; Ferro 1997, 2000; Di Stefano et al. 2016) as:

$$\pi_1 = \Phi\,(\pi_2, \pi_3, \pi_4, \pi_5, \pi_6) \tag{14}$$

Repeating variables were identified as the p, g, and ρ. The main criterion for selecting these variables was the distribution of units. The repeating variables contained mass, length and time units. The variable p has length units $[\mathrm{L}]$, while the g is in length per time squared units $[\mathrm{LT}^{-2}]$, and ρ is in mass per cubic length units $[\mathrm{M\ L}^{-3}]$. Π functions were formed and combined, as shown in Ferro (2011) below:

$$\pi_1 = p^x g^z \rho^w H \tag{15}$$

$$\pi_1 = L^x L^z T^{-2z} M^w L^{-3w} L \tag{16}$$

$$0 = x+z+1-3w \tag{17a}$$

$$0 = -2z \tag{17b}$$

$$0 = w \tag{17c}$$

The group for Eq. 13 was written for the π_1 dimensionless group by equating the sum of the exponents of each of the repeating parameters to zero in order to obtain one of the dimensionless group. By solving this equation group, exponents of the π_1 dimensionless group

were determined as x = -1, z = 0, and w = 0. Thus, by applying exponents to the dimensionless group, the following forms of Eq. 15 were obtained:

$$\pi_1 = p^{-1}\, g^0\, \rho^0\, H \tag{18}$$

$$\pi_1 = \left(\frac{H}{p}\right) \tag{19}$$

As described in Ferro (2011), the other dimensionless groups were obtained using the same approach as for π_1.

$$\pi_2 = p^x\, g^z\, \rho^w\, Q \tag{20}$$

$$\pi_2 = L^x\, L^z\, T^{-2z}\, M^w\, L^{-3w}\, L^3\, T^{-1} \tag{21}$$

$$0 = x+z-3w+3 \tag{22a}$$

$$0 = w \tag{22b}$$

$$0 = -2z-1 \tag{22c}$$

By solving the equation system 22a, 22b, and 22c, exponents were obtained as x = -5/2, z = -1/2, and w = 0 and the π_2 dimensionless group was obtained as follows:

$$\pi_2 = p^{(-5/2)}\, g^{(-1/2)} \rho^0\, Q \tag{23}$$

$$\pi_2 = \frac{Q}{p^{(5/2)} g^{(1/2)}} \tag{24}$$

To obtain the third dimensionless group π_3:

$$\pi_3 = p^x\, g^z\, \rho^w\, b \tag{25}$$

$$\pi_3 = L^x\, L^z\, T^{-2z}\, M^w\, L^{-3w}\, L \tag{26}$$

Exponents for the third dimensionless group were acquired as $x = -1$, $z = 0$, and $w = 0$, and the third dimensionless group had the following forms:

$$\pi_3 = p^{-1}\, g^{0}\, \rho^{0}\, b \tag{27}$$

$$\pi_3 = \frac{b}{p} \tag{28}$$

To obtain the fourth dimensionless groups:

$$\pi_4 = p^{x}\, g^{z}\, \rho^{w}\, \mu \tag{29}$$

$$\pi_4 = L^{x}\, L^{z}\, T^{-2z}\, M^{w}\, L^{-3w}\, M\, L^{-1}\, T^{-1} \tag{30}$$

Exponents for the fourth dimensionless group were $x = -3/2$, $z = -1/2$, and $w = -1$, and the fourth dimensionless group had the following forms:

$$\pi_4 = p^{(-3/2)}\, g^{(-1/2)}\, \rho^{-1}\, \mu \tag{31}$$

$$\pi_4 = \frac{\mu}{p^{(3/2)} g^{(1/2)} \rho} \tag{32}$$

To obtain the fifth dimensionless groups:

$$\pi_5 = p^{x}\, g^{z}\, \rho^{w}\, \sigma \tag{33}$$

$$\pi_5 = L^{x}\, L^{z}\, T^{-2z}\, M^{w}\, L^{-3w}\, M\, T^{-2} \tag{34}$$

Exponents for the fifth dimensionless group were acquired as $x = -2$, $z = -1$, and $w = -1$ and the fifth dimensionless group had the following forms;

$$\pi_5 = p^{-2}\, g^{-1}\, \rho^{-1}\, \sigma \tag{35}$$

$$\pi_5 = \frac{\sigma}{p^2 g \rho} \tag{36}$$

To obtain the sixth dimensionless group:

$$\pi_6 = p^{x}\, g^{z}\, \rho^{w}\, \sin\alpha \tag{37}$$

$$\pi_6 = L^{x}\, L^{z}\, T^{-2z}\, M^{w}\, L^{-3w} \tag{38}$$

Exponents for the sixth dimensionless group were acquired as $x = 0$, $z = 0$, and $w = 0$, and the sixth dimensionless group had the following forms:

$$\pi_6 = p^0 g^0 \rho^0 \sin\alpha \tag{39}$$

$$\pi_6 = \sin\alpha \tag{40}$$

Since Barenblatt (1979, 1987) indicated that combining dimensionless groups could result in new dimensionless groups, the following form of the stage – discharge relationship was acquired (Ferro 2011; Di Stefano et al. 2016; Bijankhan and Ferro 2017):

$$\pi_{2,3} = \frac{\pi_2^{(2/3)}}{\pi_3^{(2/3)}} = \frac{Q^{(2/3)}}{g^{(1/3)} p^{(5/3)}} \quad \frac{p^{(2/3)}}{b^{(2/3)}} \tag{41}$$

$$\pi_{2,3} = \frac{k_s}{p} \tag{42}$$

$$\pi_{4,3,2} = \frac{\pi_2}{\pi_4 \pi_3} = \frac{Q}{p^{(5/2)} g^{(1/2)}} \quad \frac{p^{(3/2)} g^{(1/2)} \rho}{\mu} \quad \frac{p}{b} \tag{43}$$

$$\pi_{4,3,2} = \frac{\rho Q}{\mu b} = Re \tag{44}$$

$$\pi_{5,1} = \frac{\pi_1^2}{\pi_5} = \frac{H^2}{p^2} \quad \frac{p^2 \rho g}{\sigma} \tag{45}$$

$$\pi_{5,1} = \frac{\rho g H^2}{\sigma} = We \tag{46}$$

As can be seen from Eq. 44 and Eq. 46, the combined dimensionless groups were assigned as the Reynolds number, *Re*, and Weber number, *We*, respectively. *We* is a dimensionless ratio that is used in fluid mechanics to analyze the interface of multiphase fluids. Open-channel flow can be categorized as multiphase, due to the fact that the water interacts with the air. *We* can be described as the ratio of the inertial effects of the fluid to the surface tension effects. In a sense, *We* indicates whether the kinetic energy is dominant over the surface energy. When *We*

is high, the kinetic energy is dominant. *Re* is another dimensionless parameter commonly employed to distinguish laminar flow from turbulent flow conditions. *Re* can be interpreted as the ratio of flow inertia to viscous forces. When the viscous forces are dominant, the flow is categorized as laminar, while in turbulent flow conditions, flow inertia is dominant.

Aydin et al. (2011) stated that different forms of *We* and *Re* are possible. Furthermore, Shen (1981) stated that it could be more legitimate to express *Re* and *We* as functions of the hydraulic head, μ, and ρ because hydraulic head is the determinative term and velocity is a function of hydraulic head. Within this paradigm, Ferro (1997, 2011), Di Stefano (et al. 2016), and Bijankhan and Ferro (2017) defined *Re* and *We*, similar to Eq. 44 and 46, respectively. The main discrepancy between *Re* and *We* definitions and Eqs. 44 and 46 was that the researchers neglected the velocity head effect, while the total upstream energy head relative to the crest was taken into account in this study. Thus, the total hydraulic energy head was determined to be a dominant term in *Re* and *We* equations.

The well-known forms of *Re* and *We* Equation are stated below:

$$Re = \frac{VL}{\nu} \tag{47}$$

$$\mathrm{We} = \frac{\rho V^2 l}{\sigma} \tag{48}$$

where *L* and *l* are characteristic linear dimensions [L] and V is fluid velocity, taken as $\bar{u}$ in this study. , and v is kinematic viscosity [L/T^2]. According to π theorem:

$$\pi_1 = f(\pi_{2,3}\ ,\ \pi_{4,3,2}\ ,\ \pi_{5,1}\ ,\ \pi_6) \tag{49}$$

Thus, the final form of the equation was acquired as follows:

$$\frac{H}{p} = f\left(\frac{k_s}{p},\ Re,\ We,\ \sin\alpha\right) \tag{50}$$

Tracy (1957), De Martino and Ragone (1984), and Rao and Shukla (1971) showed that *Re* and *We* could be neglected when *h* was sufficiently high, such that the viscous and tension forces were negligible. The negligibility of the *We* and *Re* were assumed in this study as well.

According to Swamee et al (2001), the water temperature and surface tension relationship could be expressed with the following equation:

$$\sigma = 0.0762 \exp(-0.00233\ T) \tag{51}$$

where T is the water temperature in units of degrees Celsius and σ is in units of Newtons per meter.

Water temperature was recorded during this study using Campbell Scientific CS451 pressure transducers. These transducers were also used to verify the flow depth measurements during the study. As can be seen from Eq. 51, lower temperature leads to higher surface tension. To verify that *We* was negligible, a combination of worst case scenarios, which minimizes *We* was considered and the lowest temperature value was selected from the data-logger recordings. The lowest temperature was recorded for Gate A (Montgomery Check) on the 25th of August as 16.34° Celsius.

To obtain a lower *We*, the lowest value of *H* was chosen for Eq. 46. The lowest was H = 0.64 ft, also measured at Gate A (Montgomery Check). Surface tension was determined according to Eq. 51, as below:

$$\sigma = 0.0762 \exp(-0.00233\ (16.34)) = 0.073583\ \ N/m \tag{52}$$

Eq. 46 was solved for ρ = 999.03 kg/m^3 at 16.34° Celsius, g = 9.81 m/s^2, and H = 0.64 ft. = 0.2 m. The following equation shows the resulting *We* considering *H* as a function of *V*:

$$We = \frac{\rho\, g\, H^2}{\sigma} = \frac{(999.03)(9.81)(0.64/3.28)^2}{0.073583} = 5071 \quad (53)$$

Sargison and Percy (2009) investigated varying slopes for broad crested weirs and indicated that if *We* was greater than 1, the surface tension was negligible. Thus, in this study the *We* clearly indicated that the surface tension was negligible since *We* = 5071 >> 1.

To obtain the lowest *Re* in this study and examine if it could be neglected, the worst case scenario was investigated, with the *Q*, the highest μ, which occurs at the lowest temperature, and the widest *b*. The widest gate was Gate A (Montgomery Check) where not only the lowest flow rate was recorded, but the lowest temperature was also observed. At 16.34° Celsius, the μ = 1.1081 MPa.s = $1.108*10^{-3}$ kg/m.s. The lowest *Q* with the lowest *H* was recorded for Gate A (Montgomery Check) on the 19th of August 2017 as 27.9 ft^3/s = 0.79 m^3/s, with *b* =6.71 m. The density of the water was 999.03 kg/m^3. Considering *V* can be represented as *Q/A* of Eq. 44 was solved to obtain:

$$Re = \frac{\rho\, Q}{b\, \mu} = \frac{(999.03)(0.79)}{(6.71)(0.001108)} = 106156 \quad (54)$$

Arvanaghi and Oskuei (2013) showed that for *Re* greater than 20,000 (however, the researchers did not define the *Re*), the discharge coefficient of the sharp crested weir did not change. In this study, the *Re* effect was neglected, since even in the worst-case scenarios, the Reynolds number was approximately 100,000.

Given the negligibility of *We* and *Re* numbers, Eq. 50 takes the following form:

$$\frac{H}{p} = f\left(\frac{k_s}{p}, \sin\alpha\right) \quad (55)$$

With the help of the incomplete self-similarity theory mentioned before, Eq. 55 then takes the following form (Ferro 2011; Di Stefano et al. 2016; and Bijankhan et al. 2013):

$$\frac{H}{p}=m\left(\frac{k_s}{p}\right)^n \quad (56)$$

where *m* and *n* are constants.

3.2.4.1 Obtaining the Parameters *m* and *n* as Functions of the Gate Inclination Angle

Bijankhan and Ferro (2017) suggested that both the coefficient *m* and the exponent *n* in Eq. 56 could be obtained as functions of α for overshot gates. The researchers presented second-order polynomial equations for *m* and *n* as functions of α to obtain the head-discharge relationship for overshot gates. In this study, the same approach was used by applying a curve-fitting method to the power function (Eq. 56) using the field data gathered for all of the gates to determine the *m* and *n* for different α values (Figures 19-26). KaleidaGraph data fitting software was employed for the process.

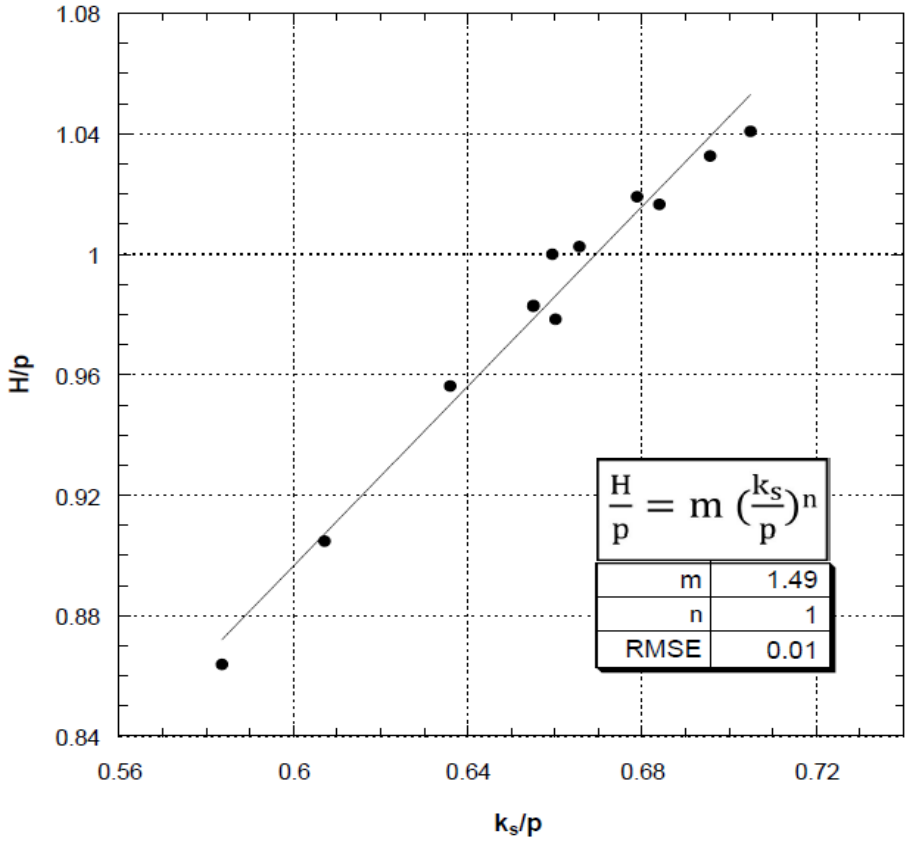

Figure 19. Coefficient and exponent of Eq. 56 for inclination angle = 22.8°

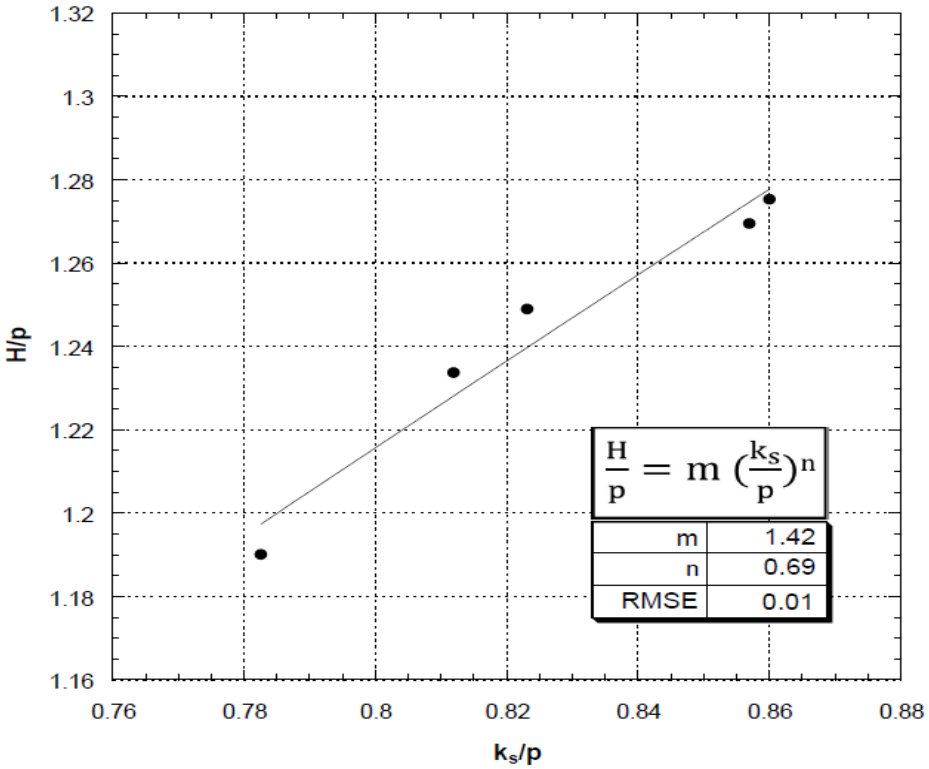

Figure 20. Coefficient and exponent of Eq. 56 for inclination angle = 23.6°

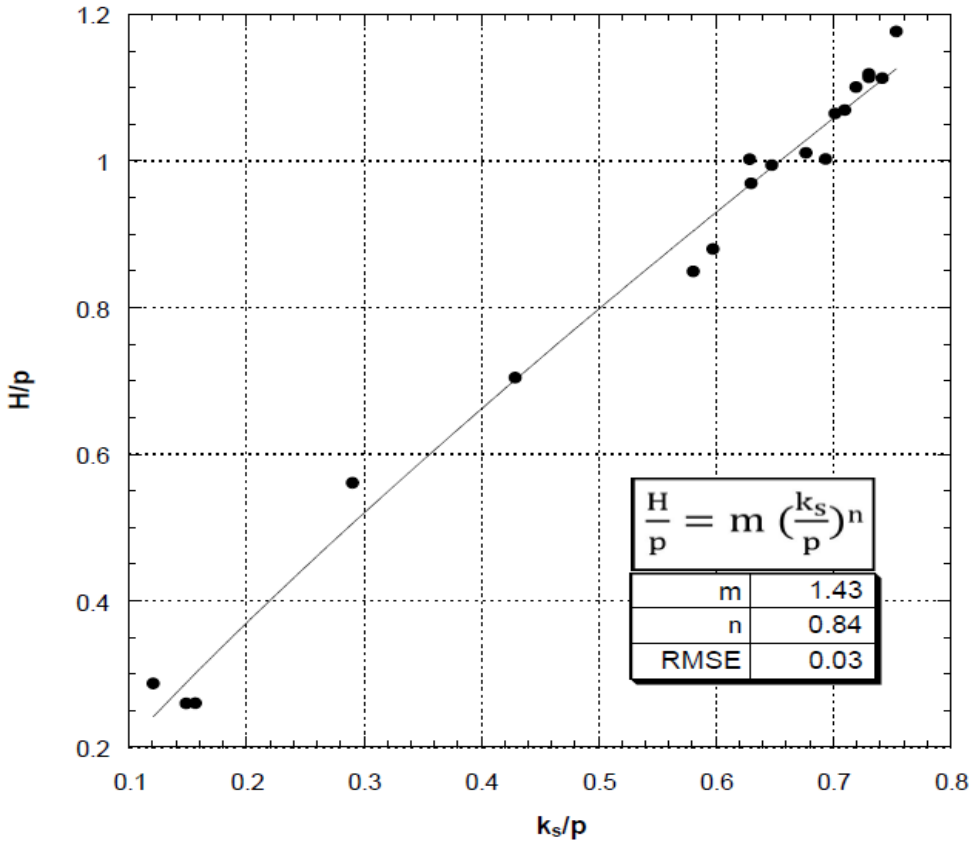

Figure 21. Coefficient and exponent of Eq. 56 for inclination angle = 29.7°

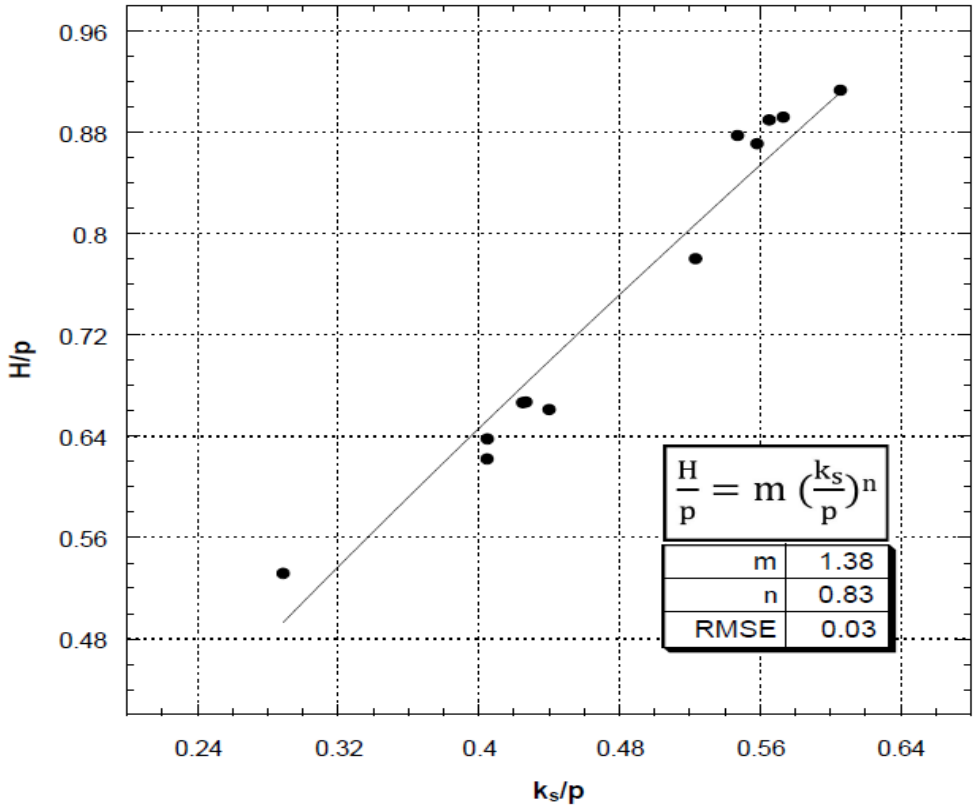

Figure 22. Coefficient and exponent of Eq. 56 for inclination angle = 32.6°

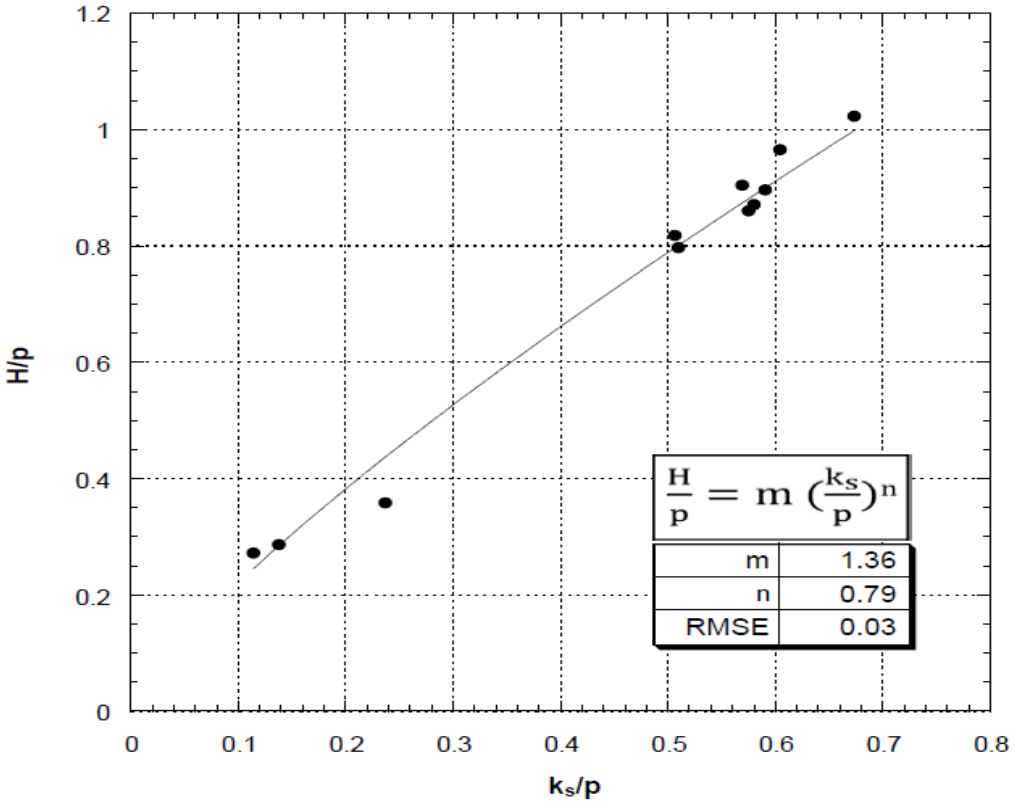

Figure 23. Coefficient and exponent of Eq. 56 for inclination angle = 34.6°

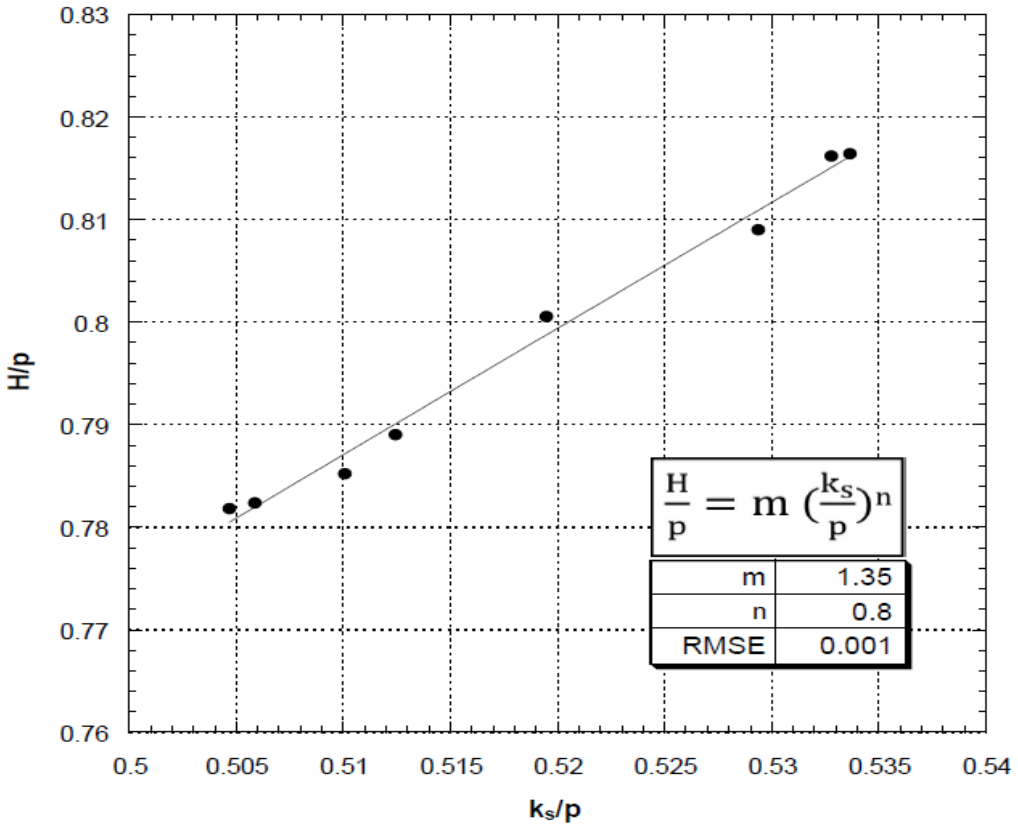

Figure 24. Coefficient and exponent of Eq. 56 for inclination angle = 35.3°

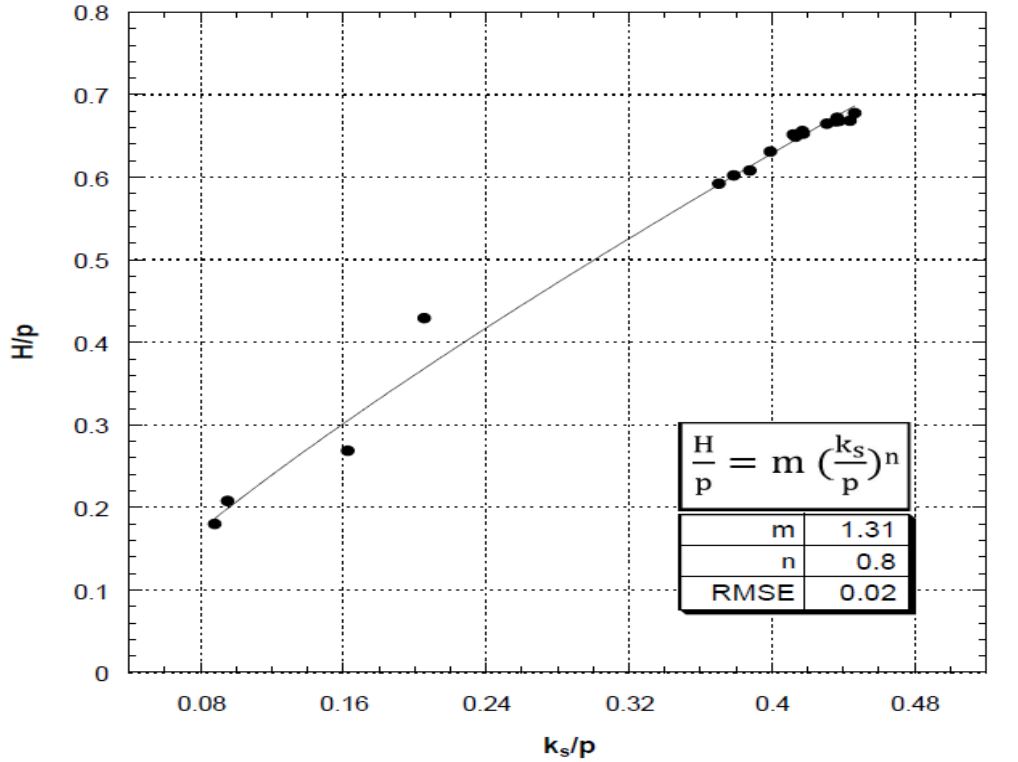

Figure 25. Coefficient and exponent of Eq. 56 for inclination angle = 38.9°

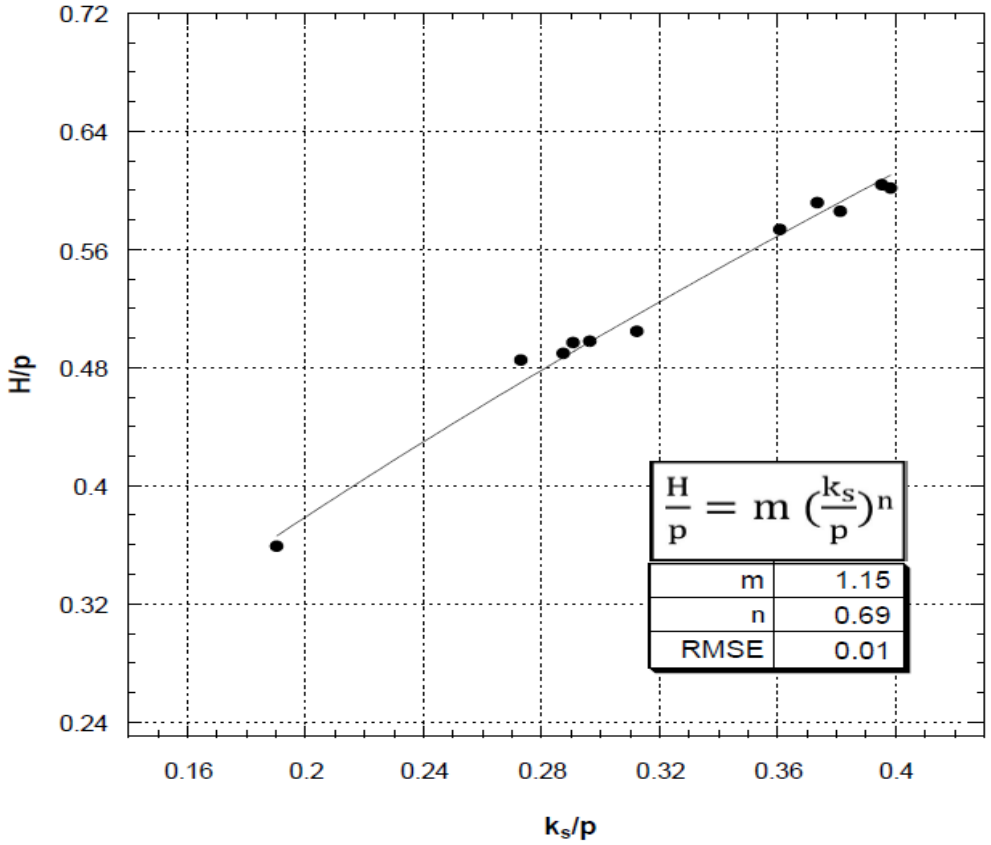

Figure 26. Coefficient and exponent of Eq. 56 for inclination angle = 40.4°

Values of *m* and *n* obtained from the curve-fitting process are summarized in Table 2.

Table 2. Coefficients and exponents of Eq. 56 for different inclination angles.

α	$\sin\alpha$	*m*	*n*
22.8	0.39	1.49	1
23.6	0.40	1.42	0.69
29.7	0.5	1.43	0.84
32.6	0.54	1.38	0.83
34.6	0.57	1.36	0.79
35.3	0.58	1.35	0.8
38.9	0.63	1.31	0.8
40.4	0.65	1.15	0.69

The relationships $m - \sin\alpha$ and $n - \sin\alpha$ were obtained using a second order polynomial curve – fitting method for the data for all of the gate flows, as described in Bijankhan and Ferro (2017), and are plotted in Figure 27 and Figure 28, respectively.

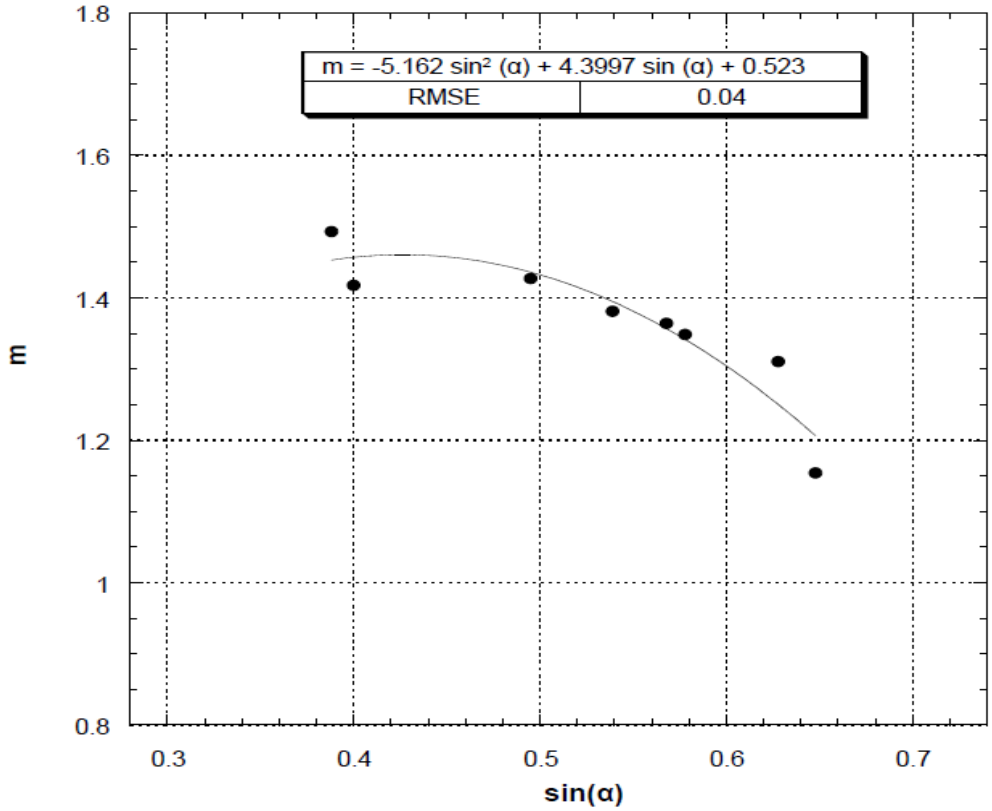

Figure 27. Data and Fitted Relationship between coefficient of Eq. 56 and inclination angle.

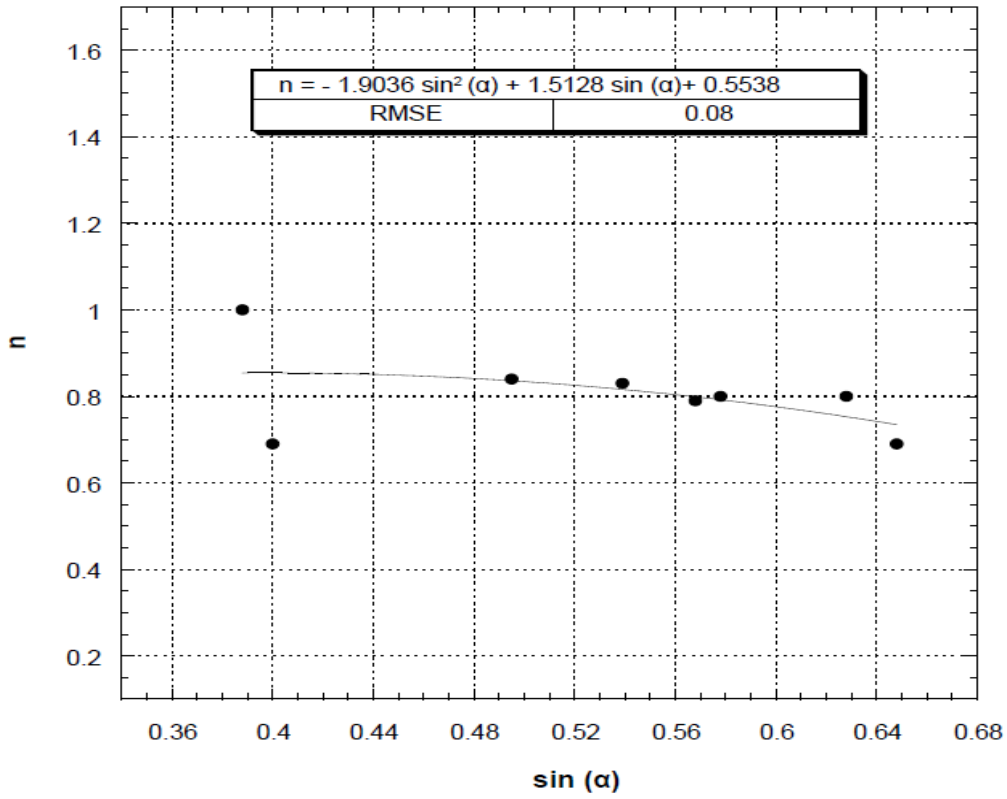

Figure 28. Data and Fitted Relationship between exponent of Eq. 56 and inclination angle.

The resulting equations were

$$m=-5.1619\sin^2(\alpha)+4.3997\sin(\alpha)+0.523 \quad (57)$$

and

$$n=-1.9036\sin^2(\alpha)+1.5128\sin(\alpha)+0.5538 \quad (58)$$

3.2.4.2 Obtaining coefficient of Eq.56 as a Function of Gate Inclination Angle by Equating Exponent of the Equation to 1

Another approach that has been employed in past studies of overshot gate flow assumes n = 1, such that Eq. 56 resembles Eq. 11 with m in Eq. 56 equivalent to t in Eqs. 10 and 11 (Bijankhan et al. 2013, Di Stefano et al. 2016, and Di Stefano et al. 2018, Bijankhan et al. 2018). Thus, the classical form of the discharge equation for sharp-crested weirs could be used to estimate the head-discharge relationship for free flow over overshot gates with a determined value of C_d. According to Aydin (et al. 2011), the value of C_d incorporates factors that are not considered in the energy conservation analysis (such as energy head loss in the approach, viscous effects, three-dimensional flow in the vicinity of the crest, side wall effects). Considering the relationship between α and Q (Prakash 2011, Nikou 2016), C_d was obtained as a function of α as well.

Since Eq. 56 takes a linear form with n= 1, linear regression was applied to the collected field data, with m calculated as the slope of the relationship between H/p and k_s/p for different values of α. By applying m to Eq. 10 and rearranging, C_d as a function of sin α was then obtained. Figure 29 to 36 depict the fitted linear relationships between H/p and k_s/p and the resulting values of m for data collected at different values of α.

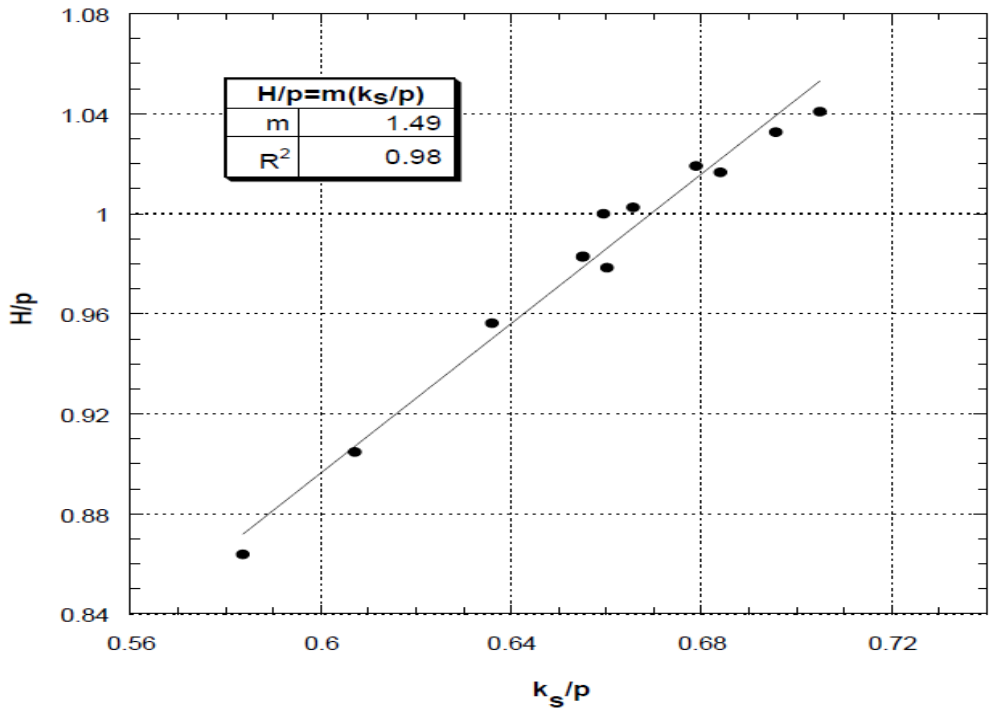

Figure 29. Coefficient of Eq. 56 from linear regression between *H/p* and k_s/p for inclination angle = 22.8°

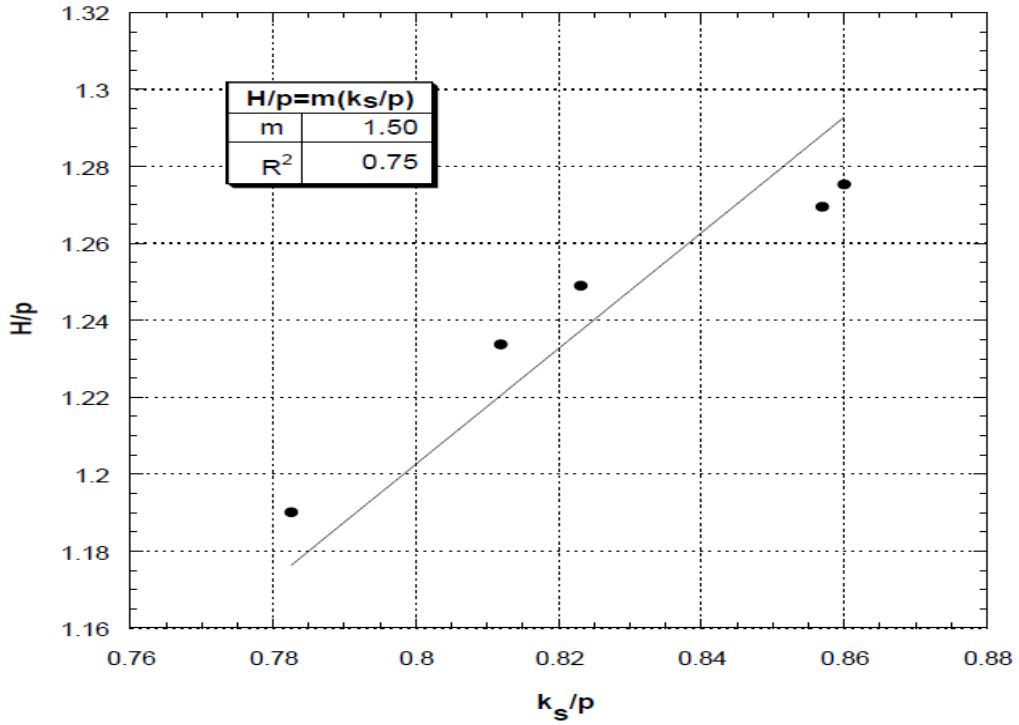

Figure 30. Coefficient of Eq. 56 from linear regression between *H/p* and k_s/p for inclination angle = 23.6°

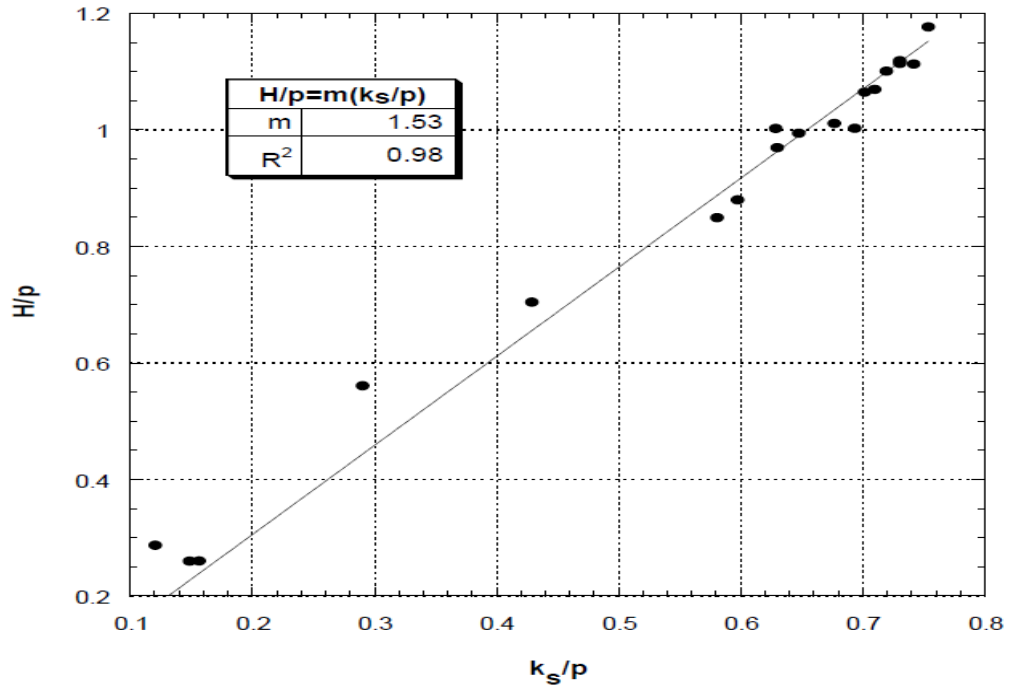

Figure 31. Coefficient of Eq. 56 from linear regression between *H/p* and k_s/p for inclination angle = 29.7°

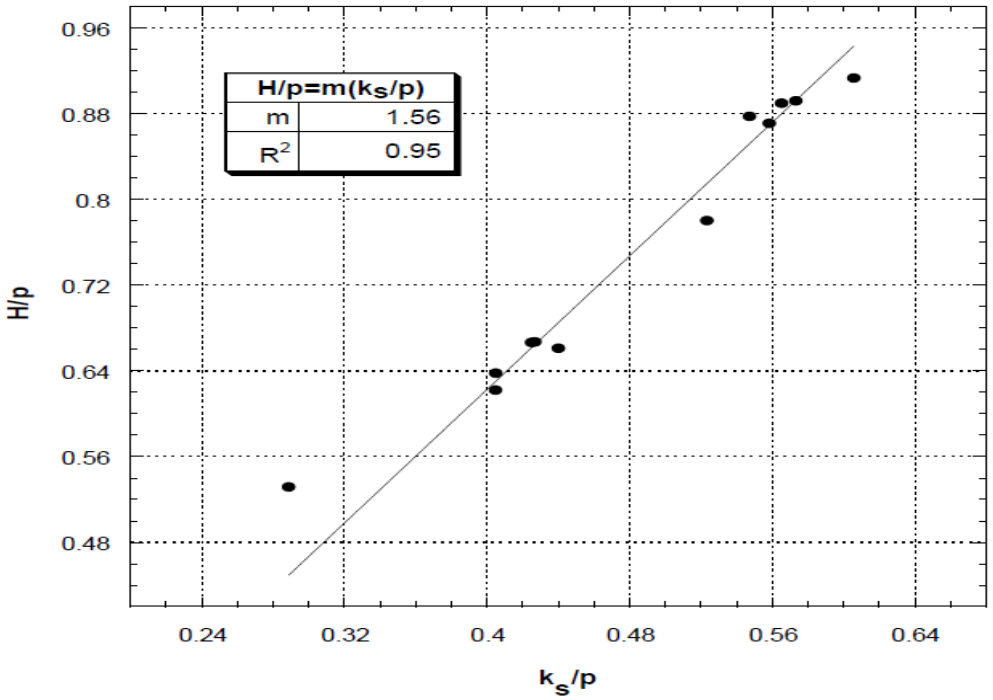

Figure 32. Coefficient of Eq. 56 from linear regression between *H/p* and k_s/p for inclination angle = 32.6°

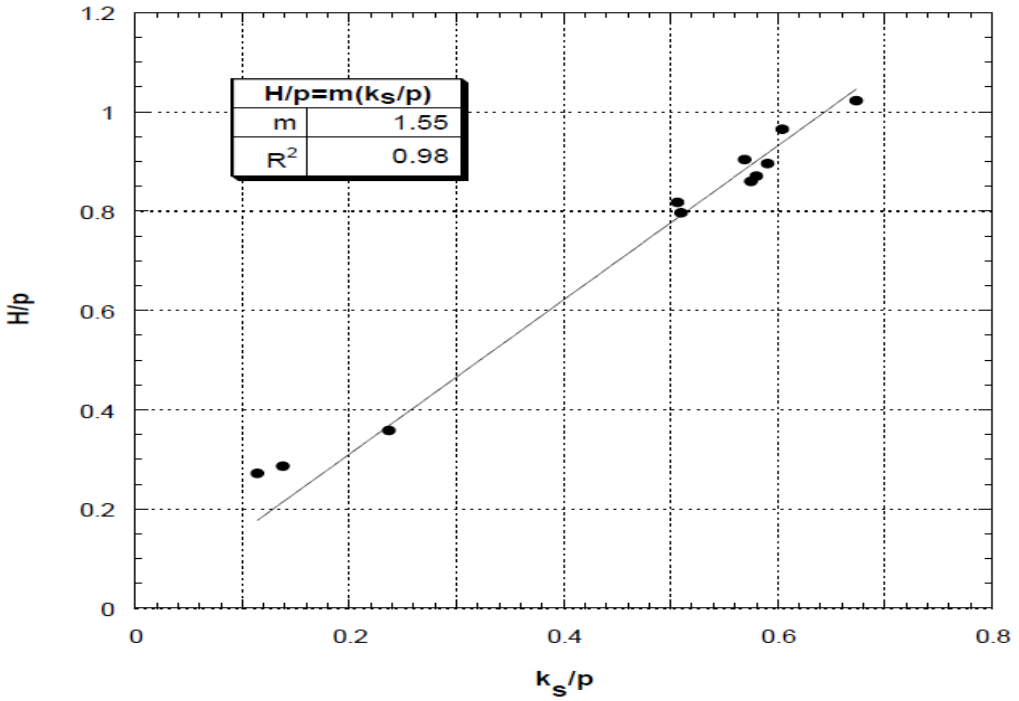

Figure 33. Coefficient of Eq. 56 from linear regression between *H*/*p* and k_s/p for inclination angle = 34.6°

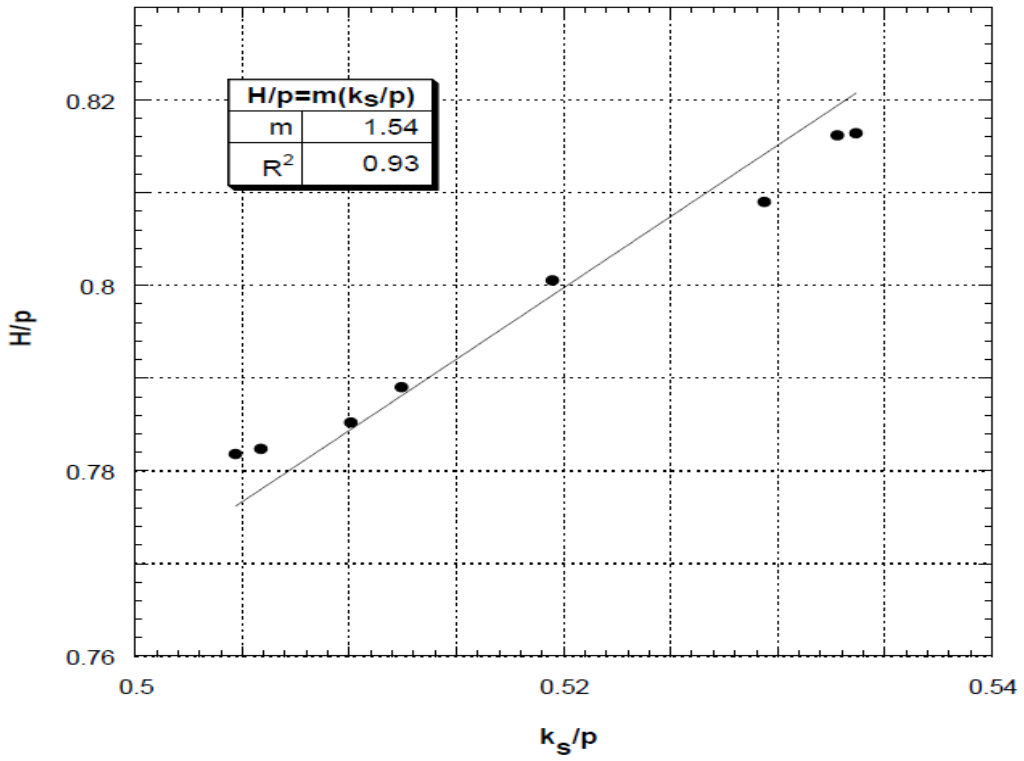

Figure 34. Coefficient of Eq. 56 from linear regression between *H*/*p* and k_s/p for inclination angle = 35.3°

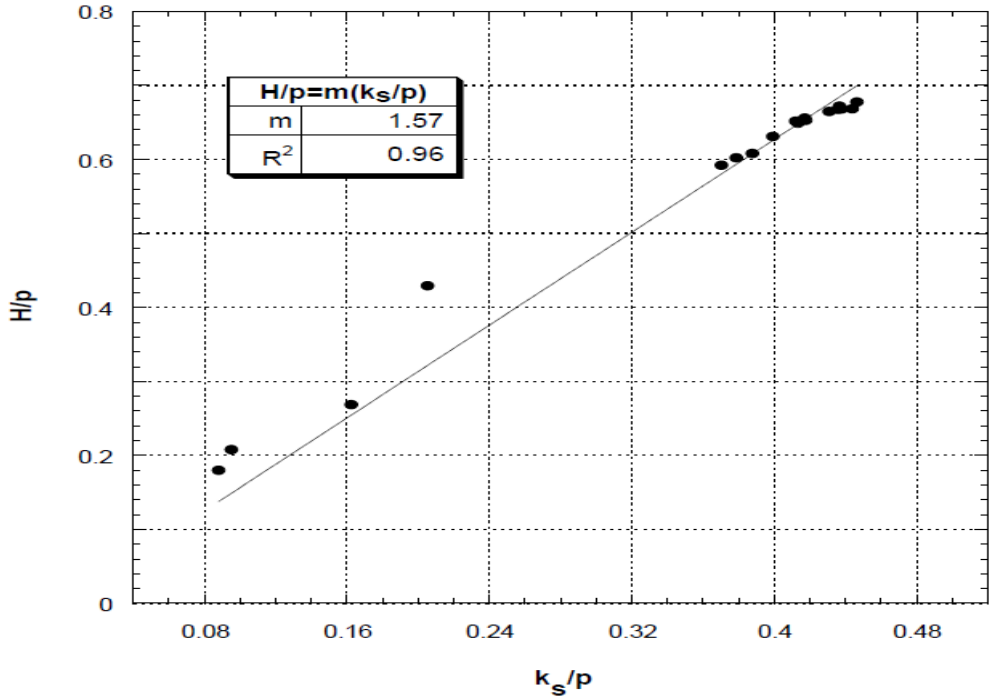

Figure 35. Coefficient of Eq. 56 from linear regression between *H/p* and k_s/p for inclination angle = 38.9°

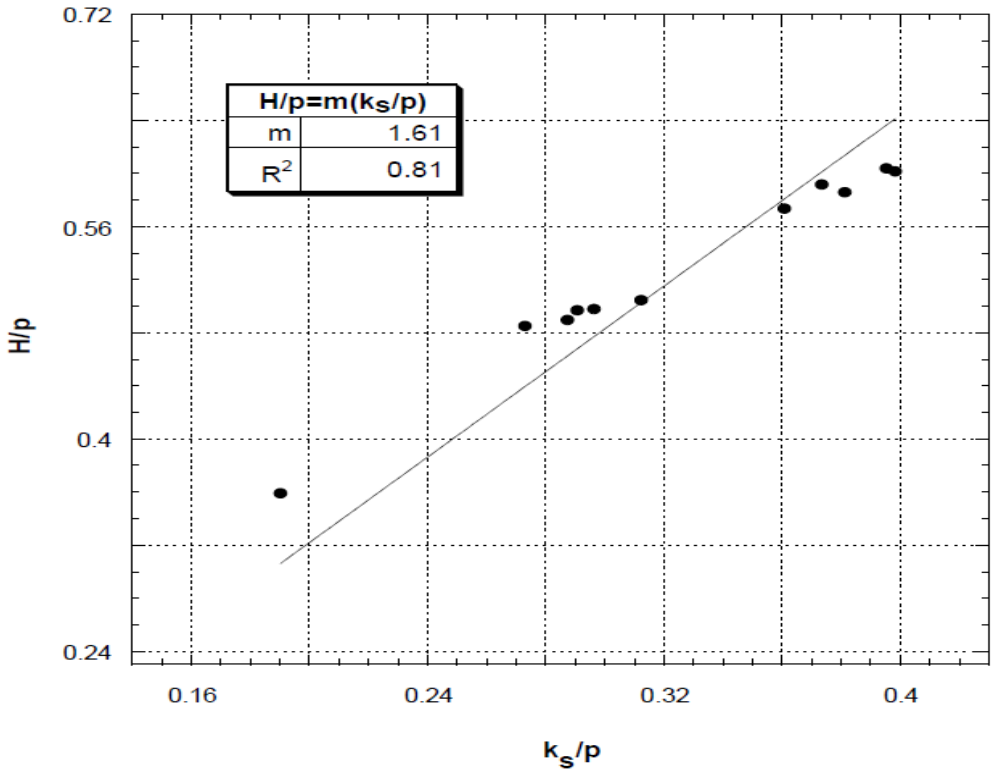

Figure 36. Coefficient of Eq. 56 from linear regression between *H/p* and k_s/p for inclination angle = 40.4°

Figures 29 to 36 depicted the values of *m* for different values of α. Equating *t* to *m* in Eq. 10, Eq. 10 was then rearranged to obtain C_d for different values of α. These C_d values were then employed in the classical sharp-crested weir head-discharge equation in order to estimate flow rate for suppressed adjustable overshot gates under free flow conditions. Rearrangement of Eq. 10 with $t = m$ gives for C_d:

$$C_d = \sqrt{\frac{9}{8m^3}} \tag{59}$$

Values of *m* and C_d for corresponding to considered values of α and sin α are summarized in Table 3.

Table 3. Values of coefficient of Eq.56 and discharge coefficient for considered values of inclination angle and sinus of inclination angle.

α (°)	sin α	*m*	C_d
22.8	0.39	1.49	0.581
23.6	0.40	1.50	0.575
29.7	0.5	1.53	0.561
32.6	0.54	1.56	0.546
34.6	0.57	1.55	0.548
35.3	0.58	1.54	0.556
38.9	0.63	1.57	0.541
40.4	0.65	1.61	0.519

A second-order polynomial equation was estimated to express the relationship between C_d and sin α, following Wahlin and Replogle (1994) and Prakash (2011) used the same form for C_d of overshot gates and inclined sharp crested weirs. Figure 37 depicts the plot of C_d versus sin α and the resulting best-fit second-order curve:

$$C_d = - 0.33112 \sin^2(\alpha) + 0.14856 \sin(\alpha) + 0.57055 \tag{60}$$

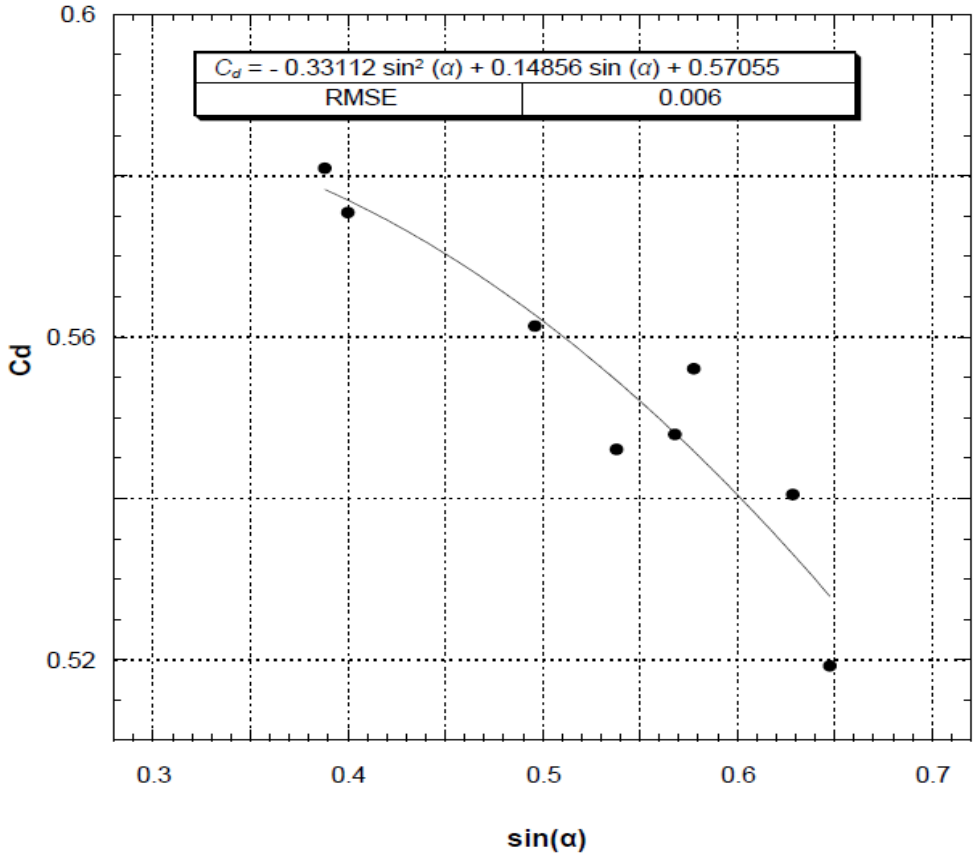

Figure 37. Discharge coefficient versus inclination angle data and fitted curve.

According to Motulsky and Ransnas (1987), R^2 is an appropriate measure of goodness of fit for linear functions only. Thus, for the nonlinear Eq. 60, the root mean square error (RMSE) and the normalized root mean square error (NRMSE) were calculated as performance measures, with goodness of fit increasing as the values of RMSE and NRMSE decrease. Values of RMSE and NRMSE for Eq. 60 were 0.006 and 0.01, respectively.

3.2.5 Obtaining a Discharge Coefficient Independent of Gate Inclination Angle

The third approach used in the literature is that of Di Stefano et al. (2018) who suggested that a single representation of C_d, irrespective of α, was possible for fully-suppressed overshot gates under free flow conditions when n = 1. To acquire C_d independent of α in this study, Eq. 56

was employed with n = 1 and treating m as a constant. Plotting all data points of H/p and k_s/p for all the gates and using linear regression (Figure 38) yielded a function with slope m = 1.52, corresponding to C_d = 0.565.

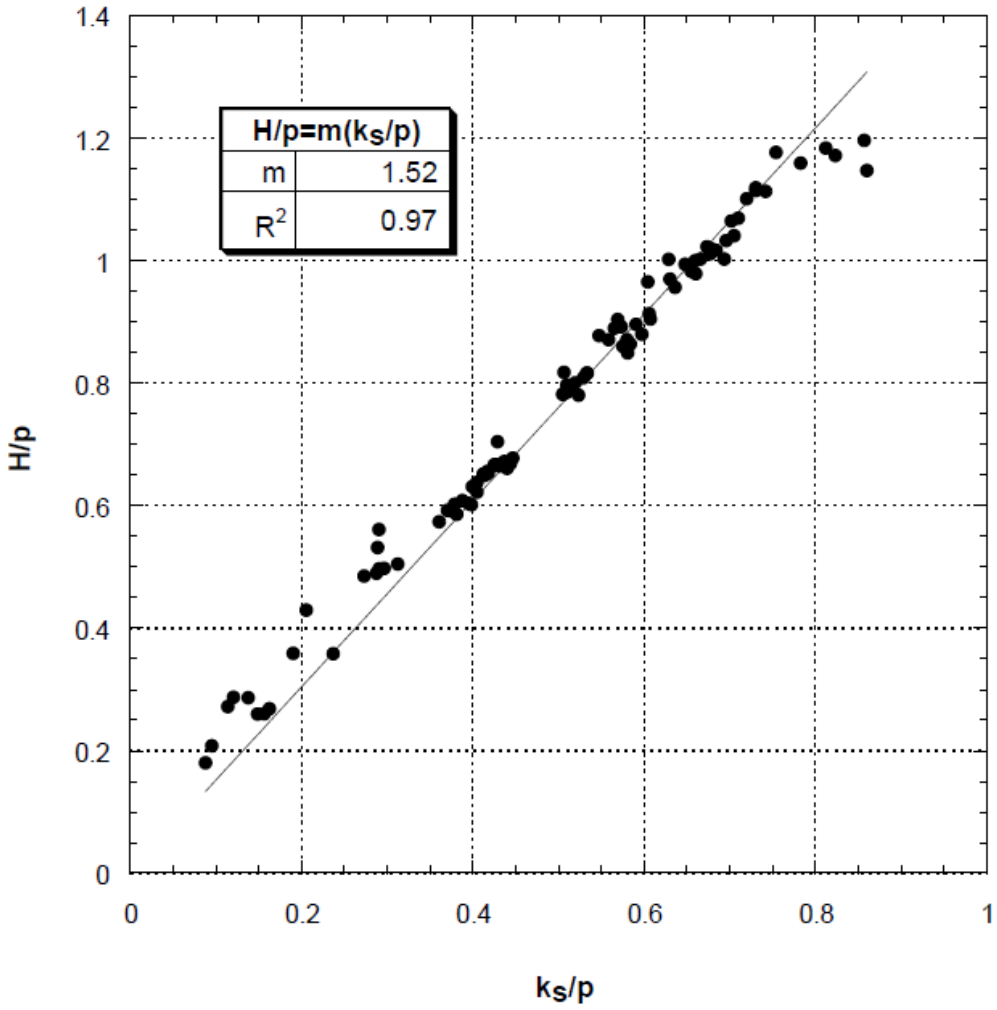

Figure 38. Coefficient of Eq.56 from linear regression between all values of H/p and k_s/p.

CHAPTER 4

RESULTS AND DISCUSSION

Using the first approach suggested in the literature, a head-discharge equation for fully-suppressed overshot gates under free flow conditions was obtained as a function of α utilizing Eq. 57 and 58:

$$Q=\sqrt{g}\, b\left[p\left(\frac{H}{p\left(-5.1619\sin^2(\alpha)+4.3997\sin(\alpha)+0.523\right)}\right)^{(1/(-1.9036\sin^2(\alpha)+1.5128\sin(\alpha)+0.5538))}\right]^{1.5} \quad (61)$$

The second approach yielded an equation in the form of the classical sharp-crested weir equation with C_d dependent upon $\sin\alpha$ using Eq. 60:

$$Q=\frac{2}{3}\left(-0.33112\sin^2(\alpha)+0.14856\sin(\alpha)+0.57055\right)\sqrt{2g}\, b\, H^{1.5} \quad (62)$$

The third approach was to employ the classical form with C_d treated as a constant, independent of α:

$$Q=\frac{2}{3}\,0.565\,\sqrt{2g}\, b\, H^{1.5} \quad (63)$$

Eq. 61, 62, and 63 are valid for $20.4 \le Q \le 330$ ft^3/s, and $22.8° \le \alpha \le 40.4°$

4.1 Uncertainty in the Discharge Equations under Free Flow Conditions

The three alternate equations were compared by comparing calculated Q values to those measured with the ADCP in the field, using RMSE and NRMSE. Table 4 shows the RMSE and NRMSE values computed for Eq. 61, Eq. 62 and Eq. 63.

Table 4. RMSE and RMSE of calculated and measured discharges for three different head-discharge equations.

	RMSE	NRMSE
Eq. 61	14.08	0.07
Eq. 62	12.56	0.06
Eq. 63	14.87	0.07

Figure 39, 40, and 41 depict the relationships between calculated and measured *Q* under free flow conditions using Eq. 61, 62, and 63, respectively, within error bounds of ±15%:

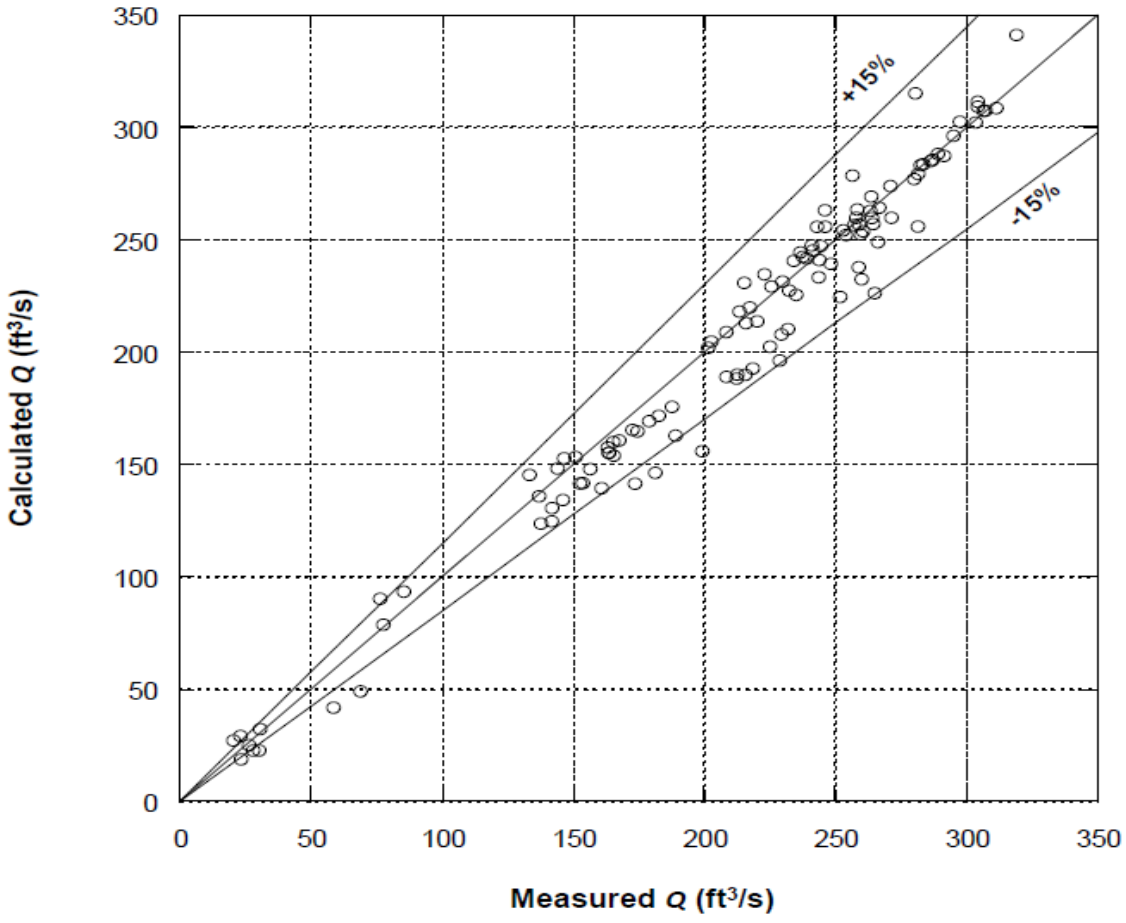

Figure 39. Calculated and measured discharges for Eq. 61

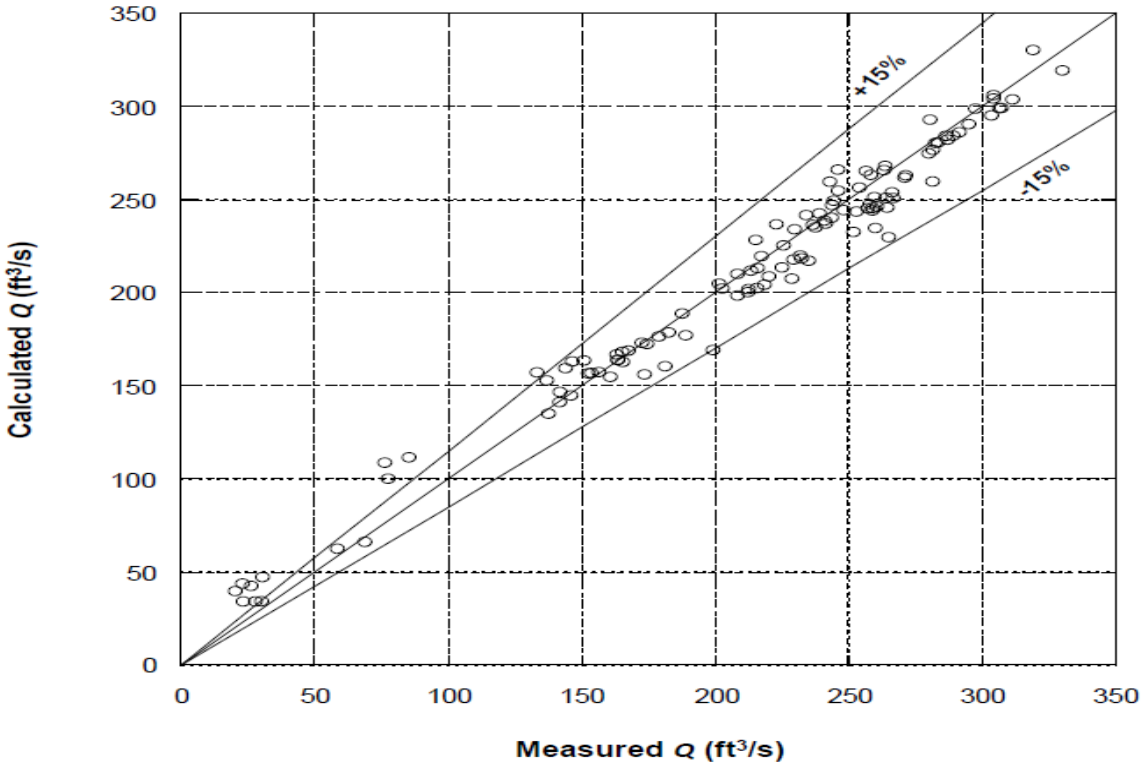

Figure 40. Calculated and measured discharges for Eq. 62

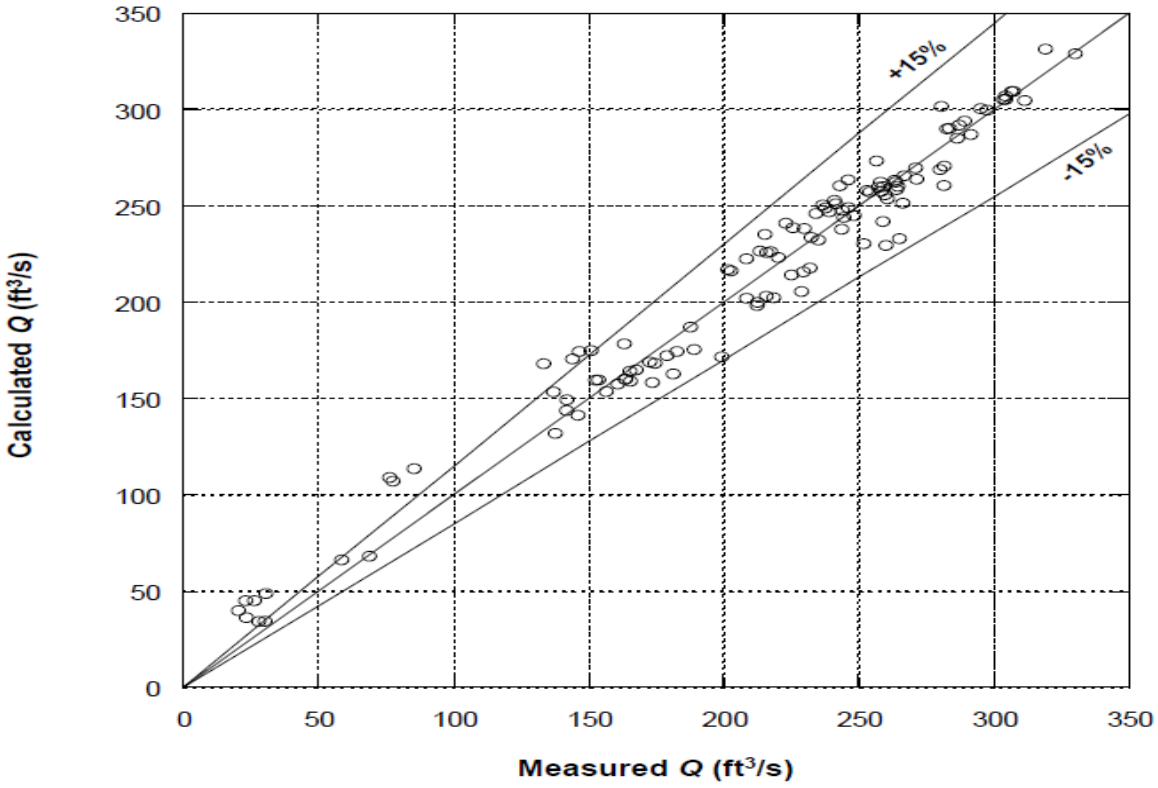

Figure 41. Calculated and measured discharges for Eq. 63

As can be seen from Table 4, Eq. 62 provides a bit more accurate results for estimation of *Q* over fully suppressed overshot gates under free flow conditions. Hence, the uncertainty in Eq. 62 was examined in detail, and the effect of α on the *Q* and the modular limits of the overshot gates were considered for Eq. 62.

The experimental field dataset of Wahlin and Replogle (1994) for Armtec overshot gates was applied using Eq. 62 to evaluate its performance under a different field condition. To examine the accuracy of Eq. 62 in detail, the relationship between calculated *Q* from Eq. 62, α of the gates, and the corresponding *H* values were depicted (Figure 43). As in Lee et al. (2014) the standard deviation of measurement error of the ADCP measurements was taken as 5%, and the measured *Q* values were depicted with 5% whisker bars in plots against *H* values for each considered α (Figure 44 to 51). Mean and standard deviation of calculated and measured *Q* values, and RMSE and NRMSE between the calculated and the measured *Q* values were obtained. NRMSE was calculated by dividing RMSE by the mean of the measured data as prescribed in Bouman and Laar (2006). In addition to RMSE and NRMSE, the absolute percent error (APE) and the mean absolute percent errors (MAPE) were calculated (Tashman 2000). Table 5 to 12 shows H, calculated and measured *Q*, and APE for each α and C_d.

Since the Gate C was not classified under submerged flow conditions (Chapter - 4, Part - 5), the measured discharge values of the gate were examined with Eq. 62 as well. Although Gate C was operated under free flow conditions during the irrigation season, measurements from the gate were not considered in Buckingham – Π analysis. The main reason for this exception was the dissimilarity of aeration conditions. Since the tail water level on Gate C reached the level of the gate crest, aeration of the water nappe that passed over the top of the gate was not comparable

to that for the other gates (Figure 42). For this reason, all data collected from Gate C was given together in Table 13 showing H, α, C_d calculated and measured Q, and APE rather than grouping for different α and C_d.

Figure 42. Flow over Gate C, indicating inadequate nappe aeration.

Table 14 summarizes mean and standard deviation of calculated and measured Q, RMSE, NRMSE, and MAPE values for α groups utilized in dimensional analysis, Gate C and pooling all the data together as well.

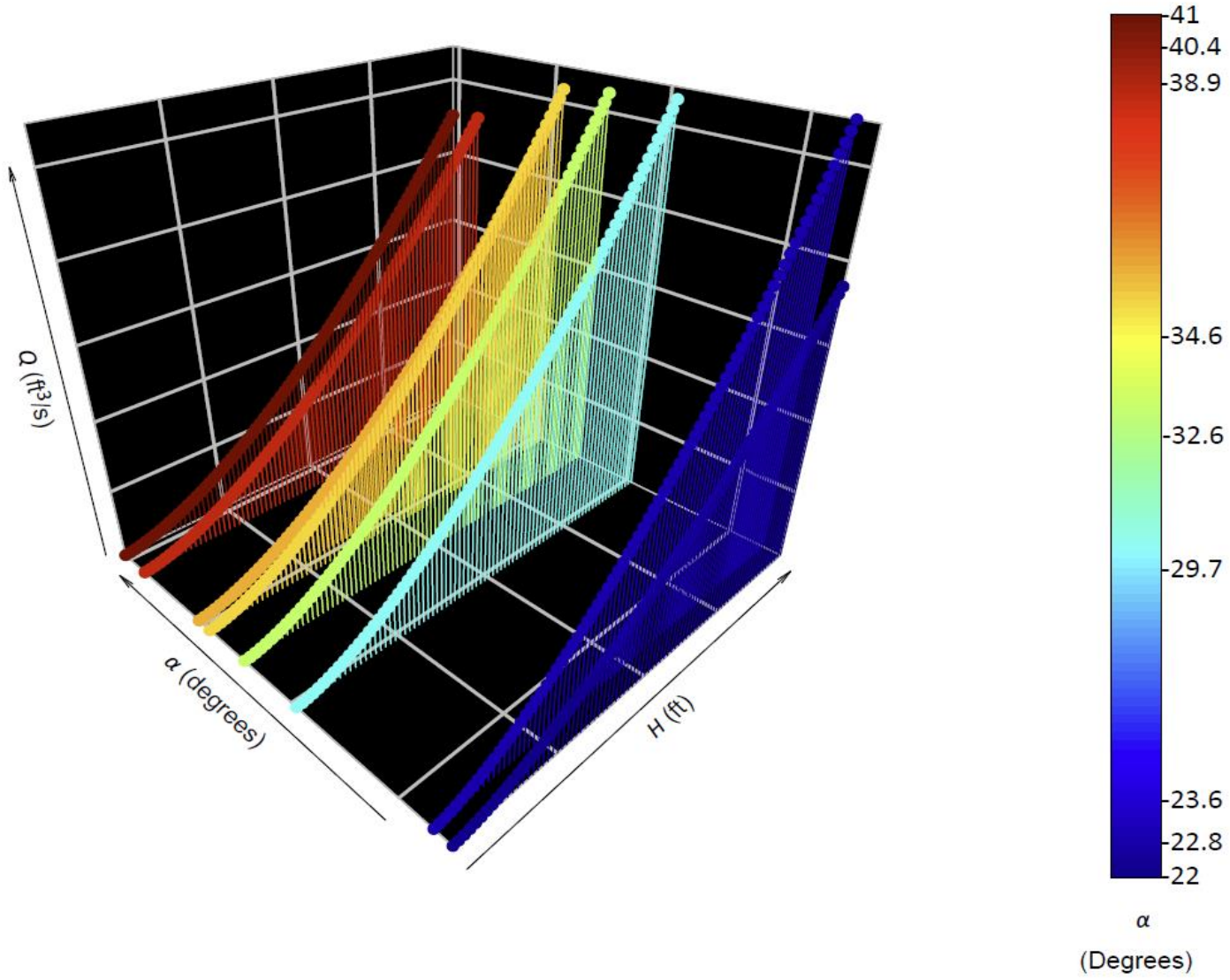

Figure 43. Discharge – Total Hydraulic Head – Inclination Angle relationship for the studied gates.

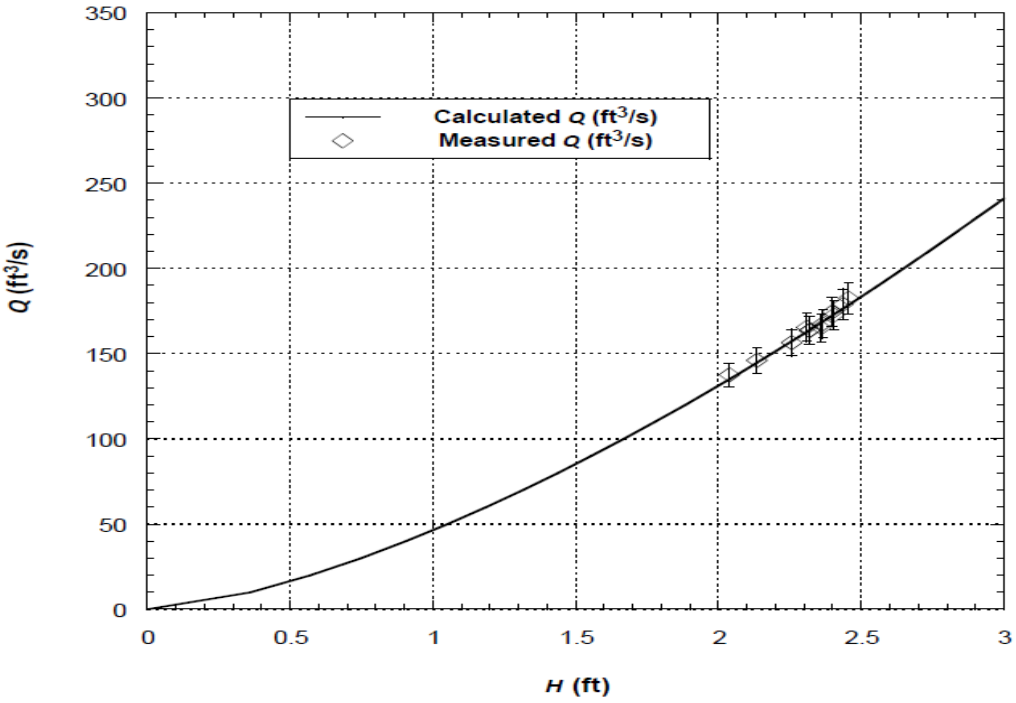

Figure 44. Calculated and measured discharges – total hydraulic head relationship for inclination angle = 22.8°, whiskers on data points indicate ± 5% of the measured value.

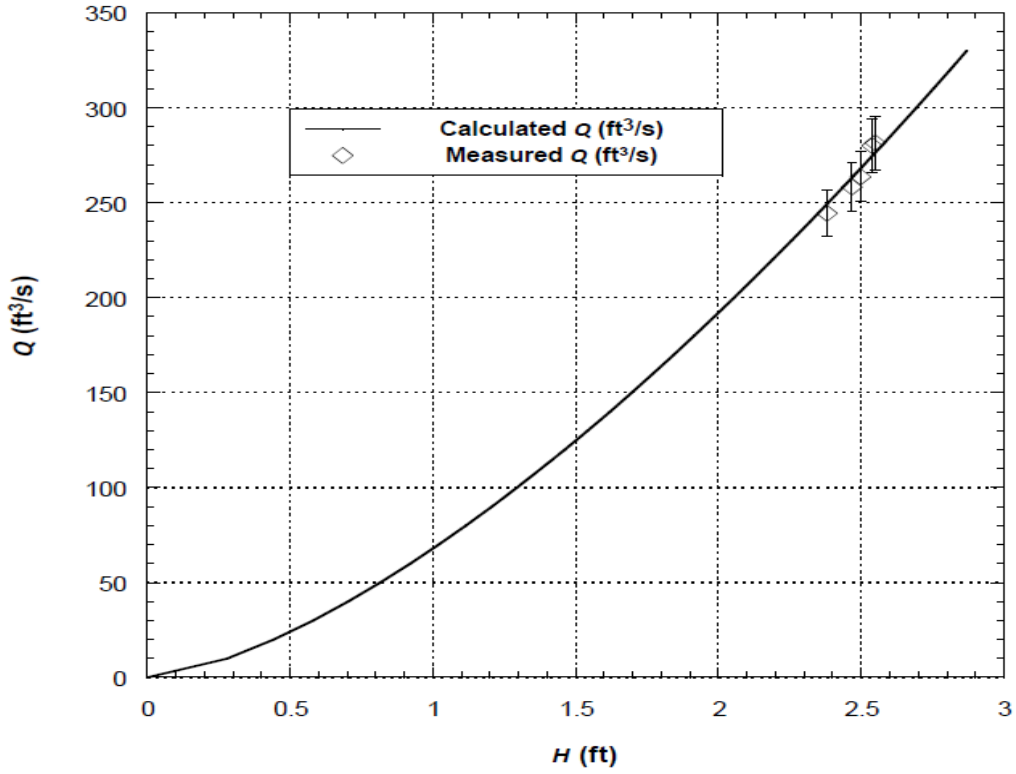

Figure 45. Calculated and measured discharges – total hydraulic head relationship for inclination angle = 23.6°, whiskers on data points indicate ± 5% of the measured value.

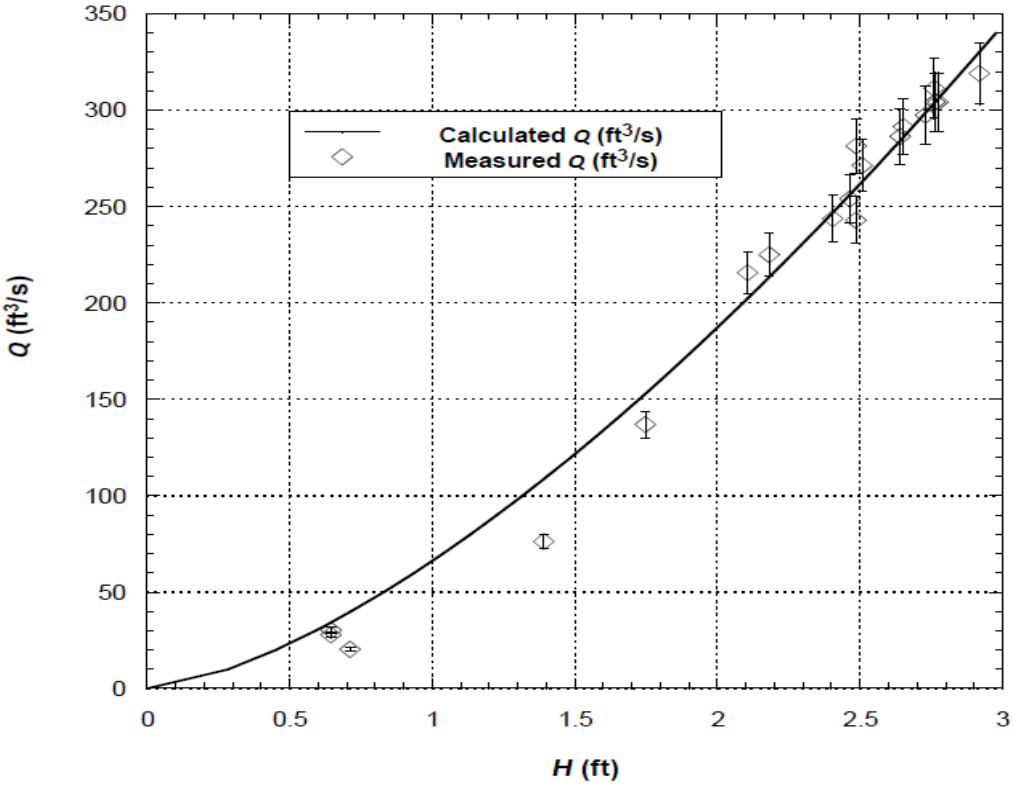

Figure 46. Calculated and measured discharges – total hydraulic head relationship for inclination angle = 29.7°, whiskers on data points indicate ± 5% of the measured value.

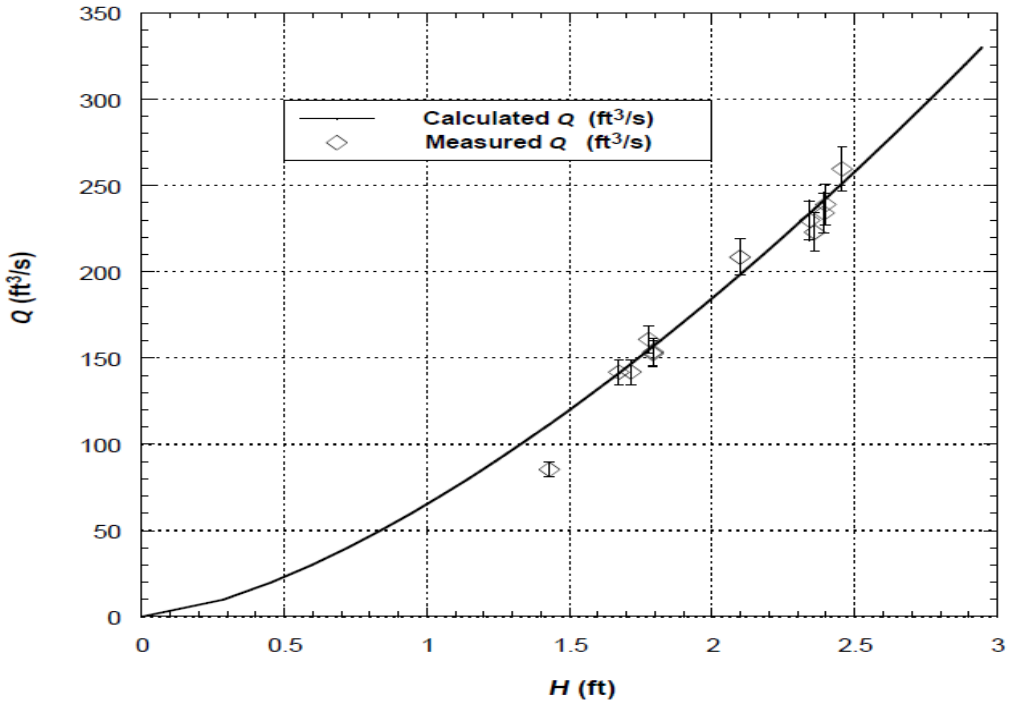

Figure 47. Calculated and measured discharges – total hydraulic head relationship for inclination angle = 32.6°, whiskers on data points indicate ± 5% of the measured value.

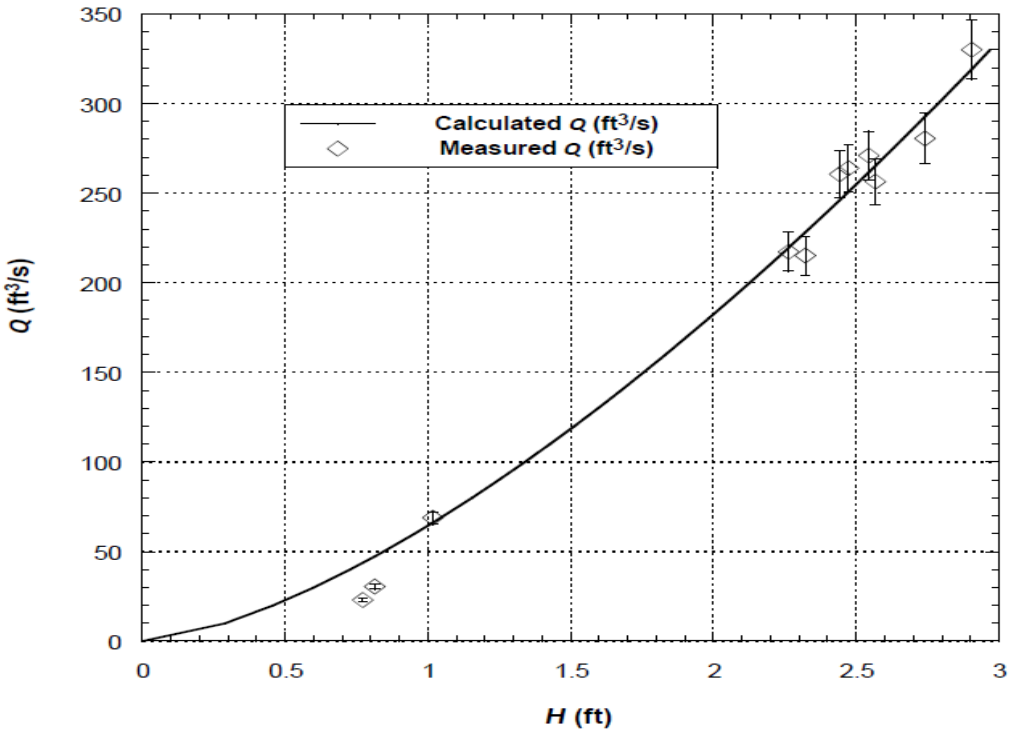

Figure 48. Calculated and measured discharges – total hydraulic head relationship for inclination angle = 34.6°, whiskers on data points indicate ± 5% of the measured value.

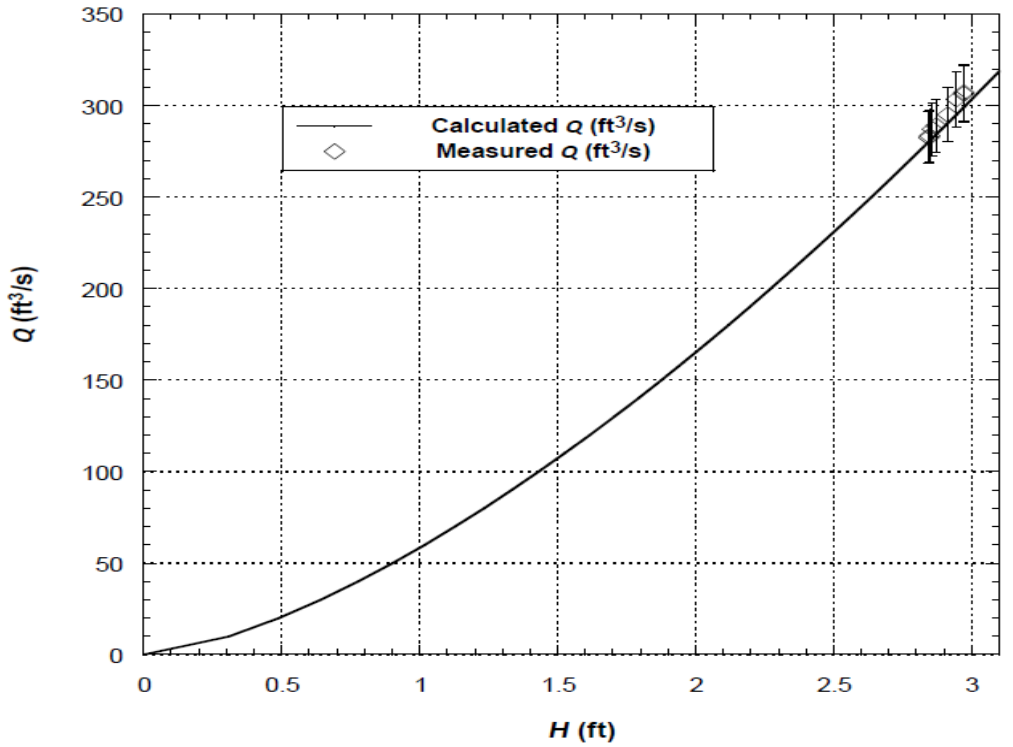

Figure 49. Calculated and measured discharges – total hydraulic head relationship for inclination angle = 35.3°, whiskers on data points indicate ± 5% of the measured value.

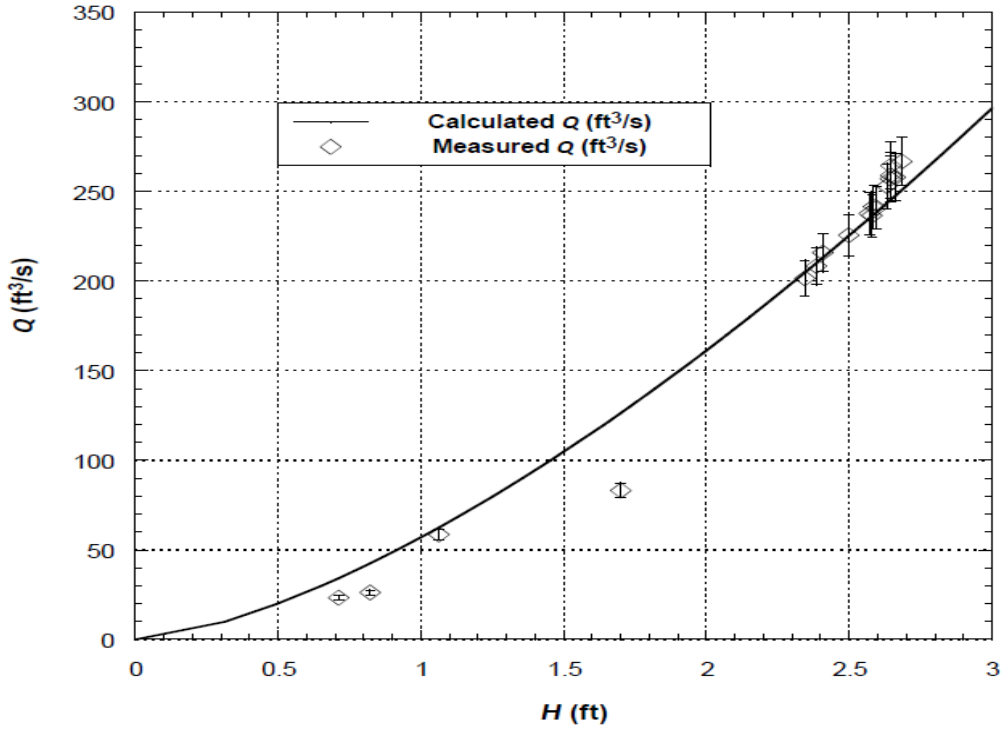

Figure 50. Calculated and measured discharges – total hydraulic head relationship for inclination angle = 38.9°, whiskers on data points indicate ± 5% of the measured value.

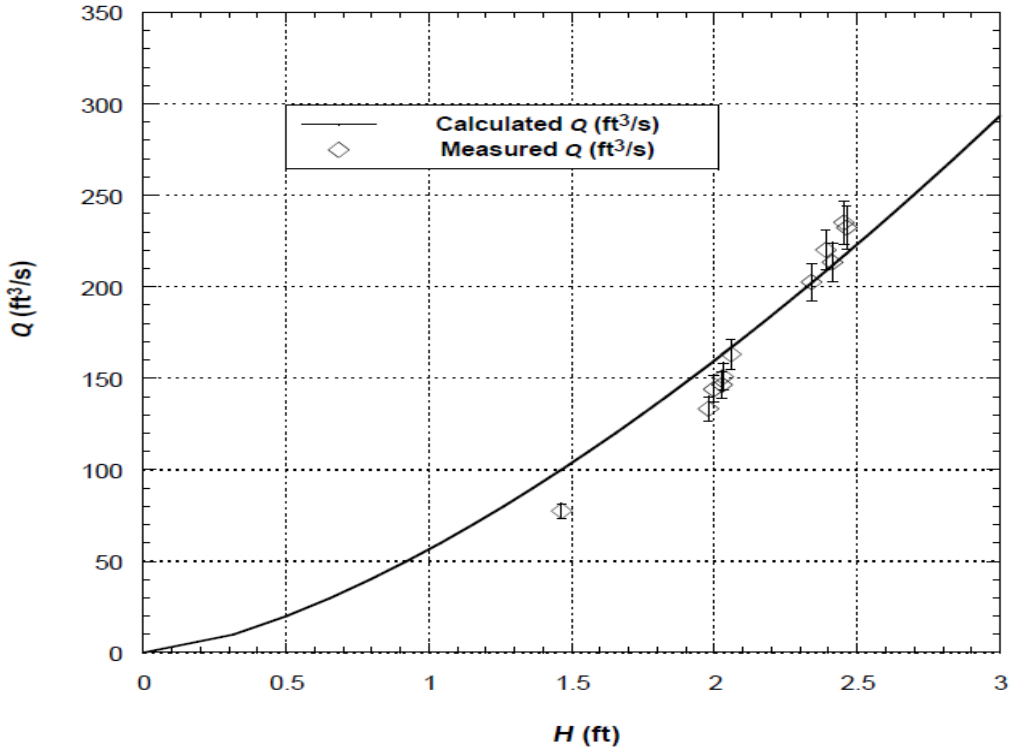

Figure 51. Calculated and measured discharges – total hydraulic head relationship for inclination angle = 40.4°, whiskers on data points indicate ± 5% of the measured value.

Table 5. Total hydraulic head, calculated and measured discharges, and absolute percentage error for inclination angle = 22.8° with discharge coefficient = 0.578.

H (ft)	Calculated *Q* (ft^3/s)	Measured *Q* (ft^3/s)	Absolute Percentage Error (%)
2.41	173	172.6	0.28
2.31	162.8	165.5	1.66
2.36	168.2	165.2	1.78
2.4	172.4	174.5	1.23
2.26	157.3	156.5	0.52
2.14	144.7	145.9	0.83
2.37	168.8	167.5	0.77
2.46	178.6	182.6	2.24
2.04	135	137.6	1.86
2.32	163.9	163.6	0.21
2.44	176.5	178.9	1.41
2.32	163.9	163.5	0.19

Table 6. Total hydraulic head, calculated and measured discharges, and absolute percentage error for inclination angle = 23.6° with discharge coefficient = 0.577.

H (ft)	Calculated *Q* (ft^3/s)	Measured *Q* (ft^3/s)	Absolute Percentage Error (%)
2.55	276.5	281.5	1.80
2.38	249.3	244.3	1.99
2.5	268	263.6	1.65
2.47	263.1	258.2	1.86
2.54	274.7	280	1.95

Table 7. Total hydraulic head, calculated and measured discharges, and absolute percentage error for inclination angle = 29.7° with discharge coefficient = 0.563.

H (ft)	Calculated *Q* (ft^3/s)	Measured *Q* (ft^3/s)	Absolute Percentage Error (%)
2.76	304.1	304.2	0.02
2.18	213.4	225.1	5.44
2.51	262.9	271.3	3.21
2.11	202.4	215.7	6.56
0.65	34.3	27.9	18.67
0.65	34.4	30.1	12.25
2.92	330.1	319	3.37
2.76	303.6	311.4	2.56
2.77	306	304.2	0.59
2.73	298.6	297.4	0.40
2.64	284.1	286.4	0.80
2.65	286	291.4	1.90
0.71	39.8	20.4	48.79
1.39	108.7	76.3	29.82
1.75	152.9	136.9	10.45
2.41	246.9	243.8	1.26
2.49	259.5	242.9	6.38
2.47	256.3	254	0.90
2.49	259.6	281.4	8.41

Table 8. Total hydraulic head, calculated and measured discharges, and absolute percentage error for inclination angle = 32.6° with discharge coefficient = 0.555.

H (ft)	Calculated *Q* (ft^3/s)	Measured *Q* (ft^3/s)	Absolute Percentage Error (%)
1.72	146.7	141.9	3.30
1.67	141.2	141.8	0.38
1.78	154.7	160.7	3.87
1.79	156.8	153.6	2.07
1.79	156.7	152.6	2.61
2.39	241.6	234.1	3.13
2.46	251.2	259.6	3.34
2.36	236.6	222.9	5.80
1.43	111.6	85.4	23.48
2.1	198.4	208.5	5.08
2.34	234	229.7	1.83
2.4	242.5	239	1.45

Table 9. Total hydraulic head, calculated and measured discharges, and absolute percentage error for inclination angle = 34.6° with discharge coefficient = 0.548.

H (ft)	Calculated *Q* (ft^3/s)	Measured *Q* (ft^3/s)	Absolute Percentage Error (%)
2.74	292.7	280.5	4.19
2.57	265.3	256.5	3.32
2.32	228.2	215.2	5.71
2.26	219.6	217.3	1.02
2.9	319.2	330	3.38
1.02	66.2	68.9	4.05
0.81	47.4	30.5	35.50
0.77	43.8	23	47.51
2.47	250.8	263.8	5.19
2.54	261.7	271	3.55
2.44	246.2	260.5	5.81

Table 10. Total hydraulic head, calculated and measured discharges, and absolute percentage error for inclination angle = 35.3° with discharge coefficient = 0.546.

H (ft)	Calculated *Q* (ft^3/s)	Measured *Q* (ft^3/s)	Absolute Percentage Error (%)
2.95	295.1	303.5	2.85
2.97	299.1	307.3	2.69
2.97	299	306.4	2.48
2.86	282.1	287	1.74
2.87	284.2	289	1.70
2.91	290.4	295	1.57
2.85	280.6	283.5	1.03
2.85	280.3	282.5	0.78

Table 11. Total hydraulic head, calculated and measured discharges, and absolute percentage error for inclination angle = 38.9° with discharge coefficient = 0.533.

H (ft)	Calculated *Q* (ft^3/s)	Measured *Q* (ft^3/s)	Absolute Percentage Error (%)
2.41	213.1	215.8	1.27
2.5	225.2	225.5	0.14
2.65	245.6	264.3	7.64
2.68	250.7	266.7	6.36
2.63	243.5	252.9	3.86
2.4	210.1	208.3	0.82
2.35	204.8	201.5	1.61
1.06	62.6	58.6	6.41
0.82	42.6	26.2	38.39
0.71	34.3	23.32	32.01
1.7	126.4	83.2	34.19
2.6	238.6	240.9	0.96
2.58	236.4	236.5	0.06
2.64	245.2	257.1	4.88
2.65	245.4	259	5.51
2.66	247.5	257.9	4.21
2.57	235	237.6	1.11
2.59	237.1	241.4	1.83

Table 12. Total hydraulic head, calculated and measured discharges, and absolute percentage error for inclination angle = 40.4° with discharge coefficient = 0.528.

H (ft)	Calculated *Q* (ft^3/s)	Measured *Q* (ft^3/s)	Absolute Percentage Error (%)
2.03	163.1	146.5	10.14
1.98	157.2	133.3	15.17
2.45	217.1	235.1	8.28
2.06	166.8	163.2	2.17
2.03	163.5	150.8	7.74
2	159.4	144	9.68
2.41	211.8	213.4	0.76
1.47	100.1	77.6	22.55
2.34	202.1	202.6	0.23
2.39	208.6	220.1	5.50
2.46	218.4	232.4	6.41

Table 13. Inclination angle, discharge coefficient, total hydraulic head, calculated and measured discharges, and absolute percentage error for Gate C

α (Degrees)	C_d	H (ft)	Calculated Q (ft^3/s)	Measured Q (ft^3/s)	Absolut Percent Error (%)
26.9	0.570	2.62	219.9	231.8	5.45
26.9	0.570	2.6	217.8	229.4	5.32
26.9	0.570	2.37	188.8	187.7	0.60
26.9	0.570	2.27	177.1	189	6.70
26.9	0.570	2.48	201.8	212.5	5.28
26.9	0.570	2.46	200.2	212.3	6.05
26.9	0.570	2.52	207.5	228.8	10.25
26.9	0.570	2.5	204.2	218.4	6.96
31.8	0.557	2.24	169.2	199.2	17.73
31.8	0.557	2.16	160.5	181.2	12.92
31.8	0.557	2.12	156.1	173.5	11.17
26.9	0.570	2.98	266	245.9	7.53
31.8	0.557	2.74	229.7	264.9	15.32
29.6	0.563	2.83	244.3	248.2	1.58
26.9	0.570	2.97	265.7	263.2	0.95
23.4	0.577	2.71	234.7	260	10.81
26.9	0.570	2.88	253.8	266.1	4.89
23.4	0.577	2.87	254.7	246	3.39
26.9	0.570	2.81	244.1	258.9	6.04
26.9	0.570	2.78	240.1	243.6	1.45
26.9	0.570	2.72	232.5	251.7	8.27

Table 14. Statistics of the errors between measured and calculated discharges for the considered values of inclination angle.

α	# of Data Points	RMSE	NRMSE	MAPE (%)	Mean Measured Q (ft^3/s)	Std. Dev. of Measured Q	Mean of Calculated Q (ft^3/s)	Std. Dev. of Calc.Q
22.8	12	2.11	0.01	1.08	164.5	13	163.7	12.9
23.6	5	4.93	0.02	1.85	265.5	15.6	266.3	10.9
29.7	19	12.8	0.06	8.51	217.9	104.6	220.2	98.3
32.6	12	10.09	0.05	4.69	185.8	53.2	189.3	49.7
34.6	11	12.44	0.06	10.84	201.6	108.2	203.7	101.1
35.3	8	5.83	0.02	1.86	294.2	10.2	288.8	8.1
38.9	18	13.85	0.07	8.40	197.6	85.3	196.9	75
40.4	11	14.82	0.09	8.06	174.4	49.9	178.9	36.3
Gate C	21	17.04	0.07	7.08	229.2	29.7	217.6	33.6
Entire Data	117	12.56	0.06	6.52	209.7	74.6	208.4	68.9

RMSE values comparing calculated to measured *Q* were calculated as 2.11 - 17.04, while NRMSE values were calculated 0.01 - 0.09. MAPE were calculated as 1.1% - 10.8%. The equation was evaluated pooling all the data together and the resulting RMSE was calculated as 12.56, NRMSE was 0.06, and MAPE was 6.52%.

To describe the uncertainty in Eq. 62, values of percent residual, ε_Q, were calculated by subtracting the measured *Q* from the calculated *Q* then dividing by the measured discharge and multiplying by 100 to obtain percent. The probability distribution of the percent residuals was fit to a log-logistic form for using Anderson-Darling, Chi-square, Kolmogorov-Smirnov, and Akaike Information Criterion goodness of fit statistics (Ashkar and Mahdi, 2006). The location parameter, shape parameter and scale parameter were obtained as -16.87, 16.12, 3.78, respectively utilizing @RISK software (Version 7.6, Palisade). The mean of the fitted distribution was 1.27% with a standard deviation of 10.24%. About 86.2% of the data residuals were within of ±10% of the mean value. Thus, accounting for uncertainty, Eq. 62 can be expressed in the following form:

$$Q=\left(\frac{2}{3}\left(-0.331\sin^2(\alpha)+0.149\sin(\alpha)+0.571\right)\sqrt{2g}\,b\,H^{1.5}\right)\left(1+\frac{\varepsilon_Q}{100}\right) \quad (64)$$

Figure 52 shows the error distribution of the data with the line of equity for both ±10% and ±15 % error ranges. Also in Figure 52, 5% error bars were used on the data points to illustrate ADCP flow measurement error (Gordon 1989, Morlock 1996, Lee et al. 2014), with 10% error bars employed for cases where $\bar{u} < 0.8$ ft/s, as Lee et al. (2014) and Mueller et al. (2013) underlined that the uncertainty is greater when the flow velocity decreases below 0.82 ft/s. These error bars are indicative of the uncertainty associated with the measured values themselves.

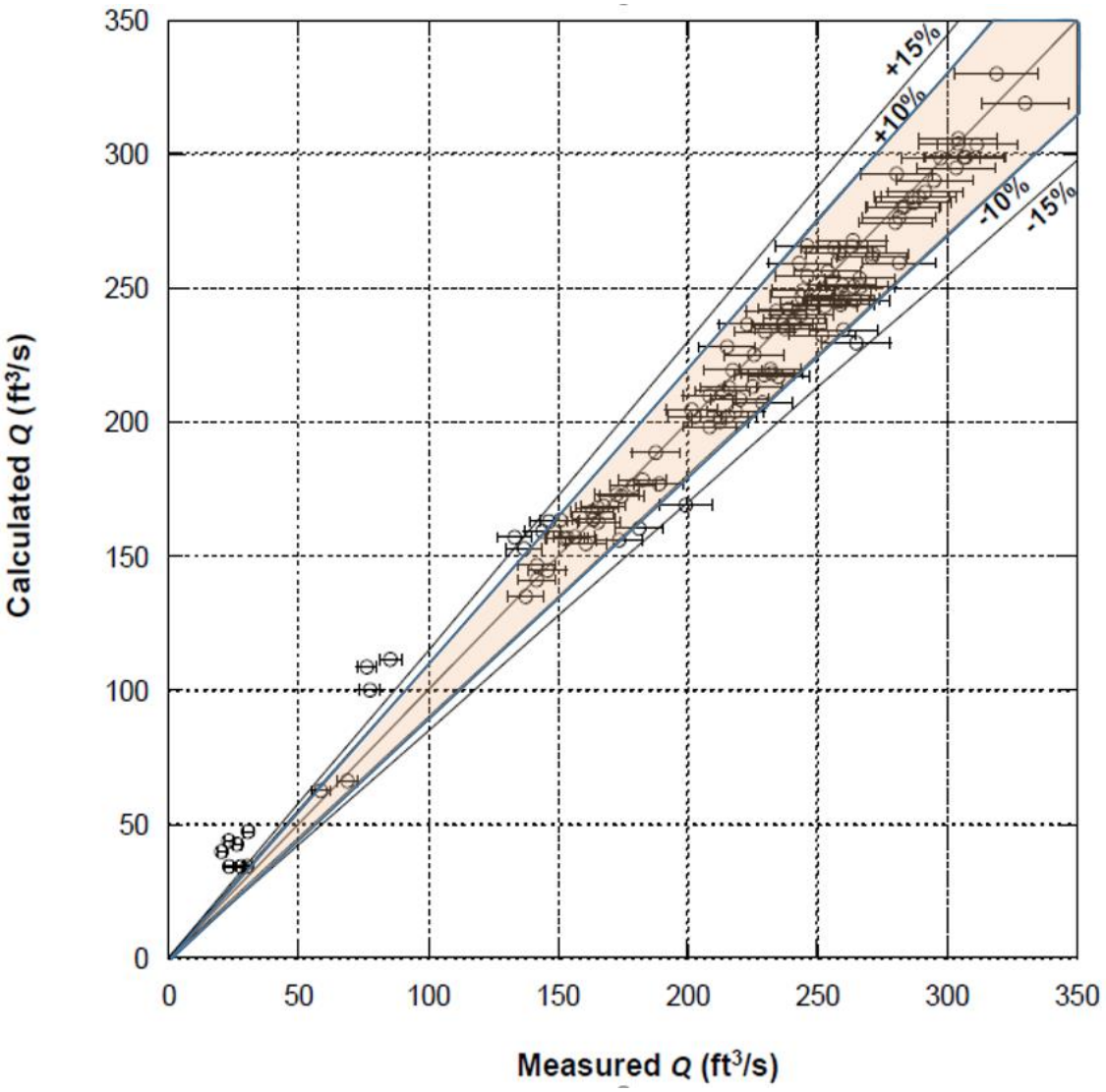

Figure 52. Calculated and Measured discharges, showing calculated and measured error ranges.

As can be seen from Figure 52, a larger discrepancy between calculated and measured values can be seen for 76.3 $ft^3/s \leq Q \leq 85.4\ ft^3/s$. This discrepancy may be explained by the substantial transition of flow conditions that occurred during the measurements. At the time that these measurements were taken, the flow regime altered abruptly, likely due to adjustments in regulating and diversion structures upstream. Additionally, a relatively low coherence between

calculated and measured Q is seen for $Q < 50$ ft^3/s. A maximum $\bar{u}$ of 0.41 ft/s was recorded for this condition. According to Muller et al. (2013), at a flow velocity of less than 0.5 ft/s, the boat control becomes difficult and is interrupted by external effects. Lee et al. (2014) described the impracticability of using ADCPs for flow velocity values lower than 0.82 ft/s, leading to large variability in computed transect Q values. The researchers also found that the non-uniformity of the density of suspended particles that scatter the acoustic waves and debris accumulation near the channel bed and banks were sources of Q measurement deviation. Aydin et al. (2011) observed considerable channel bed effects when y was low. According to the WinRiver II Software User's Guide (2016), the bottom tracking mode of the ADCP can deviate due to the acoustic absorption and the scattering density in the canal. Hence, the negative effects on boat control and the physical conditions of the canal under low flow conditions may contribute to greater errors in the measured Q values lower than 50 ft^3/s (Figure 53). Furthermore, Gordon (1989) indicated that unmeasured areas in the cross section contribute to a substantial portion of the error margins for ADCP measurements. Considering lower flow conditions, the ratio of the unmeasured zones to the measured zones would be greater than those under higher flow conditions thereby contributing to the larger discrepancy between calculated and measured values for $Q < 50$ ft^3/s.

Figure 53. Sediment Load and Debris Accumulation under the low flow effect in the canal

4.2 Testing the Head-Discharge Equation (Eq.62) with a Different Data Set

The performance of the best-fit head-discharge equation (Eq. 62) was examined in application to field data published in Wahlin and Replogle (1994). The flow measurement field data was collected from Armtec Gates located in IID canals.

In the Wahlin and Replogle (1994) study, the Armtec gates in the Plum and Oasis Canals had an average surface area of 28.5 ft^2 (the length of the gate leaves in Plum and Oasis Canals were 5.08 ft and 5.58 ft, respectively and the width of the gate leaves were 5.35 ft for both). The Armtec gates were flat, made of stainless steel. The gate leaves had weighty seal effects

(supplement material mounted at side of the gates) and the crest of the leaves were not perfectly sharp, so that additional errors in the flow measurements were considered. Level problem between the two sides of the gate crests for flow measurements also was noted by Wahlin and Replogle (1994). *Q* was measured by a broad-crested weir at a distance of about 400 ft downstream of the Armtec Gates. The value of *h* upstream of each gate was measured by point gages with moveable stilling wells. The canals in the IID field study were concrete-lined and trapezoidal with a bottom width of 2 ft for both. The side slope of the Plum Canal was 1.5, whereas it was 1.25 for the Oasis Canal. For the Obermeyer-type gates examined in the present study, the average surface area of the gate leaves that the flow passed over was 106.45 ft^2. The Obermeyer gates have a slight curvature through the end of the gate leaf. The Obermeyer gate leaves were quite thin and were equipped with stiffness plates, which helped straighten the streamlines. The surface area of the gate leaves was covered by heavy rusty layers as well. The canal in which the Obermeyer gates were located, was earthen (the canal bed consisted of clay and the banks were covered by dense vegetation) except for the side walls adjacent to the gates.

Table 15 displays, α, *H* (since only *h* was presented in Wahlin and Replogle (1994) observations, the total energy head *H* was calculated using the description of the Plum and Oasis Canal geometries in Wahlin and Replogle (1994), assuming $\Lambda = 1.1$), *Q* measured and reported by Wahlin and Replogle (1994) for flow over the Armtec gates in the Plum and Oasis Canals of the IID along with the corresponding C_d value in Eq. 62 and *Q* calculated by Eq. 62. Also shown is the percent error [(calculated *Q* - measured *Q*) 100/ measured *Q*] associated with the use of Eq. 62 to calculate *Q*. RMSE and NRMSE values between the Q calculated by Eq. 62 and the *Q* measured by Wahlin and Replogle (1994) were calculated as 4.56 and 0.24, respectively. MAPE was

calculated as -22% with a standard deviation of 3%. Wahlin and Replogle (1994) reported that the residual error in the calculation of *Q* with their head-discharge equation in comparison to the IID data was about -9.6% (standard deviation).

Table 15. Measured inclination angle, total hydraulic head, and discharge for Armtec Overshot Gates in IID Canals Reported by Wahlin and Replogle (1994); calculated discharge coefficient and discharge from Eq. 62; and Absolute Percent Difference.

Measured α (Degrees)	Measured *H* (ft)	Measured *Q* (ft^3/s)	C_d in Eq. 62	Calculated *Q* from Eq. 62 (ft^3/s)	Percent Error (%)
40.3	0.60	9.41	0.528	6.97	-0.26
39.1	0.57	8.7	0.533	6.64	-0.24
37.5	0.54	8.2	0.538	6.12	-0.25
37	0.56	8.48	0.540	6.47	-0.24
33.2	0.61	9.16	0.553	7.62	-0.17
28.8	0.62	9.71	0.565	7.84	-0.19
25.3	0.62	9.26	0.574	7.94	-0.14
33.4	1.30	29.27	0.552	23.39	-0.20
31	1.31	30.43	0.559	23.88	-0.22
28.2	1.30	30.43	0.567	24.12	-0.21
26.6	1.30	30.35	0.571	24.22	-0.20
21.2	1.31	30.48	0.581	24.80	-0.19
19.8	1.31	30.83	0.583	24.91	-0.19
35.8	1.16	26.41	0.544	19.58	-0.26
32.6	1.17	26.37	0.554	20.19	-0.23
28	1.18	26.41	0.567	20.72	-0.22
26.2	1.17	26.41	0.572	20.69	-0.22
23.8	1.17	26.33	0.577	21.00	-0.20
21.2	1.18	26.41	0.581	21.20	-0.20
19.2	1.16	26.37	0.584	21.00	-0.20
39.6	1.02	21.29	0.531	15.68	-0.26
37.2	1.01	21.47	0.539	15.58	-0.27
34.6	1.01	21.44	0.548	15.96	-0.26
32.4	1.01	21.4	0.555	16.18	-0.24
29	1.01	21.29	0.565	16.45	-0.23
26.8	1.02	21.36	0.570	16.82	-0.21
24.4	1.01	21.29	0.575	16.74	-0.21
22.2	1.01	21.25	0.579	16.89	-0.21
20.2	1.01	21.25	0.582	17.01	-0.20
37.4	0.86	17.1	0.539	12.36	-0.28
36.2	0.86	17.2	0.543	12.32	-0.28
32.4	0.86	17.07	0.555	12.66	-0.26
29.8	0.85	17.14	0.563	12.66	-0.26
28.2	0.86	17.17	0.567	12.92	-0.25

Table 15 (continued)

Measured α (Degrees)	Measured H (ft)	Measured Q (ft^3/s)	C_d in Eq. 62	Calculated Q from Eq. 62 (ft^3/s)	Percent Error (%)
24.6	0.86	16.97	0.575	13.10	-0.23
20.6	0.87	17.07	0.582	13.48	-0.21
35.4	0.71	12.62	0.545	9.31	-0.26
31.8	0.73	12.68	0.557	9.85	-0.22
28	0.73	12.65	0.567	10.07	-0.20
26.2	0.71	12.62	0.572	9.86	-0.22
24	0.71	12.65	0.576	9.96	-0.21
22.2	0.71	12.68	0.579	9.84	-0.22
20.2	0.71	12.54	0.582	10.00	-0.20

As can be seen from Table 15, calculated Q with Eq. 62 underestimates the flow rate around 25%. Wahlin and Replogle's (1994) Q equation also underestimated the flow rate about 10%. Several reasons may be considered for the under estimation of Eq. 62 and the error percentage discrepancy between two equations. In one hand, since Q was underestimated in both studies, possible unexpected flow measurements errors in the field study that presented in Wahlin and Replogle (1994) might have contributed to the error range. On the other hand, the average ratio of $\Lambda \frac{\bar{u}^2}{2g} / h$ was 1.3% for the data presented in Wahlin and Replogle (1994), whereas the ratio was 5.6% in the present study in derivation of Eq. 62. The $\Lambda \frac{\bar{u}^2}{2g}$ difference might have also caused a lower discharge coefficient than expected for Eq. 62 to calculate Q for the dataset presented in Wahlin and Replogle (1994). Then, the main potential reason of the error discrepancy, likely is due in large part to the different physical attributes of the gates and the field conditions. The physical differences mentioned before may have resulted in different surface interaction of the gates with the flow, the curvature of the streamlines and possible different flow separation zones for the gate leaves. Comparing the NRMSE and MAPE values, the

accuracy of Eq. 62 was found to be substantially higher for the data gathered in the present study compared to that reported by Wahlin and Replogle (1994).

4.3 Implications of the Use of Total Energy Head

To reduce the uncertainty in C_d, H was used in the developed head-discharge equation rather than only employing h. The ratio of $\Lambda \frac{\bar{u}^2}{2g}$, calculated using the average value Λ = 1.1, to h was examined to depict the importance of including the upstream canal velocity head term in discharge calculations. A significant effect was noted particularly for high flow conditions. The ratio $\Lambda \frac{\bar{u}^2}{2g}$ to h reached 9% for the highest recorded velocity (1.93 ft/s at Gate A). The average ratio of $\Lambda \frac{\bar{u}^2}{2g}$ to h across the measured flows was 5.6 %. Therefore, neglecting the velocity head might be misleading in assessing flow over adjustable overshot gates, and likely increases the uncertainty in estimating C_d.

4.4 Effect of Gate Inclination Angle on Discharge

Prakash et al. (2011) conducted laboratory experiments for different inclination angles (0°, 15°, 30°, 45°, and 60°) and showed that C_d *increased* with increasing α by 36% for 20°-40°. However, laboratory experiments (for inclination angles of 0°, 20°, 40°, 60°, 80°, 90°) by Nikou et al. (2016) revealed that C_d *decreased* with increasing α by 61.7% for 20°-40°. Also, Bijankhan et al. (2018) showed that Q increased by 8% for α = 30° and 7% for α = 40° compared to α = 90°, while Q was not affected by the gate inclination for 54° ≤ α ≤ 90°. In the present study, C_d also *decreased* with increasing α by 11% for 22.8° - 40.4°. This behavior may be explained by streamline curvature. Low values of α provide for less curvature of streamlines and thus, less

energy loss between upstream and the crest of the weir (Bos 1976). The resulting distribution of forces acting on the gate system also may have contributed to higher C_d values for lower α.

As can be seen from Figure 37 (Chapter 3, Part 2.4.2), increasing α generally caused the C_d to decrease. However, for the angles of 32.6° and 35.3°, very similar *m* values were calculated. For α = 34.6°, the value of *m* was higher than for the angles of 32.6° and 35.3°. These results indicate that more data are needed to depict the relationship between C_d and α more precisely. This apparent inconsistency may be explained in part by a difference in physical characteristics for Gate B, for which α values of 35.3°, 38.9°, and 40.4° were observed. First, the sidewall geometry of Gate B might have influenced the measured discharge ratios. Gate B has a different sidewall configuration on the right bank than do the other gates. Upstream of the gate, the canal had an additional concrete retaining wall on the right side (45 ft in length). The unmeasured zone of the ADCP on the right bank of the canal might have contributed the inconsistency, since the hydraulic roughness is greater for vegetated surfaces. Second, Gunawan et al. (2009) stated that the existence of vegetation and debris accumulation at the vegetated canal banks hinders the accuracy of the bottom tracking mode of the ADCP rendering additional error in velocity readings. On the right bank of Gate B, the absence of vegetation could present be a discrepancy in the dataset. Figure 54 displays the difference between the canal transects at the location of ADCP measurements for Gate B and Gate C as an example. As can be seen on the left-hand side of the figure, Gate B led to an easy Bluetooth connection between the laptop computer and the device so that the data transfer process was sustained more easily. Furthermore, the bottom tracking mode of the device was expected to be more accurate for Gate B, as compared to the gates with

vegetated banks. These differences could have contributed to some of the discrepancies in the data of Figure 37.

(a) (b)

Figure 54. Channel transects for ADCP measurements at (a) Gate B, and b) Gate C, revealing different geometric and roughness characteristics.

Di Stefano et al. (2018) indicated that α had a negligible effect on the discharge capacity of overshot gates. The researchers presented a constant value C_d = 0.723 using the laboratory test data presented in Wahlin and Replogle (1994), for free flow conditions. Values of α ranged between 24° and 71.6° for the dataset. However, in the present study, C_d independent of α was calculated as 0.565. The difference may be associated with the field study characteristics, such as higher variability in roughness, geometry, velocity distribution, and turbulence etc., compared to those in the controlled laboratory study. The use of *H* in the head-discharge equation of the present study, in contrast to *h* in the Di Stefano et al. (2018) study, might have also contributed to the difference in computed C_d.

4.5 Modular Limit of Adjustable Overshot Gates

Submergence of a hydraulic control structure can be described by examining the effect of downstream flow depth on the discharge. Wu and Rajaratnam (1996) showed that with an increase of the tailwater level relative to the crest of a weir, discharge over the structure relied on not only *H* upstream but also on the downstream flow depth relative to the crest. The authors also described the submergence ratio, *S*, as that of the downstream flow depth relative to the crest to *h*. A submergence factor was recommended for multiplication by the discharge equation derived under free flow conditions to estimate the flow rate for submerged flow conditions:

$$Q_s = \psi\, Q \tag{65}$$

where, Q_s is the discharge under submerged flow conditions [L^2/T], ψ is the submergence factor, and Q is the discharge derived under free flow equation [L^2/T]. Above a certain value for S, ψ decreases below 1 with increasing *S.*

Hager and Schwalt (1994) presented the submergence limit, or modular limit, which is the value of *S* that marks the transition between free and submerged flows, and is a significant characteristic of a hydraulic control structure. Vanishree and Manjula (2018) emphasized that submergence does not affect the free flow discharge equation up to S = 0.48 for labyrinth weirs. Göğüş et al. (2006) observed that the modular limits of broad-crested weirs with compound rectangular cross sections were less than those for rectangular cross sectioned broad crested weirs considering the same height and length of crest. Azimi et al. (2014) determined the modular limits of weirs with finite crest thickness (weirs classification used in the study were based on Rao and Muralidhar, 1963) to fall between 0.58 and 0.83, whereas the authors indicated

a modular limit of 0.83 for broad-crested weirs. The researchers also defined the submergence factor for square-edge broad-crested weirs by the following equation:

$$\Psi = [1-(S)^{10}]^{0.95} \quad (66)$$

Villemonte (1947) performed experiments on different types of submerged sharp-crested weirs, and observed a modular limit of 0.1 with the submergence factor as follows:

$$\Psi = [1-S^{3/2}]^{0.385} \quad (67)$$

During data collection in this study, for Q between 173 ft^3/s and 266 ft^3/s, the downstream flow depths were higher than the crest of the weir for Gate C. Thus, submerged flow conditions were considered. Freely circulating flow conditions, which are significant for submerged flow measurements, were examined at downstream of Gate C. There was a concrete foundation with a thickness of 1 ft supporting the gate. The foundation lay along the longitudinal cross section of the gate leaf. Downstream of the foundation, a sharp drop formed to the canal bed. Hence, after the flow passed over the crest of the gate, the streamlines suddenly dropped. This drop allowed water profiles to freely circulate at the downstream side of the gate. In addition, the expanding geometry of the concrete retaining walls downstream of the gate leaf contributed to the free circulation of the flow profiles.

Values of the downstream flow depth relative to the crest were measured at Gate C using pressure transducers (Chapter 3, Part 1.2.2) and S was calculated to range 0.03 – 0.51. For these S values, the modular limit of Gate C was inspected with respect to the collected data.

Considering their physical features, the behavior of adjustable overshot gates might be expected to lie between that of sharp- and broad-crested weirs. Therefore, the modular limits of the adjustable overshot gates were expected to fall between those reported for sharp- and

broad-crested weirs. Since Q_s is calculated by multiplying the submergence factor by Q, the inverse of the submergence factor, $1/\psi = Q/Q_s$, of the sharp and broad-crested weirs have been utilized to depict the impact of S on different types of weirs (Figure 55). Recall that modular limits were determined to be 0.1 for the sharp crested weirs (Villemonte 1947) and 0.85 for the broad crested weirs (Azimi et al. 2014).

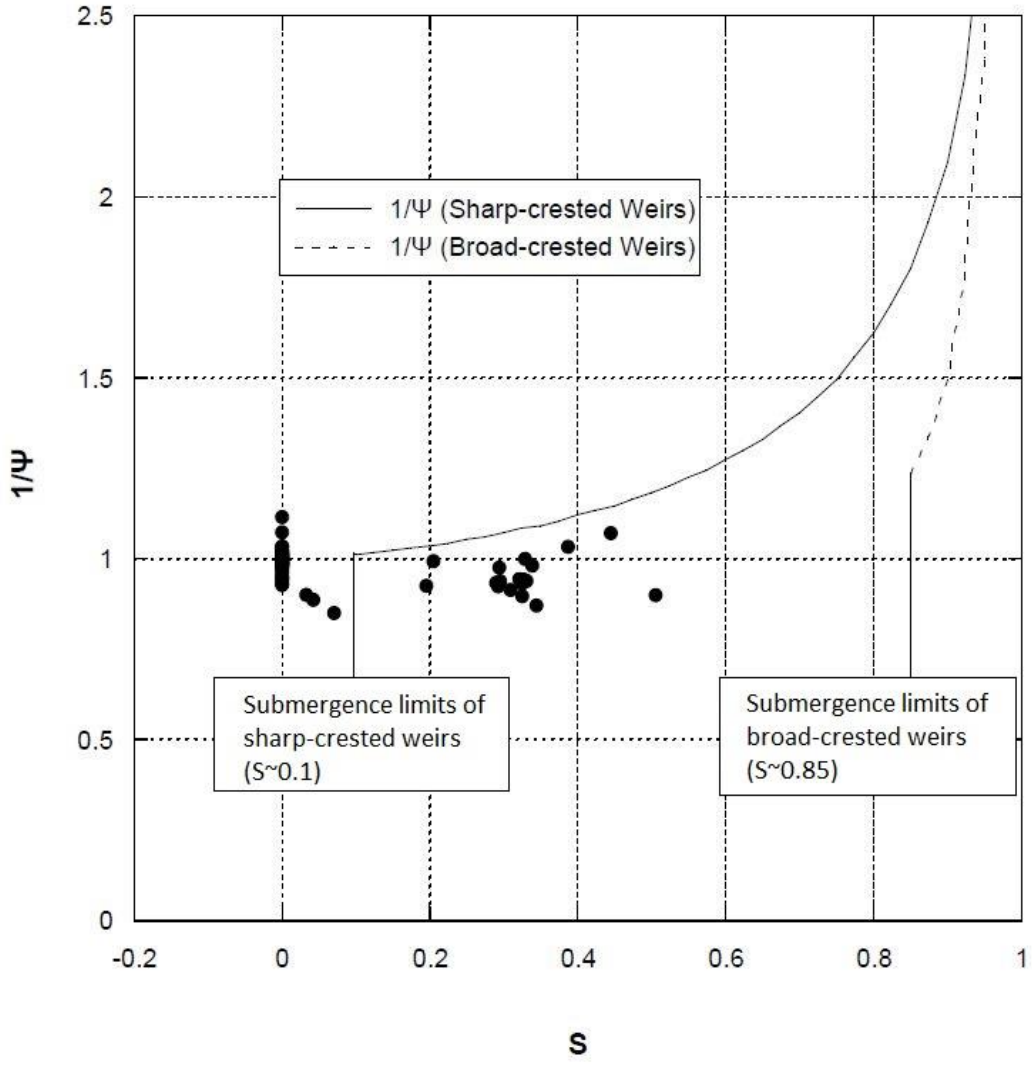

Figure 55. Modular limit assessment considering the impact of submergence ratio on inverse of reduction factor for Obermeyer Adjustable Overshot Gates in Comparison to that for Sharp-Crested and Broad-Crested Weirs.

In Figure 55 the modular limit can be assessed as the value of S at which the value of $1/\psi$ grows significantly above a value of 1. The plotted data indicate that the modular limit for Gate C could not be identified for S values up to about 0.51. Thus, it was concluded that Gate C was operating under free flow conditions in this study. The results indicate that the modular limit for Obermeyer adjustable overshot gates exceeds 0.51, indeed lying well above that for a sharp-crested weir, but determination of the actual value will require additional data under higher tailwater conditions.

CHAPTER 5

CONCLUSION AND IMPLICATIONS

Research was carried out under actual operating field conditions to provide a practical relationship between head and discharge for Obermeyer-type adjustable overshot gates. The study examines the applicability of the relationship to another type of overshot gate, the effect of the velocity head and the gate inclination angle on discharge estimation, and the modular limit of the equation in relation to submergence conditions. An improved understanding of the hydraulic behavior of overshot gates has resulted.

Three alternative forms of head-discharge equations, previously derived in the literature from dimensional analysis and controlled laboratory experiments, were considered. These alternative forms, were applied with data collected from three Obermeyer-type overshot gates under actual operating conditions in the field. The first equation (Eq. 61) was obtained by expressing both the coefficient and the exponent of a power equation as a function of the gate inclination angle, α. The second equation (Eq. 62) was obtained by equating the exponent of the power equation to 1 and determining the coefficient as a function of α, resulting in a classical sharp-crested weir head-discharge equation with the discharge coefficient, C_d, dependent upon α. The third equation (Eq. 63) was obtained by equating the exponent of the power equation to 1 and treating the coefficient as independent of α, resulting in a classical sharp-crested weir head-discharge equation with constant C_d. Considering RMSE and NRMSE values, Eq. 62 was found slightly more accurate than the other head-discharge equations, as might be expected considering the effect that α has on the nature of the flow over the gates. The accuracy of the

head-discharge equation was within ±10% for a wide range of discharge values (20.4 ft^3/s - 330 ft^3/s) and for α ranging 22.8° - 40.4°.

The best-fit head-discharge equation (Eq.62) was examined using another field dataset for Armtec overshot gates under free flow conditions. Comparing NRMSE and MAPE values, a distinctive difference in the performance of the equation was found between applications to the two different datasets, due to dissimilar gate characteristics and field conditions.

To reduce the uncertainty embedded within an evaluation of C_d and to comprehend the velocity head effect on estimates of discharge, the total mechanical energy upstream*, H,* was used in the head-discharge equation, rather than simply employing the upstream flow depth relative to the crest, *h*. The ratio of the upstream canal velocity head to *h* was calculated as 9% maximum and 5.6% average. This analysis showed that neglecting the upstream velocity head could result in misleading flow rate calculations.

The effect of α on the discharge over overshot gates was analyzed in this study due to a difference in opinion within the literature. Considering C_d values that decreased with increasing α rendered a head-discharge relation that performed (with respect to RMSE and NRMSE values) slightly better than an equation with constant C_d for the field setting of this study, in contrast to results from some of the laboratory experiments reported in the literature.

The modular limit of the adjustable overshot gates was examined in order to determine the submergence effect of tailwater levels on the discharge calculations. A tailwater effect was not observed up to a submergence ratio of 0.51. The analysis showed that the Obermeyer adjustable overshot gates have a markedly higher submergence tolerance than sharp-crested

weirs. However, more field data are required to estimate the actual submergence limits of adjustable overshot gates.

At the practical level, overshot gates generally are used to control water levels in irrigation canals, primarily for flow diversion upstream of the gates. The head-discharge equation developed here can be used for design and operation of irrigation canals providing guidance for adjustment of the upstream water levels to target values for a range of Q values by altering design dimensions, like b and L_G, and/or adjusting α of the gate leaves. In addition to controlling water levels, this study has demonstrated that overshot gates could be exploited to estimate canal flow rate from measured values of h in the field. An accurate description of canal geometry at the point of measurement is required to represent the canal flow area A as a function of h, permitting H to be represented in the head-discharge equation as a function of h and Q. Measuring flow over the structures also could be used to estimate lateral inflows or outflows and canal seepage between the structures. The present findings about the level of uncertainty in the head-discharge relationship allows notions of risk and probability to be taken into account in making decisions about gate design and operation.

REFERENCES

Afzalimehr, H., & Bagheri, S. (2009). Discharge coefficient of sharp-crested weirs using potential flow. *Journal of Hydraulic Research, 47*(6), 820-823. doi:10.3826/jhr.2009.3609

Akan, A. O. (2011). *Open Channel Hydraulics*. Burlington: Elsevier Science.

Ali, M. H. (2010). *Fundamentals of Irrigation and on-farm Water Management*. New York: Springer.

ANSYS R18.1 (2017). [Computer software]. http://www.ansys.com

Arvanaghi, H., & Oskuei, N. N. (2013). Sharp-crested weir discharge coefficient. *Journal of Civil Engineering and Urbanism*, *3*(3), 87-91.

Ashkar, F., & Mahdi, S. (2006). Fitting the log-logistic distribution by generalized moments. *Journal of Hydrology*, *328*(3-4), 694-703.

Aydin, I., Altan-Sakarya, A. B., & Sisman, C. (2011). Discharge formula for rectangular sharp-crested weirs. *Flow Measurement and Instrumentation, 22*(2), 144-151. doi:10.1016/j.flowmeasinst.2011.01.003

Azimfar, S. M., Hosseini, S. A., & Khosrojerrdi, A. (2018). Derivation of discharge coefficient of a pivot weir under free and submergence flow conditions. *Flow Measurement and Instrumentation*, *59*, 45-51.

Azimi, A. H., & Rajaratnam, N. (2009). Discharge characteristics of weirs of finite crest length. *Journal of Hydraulic Engineering, 135*(12), 1081-1085. doi: 10.1061/ (ASCE) hy.1943-7900.0000117

Azimi, A. H., Rajaratnam, N., & Zhu, D. Z. (2014). Submerged flows over rectangular weirs of finite crest length. *Journal of Irrigation and Drainage Engineering, 140*(5), 06014001. doi: 10.1061/ (ASCE) ir.1943-4774.0000728

Bagheri, S., & Heidarpour, M. (2010). Flow over rectangular sharp-crested weirs. *Irrigation science*, *28*(2), 173.

Barenblatt, G. I. (1979). *Similarity*, *Self-Similarity, and Intermediate Asymptotics.* Consultants Bureau, New York, 218.

Barenblatt, G. I. (1987). *Dimensional Analysis*. New York, U.S.A: Gordon and Breach Science.

Barenblatt, G. I. (1996). *Scaling, Self-similarity and Intermediate Asymptotics*. Cambridge: Cambridge Univ. Press.

Bijankhan, M., Di Stefano, C., Ferro, V., & Kouchakzadeh, S. (2013). New stage-discharge relationship for weirs of finite crest length. *Journal of Irrigation and Drainage Engineering*, *140*(3), 06013006.

Bijankhan, M., & Ferro, V. (2017). Dimensional analysis and stage-discharge relationship for weirs: A review. *Journal of Agricultural Engineering, 48*(1), 1. doi:10.4081/jae.2017.575

Bijankhan, M., & Ferro, V. (2018). Experimental study and numerical simulation of inclined rectangular weirs. *Journal of Irrigation and Drainage Engineering*, *144*(7), 04018012.

Bilhan, O., Emiroglu, M. E., & Miller, C. J. (2016). Experimental investigation of discharge capacity of labyrinth weirs with and without nappe breakers. *World Journal of Mechanics*, *6*(07), 207.

Boiten, W. (2002). Flow measurement structures. *Flow Measurement and Instrumentation, 13*(5-6), 203-207. doi: 10.1016/s0955-5986(02)00057-2

Borghei, S. M., Jalili, M. R., & Ghodsian, M. A. S. O. U. D. (1999). Discharge coefficient for sharp-crested side weir in subcritical flow. *Journal of Hydraulic Engineering*, *125*(10), 1051-1056.

Borghei, S. M., Vatannia, Z., Ghodsian, M., & Jalili, M. R. (2003). Oblique rectangular sharp-crested weir. *Proceedings of the Institution of Civil Engineers - Water and Maritime Engineering, 156*(2), 185-191. doi:10.1680/wame.2003.156.2.185

Bos, M. (1976). *Discharge Measurement Structures*. Wageningen: ILRI.

Bouman, B., & Laar, H. V. (2006). Description and evaluation of the rice growth model ORYZA2000 under nitrogen-limited conditions. *Agricultural Systems, 87*(3), 249-273. doi:10.1016/j.agsy.2004.09.011

Cash, J. R., & Karp, A. H. (1990). A variable order Runge-Kutta method for initial value problems with rapidly varying right-hand sides. *ACM Transactions on Mathematical Software (TOMS)*, *16*(3), 201-222.

Campbell Scientific flow measurement instruments and PC200W software (rugged monitoring)-measurement and control instrumentation for any application. (2006). Retrieved from https://www.campbellsci.com/ Last visited (12.02.2018)

CFD post-user guide (streamline command). (2015, June 29). Retrieved from https://www.sharcnet.ca/Software/Ansys/16.2.3/en-us/help/cfd_post/i1302090.html Last visited (11.25.2018)

Chandler, M. (1998). Buckingham Pi Theorem.

Chen, C. (1991). Unified theory on power laws for flow resistance. *Journal of Hydraulic Engineering, 117*(3), 371-389. doi: 10.1061/ (ASCE) 0733-9429(1991)117:3(371)

Chen, Y. S., & Kim, S. W. (1987). Computation of turbulent flows using an extended k-epsilon turbulence closure model. *Technical report* CR-179204, NASA.

De Martino, G., & Ragone, A. (1984). Effects of viscosity and surface tension on slot weirs flow. *Journal of Hydraulic Research*, *22*(5), 327-341.

Di Stefano, C., & Ferro, V. (2013). A new approach for deducing the stage-discharge relationship of triangular in plan sharp-crested weirs. *Flow Measurement and Instrumentation*, *32*, 71-75.

Di Stefano, C., Ferro, V., & Bijankhan, M. (2016). New theoretical solution of the outflow process for a weir with complex shape. *Journal of Irrigation and Drainage Engineering*, *142*(10), 04016036.

Di Stefano, C., Ferro, V., & Bijankhan, M. (2018). Discussion of "Extraction of the flow rate equation under free and submerged flow conditions in pivot weirs with different side contractions" by N. Sheikh Rezazadeh Nikou, M. J. Monem, and K. Safavi. J*ournal of Irrigation and Drainage Engineering*, 144(4), 04016025

Environment Canada, (2013). Measuring discharge with acoustic Doppler current profilers from a moving boat, version adapted for Water Survey of Canada, 62 p.

Fenton, J. D. (2015). Calculating flow over rectangular sharp-edged weirs. *Technical report, Alternative Hydraulics Paper 6.* http://johndfenton. com/Papers/Calculating-flow-over-rectangular-sharpedged-weirs.pdf.

Ferro, V. (1997). Applying hypothesis of self-similarity for flow-resistance law of small-diameter plastic pipes. *Journal of Irrigation and Drainage Engineering, 123*(3), 175-179. doi: 10.1061/ (ASCE) 0733-9437(1997)123:3(175)

Ferro, V. (2000). Simultaneous flow over and under a gate. *Journal of Irrigation and Drainage Engineering, 126*(3), 190-193. doi: 10.1061/ (ASCE) 0733-9437(2000)126:3(190)

Ferro, V., & Pecoraro, R. (2000). Incomplete self-similarity and flow velocity in gravel bed channels. *Water Resources Research, 36*(9), 2761-2769. doi: 10.1029/2000wr900164

Ferro, V. (2011). New theoretical solution of the stage-discharge relationship for sharp-crested and broad weirs. *Journal of Irrigation and Drainage Engineering*, *138*(3), 257-265.

French, R. H. (1985). *Open Channel Hydraulics*. New York: McGraw-Hill.

Geological Survey (US), & Rantz, S. E. (1981). Measurement and computation of streamflow: Volume 1: measurement of stage and discharge.

Gore, J. A., & Banning, J. (2017). Discharge measurements and streamflow analysis. *Methods in Stream Ecology, Volume 1,* 49-70. doi:10.1016/b978-0-12-416558-8.00003-2

Gordon, R. L. (1989). Acoustic measurement of river discharge. *Journal of hydraulic Engineering*, *115*(7), 925-936.

Gunawan, B., Sterling, M., & Knight, D. W. (2009). Using an acoustic Doppler current profiler in a small river. *Water and Environment Journal, 24*(2), 147-158. doi:10.1111/j.1747-6593.2009.00170.

González, J. A., Melching, C. S., & Oberg, K. A. (1996, September). Analysis of open-channel velocity measurements collected with an acoustic Doppler current profiler. In *the 1st International Conference on New/Emerging Concepts for Rivers, the International Water Resources Association, Chicago, Illinois, USA*.

Göğüş, M., Defne, Z., & Özkandemir, V. (2006). Broad-crested weirs with rectangular compound cross sections. *Journal of Irrigation and Drainage Engineering, 132*(3), 272-280. doi: 10.1061/ (ASCE) 0733-9437(2006)132:3(272)

Hager, W. H., & Schwalt, M. (1994). Broad-crested weir. *Journal of Irrigation and Drainage Engineering*, *120*(1), 13-26.

Henderson, F. M. (1966). *Open Channel Flow* (No. 532 H4).

Hirt, C., & Nichols, B. (1981). Volume of fluid (VOF) method for the dynamics of free boundaries. *Journal of Computational Physics, 39*(1), 201-225. doi: 10.1016/0021-9991(81)90145-5

Hulsing, H. (1968). Measurement of peak discharge at dams by indirect method. *Techniques of Water Resources Investigations, U.S. Geological Survey, Book 3(A5).* U.S. Government Printing Office, Washington, D.C.

Instruments, R. D. (1996). Principles of operation a practical primer. Available from http://www.RDInstruments.com. Last visited (10.15.2018)

Johnson, M. C. (2000). Discharge coefficient analysis for flat-topped and sharp-crested weirs. *Irrigation Science, 19*(3), 133-137. doi: 10.1007/s002719900009

KaleidaGraph [Computer software]. *Synergy Software*. http://www.synergy.com

Khalili Shayan, H., Aminpour, Y., Peysokhan, P., & Bayrami, M. (2018). Discussion of "Extraction of the flow rate equation under free and submerged flow conditions in pivot weirs with different side contractions" by N. Sheikh Rezazadeh Nikou, MJ Monem, and K. Safavi. *Journal of Irrigation and Drainage Engineering*, *144*(4), 07018008.

Kindsvater, C. E., & Carter, R. W. (1959). Discharge characteristics of rectangular thin-plate weirs. *Transactions of the American Society of Civil Engineers*, *124*(1), 772-801.

Lee, K., Ho, H. C., Marian, M., & Wu, C. H. (2014). Uncertainty in open channel discharge measurements acquired with StreamPro ADCP. *Journal of hydrology*, *509*, 101-114.

Martínez, J., Reca, J., Morillas, M. T., & López, J. G. (2005). Design and calibration of a compound sharp-crested weir. *Journal of Hydraulic Engineering, 131*(2), 112-116. doi: 10.1061/ (ASCE) 0733-9429(2005)131:2(112)

Molden, D. J., & Gates, T. K. (1990). Performance measures for evaluation of irrigation-water-delivery systems. *Journal of irrigation and drainage engineering*, *116*(6), 804-823.

Morlock, S. E. (1996). Evaluation of acoustic Doppler current profiler measurements of river discharge (pp. 95-4218). US Department of the Interior, US Geological Survey.

Motulsky, H. J., & Ransnas, L. A. (1987). Fitting curves to data using nonlinear regression: A practical and nonmathematical review. *The FASEB Journal, 1*(5), 365-374. doi:10.1096/fasebj.1.5.3315805

Mueller, D. S., Wagner, C. R., Rehmel, M. S., Oberg, K. A., & Rainville, F. (2013). Measuring discharge with acoustic Doppler current profilers from a moving boat. *Techniques and Methods*. doi: 10.3133/tm3a22

Muste, M., Yu, K., & Spasojevic, M. (2004). Practical aspects of ADCP data use for quantification of mean river flow characteristics; Part I: moving-vessel measurements. *Flow measurement and instrumentation*, *15*(1), 1-16.

Nikou, N. S., Monem, M. J., & Safavi, K. (2016). Extraction of the flow rate equation under free and submerged flow conditions in pivot weirs with different side contractions. *Journal of Irrigation and Drainage Engineering, 142*(8), 04016025. doi: 10.1061/ (ASCE) ir.1943-4774.0001027

Nikou, N. S. R., Ziaei, A. N., & Safavi, K. (2018). Closure to "Extraction of the flow rate equation under free and submerged flow conditions in pivot weirs with different side contractions" by N. Sheikh Rezazadeh Nikou, M.J. Monem, and K. Safavi. *Journal of Irrigation and Drainage Engineering*, *144*(4), 07018009.

Prakash, M. S., Ananthayya, M. B., & Kovoor, G. M. (2011). Inclined rectangular weir-flow modeling. *Earth Science India*, *4*.

Rady, R. A. E. H. (2011). 2D-3D modeling of flow over sharp-crested weirs. *Journal of applied sciences research*, *7*(12), 2495-2505.

Ramamurthy, A. S., Tim, U. S., & Rao, M. V. (1987). Flow over sharp-crested plate weirs. *Journal of Irrigation and Drainage Engineering, 113*(2), 163-172. doi: 10.1061/ (ASCE) 0733-9437(1987)113:2(163)

Ramooz, R., & Rennie, C. D. (2010). Laboratory measurement of bed-load with an ADCP. Bedload-Surrogate Monitoring Technologies; US Geological Survey Scientific Investigations Report, 5091.

Rao, N. S., & Muralidhar, D. (1963). Discharge characteristics of weirs of finite-crest width. *La Houille Blanche,* (5), 537-545. doi:10.1051/lhb/1963036

Rao, S. S., & Shukla, M. K. (1971). Characteristics of flow over weirs of finite crest width. *Journal of the Hydraulics Division*, *97*(11), 1807-1816

Rehbock, T. (1929). Discussion of" Precise measurements". *Trans. of ASCE*, *93*, 1143-1162.

RISK, (@RISK). [Computer software]. http://palisade.com

Sargison, J. E., & Percy, A. (2009). Hydraulics of broad-crested weirs with varying side slopes. *Journal of Irrigation and Drainage Engineering, 135*(1), 115-118.

Shen, J. (1981). Discharge characteristics of triangular-notch thin-plate weirs (No. 1617). United States Department of the Interior, Geological Survey.

Singh, S. (2012). *Experiments in Fluid Mechanics*. PHI Learning Pvt. Ltd.

Skogerboe, G. V., Hyatt, M. L., Anderson, R. K., & Eggleston, K. O. (1967). Design and calibration of submerged open channel flow measurement structures: Part 4-Weirs. doi: 10.1061/ (ASCE) 0733-9437(2009)135:1(115)

Sonin, A. A. (2001). The Physical Basis of Dimensional Analysis, Ain A.

StreamPro ADCP User's Guide - Teledyne Marine. (September 2015). Retrieved from http://www.teledynemarine.com Last visited (12.12.2018)

Subramanya, K. (1982). *Flow in Open Channels*. New Delhi: Tata McGraw-Hill.

Swamee, P. K. (1988). Generalized rectangular weir equations. *Journal of Hydraulic Engineering 114*(8), 945-949. doi: 10.1061/ (ASCE) 0733-9429(1988)114:8(945)

Swamee, P. K., Pathak, S. K., & Ghodsian, M. (2001). Viscosity and surface tension effects on rectangular weirs. *ISH Journal of Hydraulic Engineering, 7*(2), 45-50. doi:10.1080/09715010.2001.10514697

Tashman, L. J. (2000). Out-of-sample tests of forecasting accuracy: an analysis and review. *International journal of forecasting*, *16*(4), 437-450.

Taylor, G. (1968). The performance of labyrinth weirs (Doctoral dissertation, University of Nottingham).

Tracy, H. J. (1957). Discharge characteristics of broad-crested weirs (Vol. 397). US Department of the Interior, Geological Survey.

USBR Water Measurement Manual. (2001). Retrieved from https://www.usbr.gov/tsc/techreferences/mands/wmm/WMM_3rd_2001.pdf Last visited (10.08.2018)

Vanishree, B. R., & Manjula, R. (2018). Analysis of various parameters affecting weir design and fabrication of weirs: An overview. *MATEC Web of Conferences, 144*, 01006. doi:10.1051/matecconf/201714401006

Vatankhah, A. R. (2010). Flow measurement using circular sharp-crested weirs. *Flow Measurement and Instrumentation, 21*(2), 118-122. doi:10.1016/j.flowmeasinst.2010.01.006

Villemonte, J. R. (1947). Submerged weir discharge studies. *Engineering News-Record*, *139*(26), 54-56.

Wahlin, B. T., & Replogle, J. A. (1994). Flow measurement using an overshot gate. Phoenix, AZ: UMA Engineering.

White, F. M. (1994). The Buckingham-Pi theorem in dimensional analysis. *Fluid Mechanics Sections*, 5-1.

White, F. M. (2003). *Fluid Mechanics*. Boston: McGraw-Hill.

WinRiver II Software User's Guide – Teledyne Marine. (August, 2016). Retrieved from http://www.teledynemarine.com Last visited (12.24.2018)

Wu, S., & Rajaratnam, N. (1996). Submerged flow regimes of rectangular sharp-crested weirs. *Journal of Hydraulic Engineering, 122*(7), 412-414. doi: 10.1061/ (ASCE) 0733-9429(1996)122:7(412)

APPENDIX 1

ASSEMBLY PROJECTS OF OBERMEYER-TYPE OVERSHOT GATES (Gates A and B)

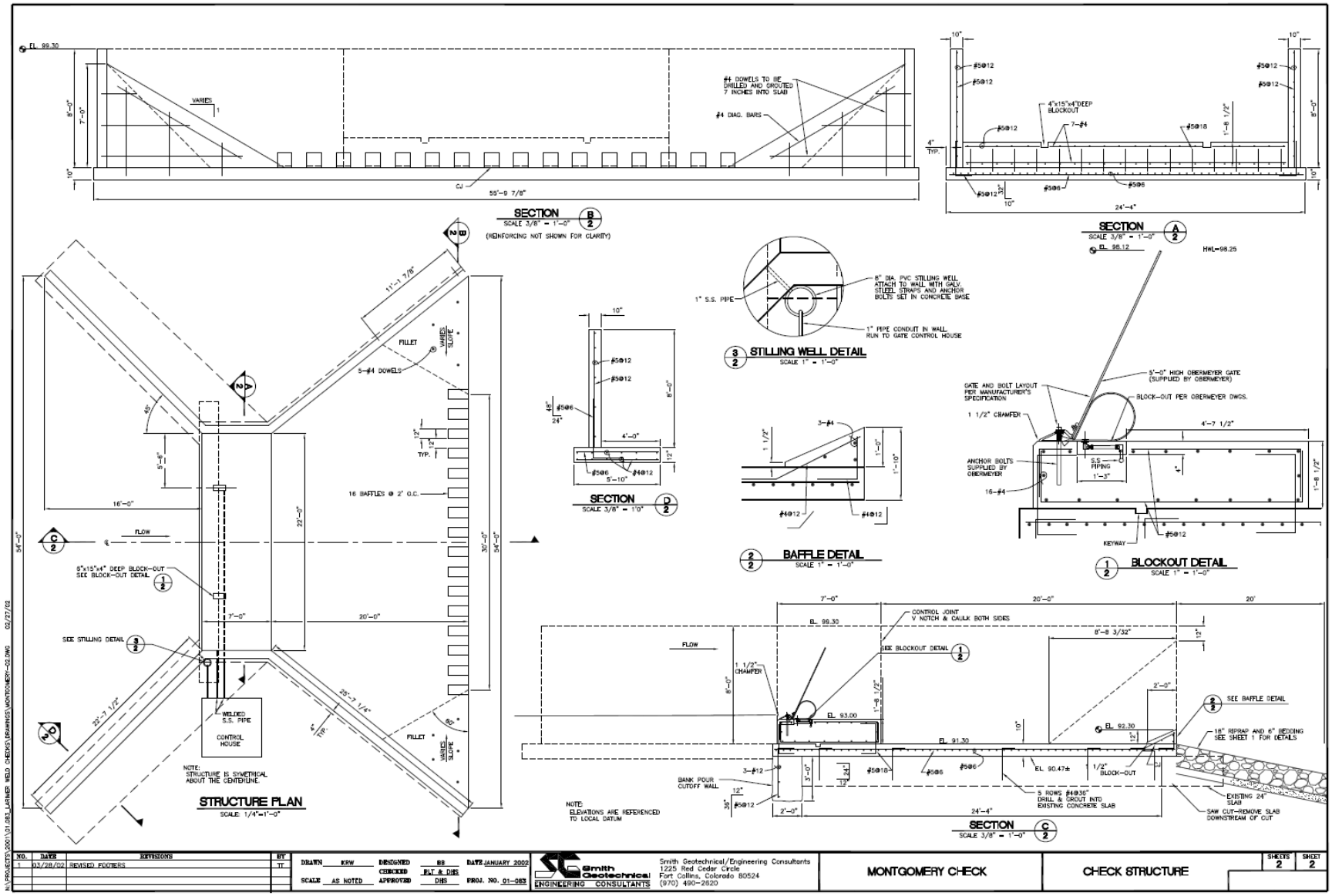

Figure 56. Assembly project of Montgomery Check Structure (Gate A)

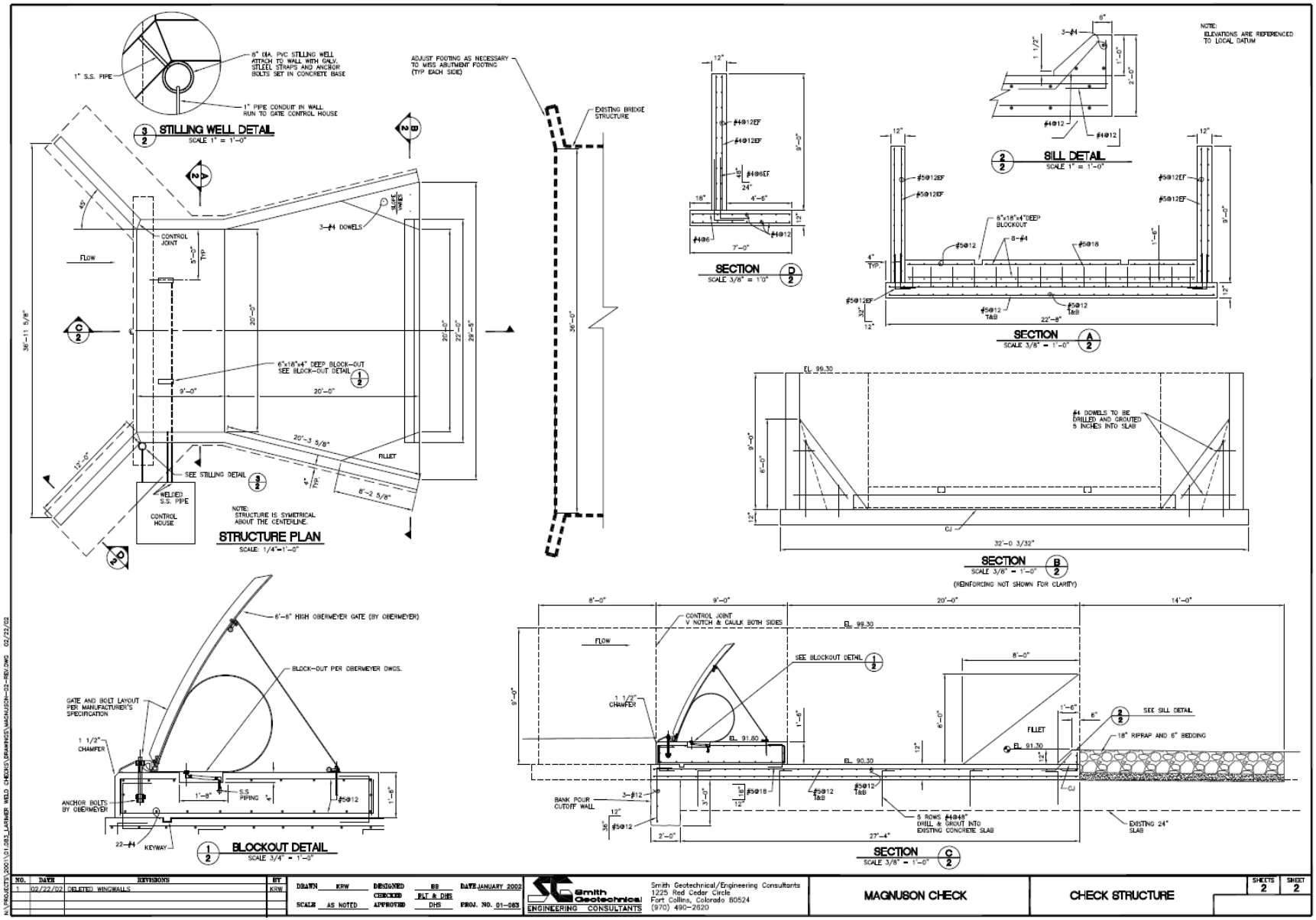

Figure 57. Assembly project of Magnuson Check Structure (Gate B)

APPENDIX 2

Calibration Documentation from USGS for ADCP Used in This Study

Test Date:	7/6/2017	Hydrologic Instrumentation Facility
Result	Pass	Building 2101, Stennis Space Center, MS

INSTRUMENT

Manufacturer:	TRDI
Model:	StreamPro
Serial Number:	861
Probe Serial Number:	12295

OWNER

Water Science Center:	Fort Collins
Contact:	Caner Kutlu

Mhz SUMMARY

Heading (deg)	DMG (m)	Ratio	Error (%)	Pass/Fail
0	22.933	1.0057	0.57	Pass
45	22.838	1.0015	0.15	Pass
90	22.8638	1.0027	0.27	Pass
135	22.9327	1.0057	0.57	Pass

TEST REFERENCE DATA

Reference Distance: 22.8033222

Transformation Matrix:

1.48	-1.4763	0.0318	-0.0314
0.0304	-0.0358	-1.4814	1.4859
0.2602	0.2708	0.2633	0.268
1.0466	1.0487	-1.0507	-1.0436

TRANSECTS	Heading (deg)	DMG (m)	No. Pts.	No. Bad	Ratio	Error (%)	
86120170706_0_000.PD0	91	22.844	241	0	1.0018	0.18	Pass
86120170706_0_001.PD0	271	22.8909	207	0	1.0038	0.38	Pass
86120170706_0_002.PD0	91	22.8567	211	0	1.0023	0.23	Pass
86120170706_0_003.PD0	271	22.8636	208	0	1.0026	0.26	Pass
86120170706_0_004.PD0	132	22.9238	216	0	1.0053	0.53	Pass
86120170706_0_005.PD0	313	22.9149	215	0	1.0049	0.49	Pass
86120170706_0_006.PD0	133	22.9708	214	0	1.0073	0.73	Pass
86120170706_0_007.PD0	313	22.9212	212	0	1.0052	0.52	Pass
86120170706_0_008.PD0	179	22.9248	212	0	1.0054	0.54	Pass
86120170706_0_009.PD0	359	22.9416	209	0	1.006	0.6	Pass
86120170706_0_010.PD0	179	22.9266	210	0	1.0054	0.54	Pass
86120170706_0_011.PD0	359	22.9387	206	0	1.0059	0.59	Pass
86120170706_0_012.PD0	223	22.8152	251	0	1.0006	0.06	Pass
86120170706_0_013.PD0	43	22.8533	211	0	1.0022	0.22	Pass
86120170706_0_014.PD0	222	22.8426	207	0	1.0017	0.17	Pass
86120170706_0_015.PD0	43	22.8411	216	0	1.0016	0.16	Pass

Temperature Probe Check

Reference Temp. (C)	Average* ADCP Temp. (C)
26.76	25.5
Temperature Probe	Pass

*Avereage of 25 meter readings

Run Location: Large Acoustic Tank
RDI Bottom Track Limit (+/- 1.0 %, +/- 2 mm/s)

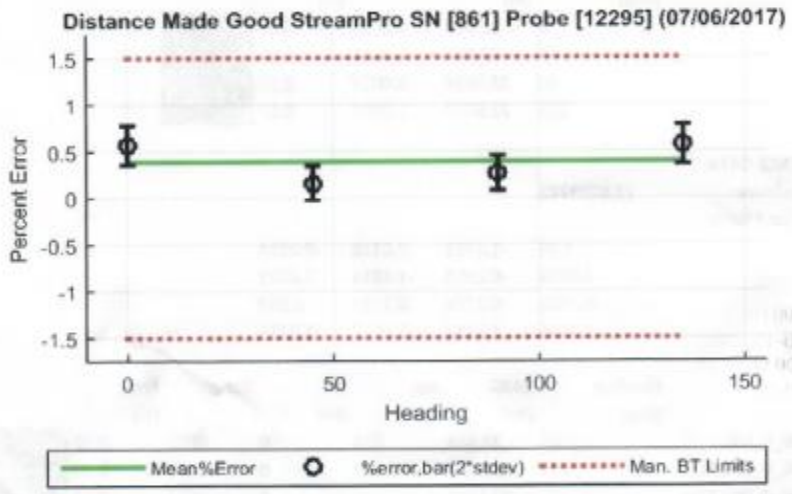

```
ans =

=
StreamPro
Teledyne RD Instruments (c) 2010
All rights reserved.
Firmware Version: 31.15

>CR1
[Parameters set to FACTORY]

>
>TS?
TS 17/07/06,08:59:49.63
>
>PS0
  Serial Number:  861
     Frequency:  2000000 Hz
  Configuration:  4 BM, JANUS
    Beam Angle:  20 DEGREES
   CPU Firmware:  31.15
   FPGA Version:  3.00.005
      Compass :  Not Installed

ROM_ID:  C7 00 00 01 89 3E E1 28
Part Num:
ROM_ID:  5D 00 00 00 8B 39 0A 23
Part Num: DSP72B-2002-12D
ROM_ID:  6D 00 00 00 B7 D8 06 23
Part Num: XDR82B-1003-00A
ROM_ID:  E9 00 00 00 94 D1 5E 23
Part Num: RCV72B-2003-12A
ROM_ID:  FF 00 00 00 B7 D4 85 23
Part Num: PIO72B-2001-12B
ROM_ID:  A7 00 00 00 6D 80 3F 23
Part Num: PER72B-2006-00A

>
>PS3
 1.4800 -1.4763  0.0318 -0.0314
 0.0304 -0.0358 -1.4814  1.4859
 0.2602  0.2708  0.2633  0.2680
 1.0466  1.0487 -1.0507 -1.0436


>
>PT2
17/07/06 08:59:51.09  26.6875 C

>
>PT3
Mag (%)  Lag Bm1 Bm2 Bm3 Bm4
```

```
        0 100 100 100 100
        1  56  62  70  62
        2  34  37  49  41
        3  21  27  35  30
        4  21  21  26  27
        5  12  17  20  20
        6  13  13  17  16
        7  14  13  22  16
Sin Duty(%)   55  52  59  58
Cos Duty(%)   52  51  53  52
RSSI (counts)  73  75  76  63

>
>PT4
Current RTCSPI Register Status:
 Time Registers:
  Month=0007 Date=0006 WDay=0000 Hour=0088 Min=0059  Sec=0053 100thSec=0026
 Formatted Time: 17/08/06,08:59:53.08
 Ctrl=0080
 WD=0000
 Alarm Registers:
  Month=0000 Date=0000 Hour=0000 Min=0000  Sec=0000
 Alarm Time/Date Decoded:
  sec=0 min=0 hr=0 mday=0 mon=0
 FLAG=0000
 SQW=0000

>
>PA
PRE-DEPLOYMENT TESTS

DSP TESTS:
 RTC.....PASS
 RAM.....PASS
 ROM.....PASS
 ADC.....PASS
RCVR TESTS:
 COR.....PASS
 AMP.....PASS

>
>
```